PROCESSING, CHARACTERIZATION AND MODELING OF SOLUTION-PROCESSED INDIUM TIN OXIDE FILMS

A Dissertation
Presented to
The Academic Faculty

by

Ning Xia

In Partial Fulfillment
of the Requirements for the Degree
Doctor of Philosophy in the
School of Materials Science and Engineering

Georgia Institute of Technology
May 2018

PROCESSING, CHARACTERIZATION AND MODELING OF SOLUTION-PROCESSED INDIUM TIN OXIDE FILMS

Approved by:

Dr. Rosario A. Gerhardt, Advisor
School of Materials Science and Engineering
Georgia Institute of Technology

Dr. Dong Qin
School of Materials Science and Engineering
Georgia Institute of Technology

Dr. Nazanin Bassiri-Gharb
School of Materials Science and Engineering
Georgia Institute of Technology

Dr. Emmanouil M. Tentzeris
School of Electrical and Computer Engineering
Georgia Institute of Technology

Dr. Vladimir Tsukruk
School of Materials Science and Engineering
Georgia Institute of Technology

Dr. David S. Gottfried
Institute for Electronics and Nanotechnology
Georgia Institute of Technology

Date Approved: Dec 7th, 2017

ACKNOWLEDGEMENTS

I would like to express my first and foremost appreciation to my advisor Dr. Rosario A. Gerhardt for her all-around guidance during my PhD study. I would like to thank Dr. Nazanin Bassiri-Gharb, Dr. Vladimir Tsukruk, Dr. Dong Qin, Dr. Emmanouil M. Tentzeris and Dr. David S. Gottfried for serving on my committee and giving me valuable comments and suggestions.

I would like to acknowledge the funding and financial support from the National Science Foundation under DMR-1207323, Institute for Electronics and Nanotechnology Seed Grant, Arnold Magnetics and RF Genesis Inc.

I would like to thank Dr. Valeria Lauter from Oak Ridge National Laboratory (ORNL) for help with neutron reflectometry experiments and analysis.

Thanks for the help and discussions with previous and current group members: Dr. Youngho Jin, Thomas Rudzik, Morgan Watt and Zev Greenberg.

I would also like to thank my families. My parents, Xing Xia and Zhimei Jia have supported me throughout my education. My wife, Xiaoliang Song has always encouraged me during my PhD study.

Again, I would like to express my sincere thanks to everyone who has supported and helped me along my PhD journey.

TABLE OF CONTENTS

LIST OF TABLES

LIST OF FIGURES

LIST OF SYMBOLS AND ABBREVIATIONS

σ	Electrical conductivity
R_{ms}	Root mean square roughness
Z^*	Complex impedance
Z'	Real impedance
Z''	Imaginary impedance
$\|Z\|$	Impedance magnitude
R_s	Sheet resistance
V	Voltage
I	Current
ρ	Sheet resistivity
t	Film thickness
f	Frequency
ω	Angular frequency
θ	Phase angle
R	Resistance
C	Capacitance
L	Inductance
τ	Time constant
ε^*	Complex permittivity
Y^*	Complex admittance
M^*	Complex modulus
g	Geometric factor

A	Area
s	Electrodes spacing
C_g	Geometric capacitance
C_0	Open circuit capacitance
ε_0	Vacuum permittivity
ε_r	Relative permittivity
D	Diameter of circular probe tips
ε'	Real permittivity
Y'	Real admittance
Y''	Imaginary admittance
C'	Real capacitance
C''	Imaginary capacitance
a	Side length of square film
TCO	Transparent conducting oxide
ITO	Indium tin oxide
ATO	Antimony doped tin oxide
AZO	Aluminum doped zinc oxide
FTO	Fluorine doped tin oxide
PANI	Polyaniline
PPy	Polypyrrole
PMMA	Polymethylmethacrylate
PEDOT:PSS	Poly-(3,4-ethylenedioxythiophene): poly(styrenesulfonic acid)
CNT	Carbon nanotube
DMD	Dielectric/metal/dielectric

XPS	X-ray photo-electron spectroscopy
CVD	Chemical vapor deposition
AFM	Atomic force microscopy
TGA	Thermogravimetric analysis
XRD	X-ray diffraction
SEM	Scanning electron microscopy
UV-vis	Ultraviolet-visible
DC	Direct current
AC	Alternating current
NR	Neutron reflectometry
FTIR	Fourier transform infrared spectroscopy
Rpm	Revolutions per minute
SE	Spectroscopic ellipsometry
RBS	Rutherford backscattering spectroscopy
TOF	Time-of-flight
2D	Two-dimensional
3D	Three-dimensional
NSLD	Neutron scattering length density
RH	Relative humidity
FEA	Finite element analysis
WC	Tungsten carbide
LCD	Liquid crystal display
OLED	Organic light emission diodes
PVA	Polyvinyl alcohol

SUMMARY

In this research, highly transparent and conductive ITO films were fabricated by two different solution-based deposition methods: spin coating and ink-jet printing using a custom-made ITO ink. The fabrication steps and annealing process were optimized to largely reduce the sheet resistance for single-layer ITO films. Films with different number of deposited layers were systematically investigated to evaluate the optical properties, electrical properties and microstructure. Even when the film composition and microstructure are similar, multi-layer ITO films from two solution processing methods can have different optical transmittance, sheet resistance and large scale surface morphology.

To understand the reason that solution-processed ITO films has higher sheet resistivity than vacuum-processed ITO films, neutron reflectometry was used to investigate the buried microstructures of ITO films. The fitting results for the neutron reflectivity showed that solution-processed ITO films had much lower scattering length density (SLD) than would be expected for theoretically dense ITO materials. The nano-porous structure present in the solution-processed ITO films was found to be the reason. Additional characterization techniques (such as AFM, SEM) were used to corroborate these results. Furthermore, the average porosity was calculated from the SLD data. However, by correlating the porosity and the electrical properties, it was determined that the porous microstructure cannot be the only reason for the higher sheet resistivities obtained. The ITO nanoparticles may have not yet reached ideal conductivity with the current annealing procedure, which affects the overall electrical properties for ITO films.

The electrical properties of solution-processed ITO films were then studied experimentally by impedance spectroscopy (IS) using an in-plane configuration. Different experimental conditions were evaluated to better understand the IS results. Inter-particle and intra-particle conduction mechanisms in multi-layer ITO films were discussed. An equivalent circuit model was proposed and simulated with different values of open circuit capacitance. It was found that the open circuit capacitance could have a significant influence on the in-plane IS measurement results. Fitting of the experimental data proved that the open circuit capacitance dominated the measured capacitance value. DC resistance and AC impedance of the same ITO films were compared and the reasons for their differences were discussed.

The electrical properties of solution-processed ITO films were further studied by finite element analysis. Different measurement configurations were simulated using 2D and 3D models. The insulating substrate and air environment were found to have a substantial effect on the resultant capacitance but minimal influence on the impedance of the films. Simulations for a range of film thickness, size and electrical properties were conducted. The effects of sample geometry, film conductivity and electrodes geometry were discussed and compared to the experimental results, showing good agreement. Multi-layer ITO films were simulated as a single homogenous layer first and then as two separated ITO layers using the experimental data as a starting point. The simulation proved that different ITO layers were connected in a parallel way.

CHAPTER 1. INTRODUCTION

1.1 Transparent conducting films

Transparent conducting films are thin film materials with high electrical conductivity and high optical transparency in the visible light region. This kind of material is very unique and rarely seen in nature because high transparency is usually not compatible with electrical conductivity as physical properties. For example, glass is very transparent but very insulating, while silver is highly conductive but opaque to visible light. In order to combine transparency and conductivity in thin films, it is crucial to choose the right materials, use the most suitable fabrication techniques and understand how to control the film microstructure. Currently, three categories of materials can be made into transparent conducting films: metals, metal oxides and organic materials. In addition, high quality transparent conducting films can also be fabricated by making composites using any two of the above materials.

1.1.1 Transparent conducting metal films

Metals are materials with very high carrier concentration or electron density and thus they are very conductive. As an example, silver has electron density as high as 10^{22} cm^{-3}. Since these free electrons can absorb the visible light photons' energy or reflect the photons, the metal has strong absorption or reflection in the visible light region. It is possible to make metal films transparent when the thickness is decreased to less than tens of nanometers with porous structure as reported in 1985 [1]. However, if one continues decreasing the thickness, the film will be too porous and will separate into islands, thus losing its good

conductivity [2]. To overcome this problem, several new film structures have been employed such as metal grids, metal nanowires (NW) and topological nanostructures [3-5]. Compared to a continuous or porous film, metal grids can maintain relatively good transparency without sacrificing the high electrical properties. As an example, Sam et al. [3] sputtered hexagonal gold grids on glass with a sheet resistance of 15 Ω/sq and light transmission of 64% at 550 nm. To reduce the process of patterning metal grids, De et al. [5] dispersed commercially available silver NW in isopropyl alcohol and prepared silver NW film by vacuum filtration. The 160 nm thickness film had a sheet resistance of 13 Ω/sq and transmittance of 85%. Table 1.1 lists some transparent conducting metal films. One of the main issues for these metal grids is the high surface roughness they have which may cause device shorting problems. The fabrication process is still difficult due to high-cost instruments as well as difficulty in controlling thickness and microstructure. In addition, the material itself is precious metals which increases the overall cost.

Table 1.1. Properties of transparent conducting metal films.

Metal	Sheet resistance (Ω/sq)	Transmittance
Au (films) [1,2,6]	>20	60%
Au (grids) [3]	15	63%
Ag (films) [7]	51	<80%
Ag (grids) [8]	40	75-94%
Ag (NWs) [5]	13	85%

1.1.2 Transparent conducting oxide (TCO) films

The first reported transparent conducting oxide was CdO, discovered by Badeker in 1907 who found the oxidized Cd thin film became transparent and remained electrically

conducting [9]. After that initial discovery, TCO films have aroused great interest and developed rapidly. Currently, TCOs are the most important type of transparent thin films and have many applications. Most TCO materials are n-type or p-type semiconductors with a wide bandgap larger than 3.0 eV and the ability to change them by doping. Also, most TCOs are highly transparent (>80%) in the visible light region and reflective in the infrared light region [10]. The electrical resistivity for TCOs is in the range of 10^{-2}~10^{-4} Ω·cm which meets the requirement for most conducting purposes.

1.1.2.1 Indium tin oxide

Indium tin oxide (ITO), or tin doped indium oxide, is composed of three elements: indium, tin and oxygen. The most common composition for ITO is 90 wt% In_2O_3 with 10 wt% SnO_2. ITO has an excellent combination of electrical resistivity (as low as 10^{-4} Ω·cm) and optical transmission (>85%). ITO has been the most widely used TCO material in the past several decades.

As the main composition element, indium is a relatively expensive metal because of its limited availability and scattered distribution in the earth crust (0.052 ppm, less than silver of 0.055 ppm) [11]. Since the fast development of electronic technology from the 1970's, the large consumption of ITO has further increased the price of indium. Thus, researchers keep trying to find low-cost alternative materials to replace ITO, especially for those electronics that do not require high optical or electrical properties. Several transparent conducting oxide films were discovered and their opto-electrical properties were thoroughly investigated.

1.1.2.2 Other transparent conducting oxides

Besides ITO, three TCO materials have been studied: Antimony doped tin oxide (ATO), aluminium doped zinc oxide (AZO) and fluorine doped tin oxide (FTO). Recently, Yu et al. [12] deposited ATO thin films on quartz substrates by magnetron sputtering. The 300 nm ATO films reached a low sheet resistivity of 8.23×10^{-4} Ω·cm and a good transmittance over 83% in the visible region. EI Hamali et al. [13] annealed sputtered AZO thin films with thickness of 180 nm on quartz by excimer laser. The electrical resistivity was lowered from 1×10^{-3} Ω·cm to 5×10^{-4} Ω·cm and the optical transmission was improved from 85% to 90%. Banyamin et al. [14] fabricated FTO on glass substrate by sputtering with average visible transmittance of 83% and resistivity of 6.71×10^{-3} Ω·cm. The best film properties were achieved using 12 wt% SnF_2 and 88 wt% SnO_2 in the target. All the above TCO thin films have the potential to replace ITO films since their raw materials are cheaper and more easily accessible than indium. However, most oxide materials have the common problem of brittleness, thus they cannot meet the requirement for flexible devices. Table 1.2 summarizes the properties for several typical TCO films.

Table 1.2. Properties of transparent conducting oxide films.

Oxide	Electrical resistivity (Ω·cm)	Transmittance
ITO [10]	3×10^{-4}	85%
ATO [12]	8.23×10^{-4}	83%
AZO [13]	5×10^{-4}	90%
FTO [14]	6.71×10^{-3}	83%

1.1.3 Transparent conducting carbon-based films

1.1.3.1 Conducting polymers

The Nobel Prize 2000 in chemistry was awarded to Heeger, MacDiarmid and Shirakawa for the discovery of conducting polymers [15]. Their discovery broke the traditional idea that organic materials are all insulators. At first, the conductive polymers were very difficult to melt, dissolve and process in large quantity because they usually contain rigid double bonds. By emulsion polymerization [16], doping [17] and grafting [18] methods, some conductive polymers are possible to dissolve in solvent and their conductivity can be improved. Currently, polyaniline (PANI), polypyrrole (PPy), polythiophene and their derivatives [19] are the most popular conductive polymers for making transparent conducting organic films because of their good properties. Cao et al. [20] reported high quality solution-casted PANI films working as transparent electrodes. The films can achieve sheet resistance less than 100 Ω/sq with an optical transmittance above 70%. Jang and Oh [21] synthesized PPy/Polymethylmethacrylate (PMMA) core/shell nanospheres by emulsion polymerization and used them to make highly transparent conducting thin films. The 20 μm polymer films gave optical transparency higher than 81% when the sheet resistivity is about 8.62×10^{-3} Ω·cm. Currently, the most successful conducting polymer materials is Poly-(3,4-ethylenedioxythiophene): poly(styrenesulfonic acid) (PEDOT:PSS), which is a mixture of two polymers where the PEDOT is a derivative of the polythiophene. It is commercially available and can be dissolved in water which greatly broadens its applications. As reported by Vosgueritchian et al [22], spin-coated PEDOT:PSS films can achieve excellent opto-electric properties with a record sheet resistivity of 46 Ω/sq and transmittance of 82%. Most importantly, they found that the PEDOT:PSS film on flexible

substrate have no change in electrical property after over 5000 stretching cycles. Compared to the inorganic transparent conducting films, these organic films have the advantages such as low cost, easy processing, can also be flexible and mechanically robust [23]. With conductive polymers working as electrodes, it is possible to fabricate all-polymer solar cells by roll-to-roll processing without using ITO as an electrode [24].

1.1.3.2 Graphene and CNT based materials

Graphene and carbon nanotubes (CNT) are the well-known 2D and 1D carbon-based materials with very good electrical properties. Although the carbon is black in colour, they are still possible to make into transparent conducting films with controlled thickness. Wang et al. [25] demonstrated 10 nm graphene films with sheet resistivity of 1.82×10^{-3} Ω·cm and 60% transmittance in visible region. The graphene films were possible to make into dye-sensitized solar cells. Wu et al. [26] used vacuum filtration method to fabricate CNT transparent conducting films with the ability to be transferred to another substrate. The sheet resistivity can be optimized to 1.50×10^{-4} Ω·cm for a 50 nm film with 70% transmittance. Table 1.3 lists the properties of transparent conducting carbon-based films. The electrical properties of most conducting polymer films are not as good as metal and metal oxide films. High thickness films are required to achieve the low sheet resistance. For graphene and CNT film, the optical transmittance still need to be improved.

Table 1.3. Properties of transparent conducting carbon-based films.

Material	Electrical resistivity (Ω·cm)	Transmittance
PANI [20]	~1× 10^{-2}	70%
PPy/PMMA [21]	8.62 × 10^{-3}	81%
PEDOT:PSS [22]	9 × 10^{-1}	82%
Graphene [25]	1.82 × 10^{-3}	60%
CNT [26]	1.50 × 10^{-4}	70%

1.1.4 Transparent conducting composite films

To combine the advantages of metal, metal oxides and carbon-based materials, multi-layer composite materials have been developed and made into thin films. A typical structure of transparent conducting composite is shown in Figure 1.1 as a dielectric/metal/dielectric (DMD) structure [27].

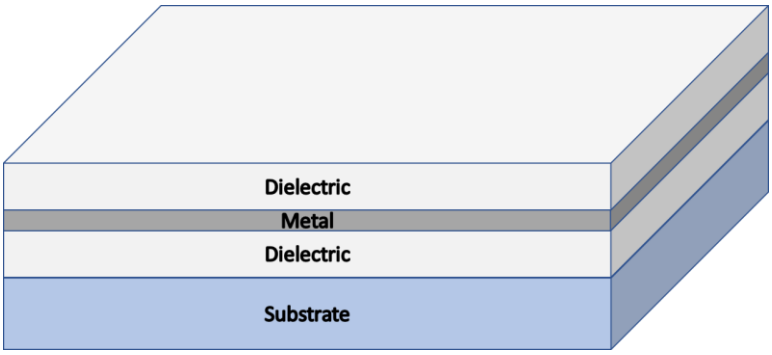

Figure 1.1. Typical DMD structure of transparent conducting composite films.

Many high quality TCO/metal/TCO thin films are reported, such as ITO/Au/ITO [28], ITO/Ag/ITO [29], FTO/Ag/FTO [30], AZO/Ag/AZO [31] etc. As an example, Yu et al. [30] reported FTO (20 nm)/Ag (7 nm)/FTO (30 nm) structure with average optical transmittance of 95.5% and average resistivity of 8.8 × 10^{-5} Ω·cm. The introduction of thin layer of metal layer can improve the electrical conductivity since the metal has high

conductivity. The sandwiched structure can effectively suppress the metal reflection in the visible light region [32], which increases the device transmission. Since the metal film is embedded between two TCO layers, it also prevents the oxidation of the metal layer. However, the processing of composite films requires a precise control of film thickness. The long-time stability of multi-layer structure still needs to be further investigated.

1.2 Properties of ITO

Despite so many materials being researched and developed for fabricating transparent conducting films, ITO is still the dominant one in the current market. Since ITO is the main topic in this research, it is essential to discuss the physical properties of ITO such as its crystal structure, electrical and optical properties.

1.2.1 Crystal structure

Since In_2O_3 is the main component of ITO ($\geq$ 90 wt%), ITO has the same crystal structure as indium oxide, which is the cubic bixbyite structure [33] shown in Figure 1.2. The unit cell has 80 atoms with a lattice parameter of 10.119 Å [34]. Bixbyite structure is a derivative of the fluorite structure (CaF_2) but missing one-quarter of the anions. As clearly shown in Figure 1.3, the indium cations are octahedrally coordinated by six oxygen anions and two structural vacancies. Thus the coordination number for indium is 6. The oxygen anions are surrounded by 4 indium cations. There are two different cation sites in the crystal structure: one is d-site (75% of the cations) with two vacancies on the face diagonal, another is b-site (25% of the cations) with vacancies on the body diagonal [35].

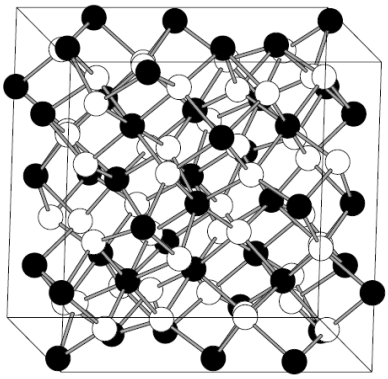

Figure 1.2. The crystal structure of Indium oxide ($In_{32}O_{48}$) shows one unit cell. The indium and oxygen atoms are represented by black and white spheres respectively [33].

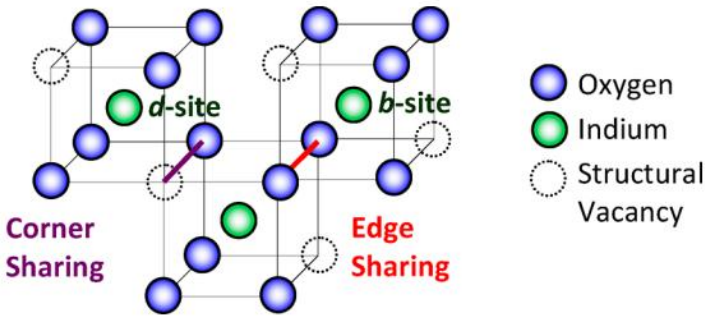

Figure 1.3. Two different indium sites in indium oxide crystal structure [35].

When the indium oxide is doped with tin oxide, the tin ions will substitute on both the indium b-sites and d-sites [36]. It was reported that the more symmetrical b-site is preferred by the tin ions [37]. With increasing tin doping, the lattice parameter gradually increases. As an example, the 6 at% Sn ITO has a lattice parameter of 10.125 Å when the number for indium oxide is 10.119 Å [34]. The simple Kröger-Vink defect reaction can be written as follows:

$$2\mathrm{SnO}_2 \xrightarrow{In_2O_3} 2Sn_{In}^{\cdot} + O_i^{''} + 3O_O \qquad (1.1)$$

1.2.2 Conduction mechanism

The pure indium oxide is a semiconductor. Under reducing conditions, high concentration of oxygen vacancies form in the indium oxide. As a doubly ionized donor, each oxygen vacancy can contribute two electrons as shown below [38]:

$$2O_o^{\times} \rightarrow O_2(g) + 2V_O^{\cdot\cdot} + 4e' \tag{1.2}$$

Thus the actual composition for indium oxide is In_2O_{3-x}. Electrons are not the only charge carriers in indium oxide. The presence of oxygen vacancies can allow oxygen ions to freely move in the crystal. So indium oxide is a mixed conductor with electronic and ionic conduction, where the latter mechanism is insignificant [39].

Since the tin ion is smaller than the indium ion, it can be substituted into indium sites without disordering the indium oxide structure. To explain the conducting mechanism of tin doping, Frank and Kostlin [36] discussed the defect structure of ITO using a $(2Sn_{In}^{\cdot} \cdot O_i^{''})^{\times}$ cluster model and confirmed by others [40, 41]. The concentration of $(2Sn_{In}^{\cdot} \cdot O_i^{''})^{\times}$ cluster in ITO depends on the tin content and oxygen partial pressure. Under reducing environment, the defect function can be written as:

$$2(2Sn_{In}^{\cdot} \cdot O_i^{''})^{\times} \rightarrow O_2(g) + 4Sn_{In}^{\cdot} + 4e' \tag{1.3}$$

Free $Sn_{In}^{\cdot}$ and electrons can work as free carriers in ITO material. Thus, ITO is a heavily doped n-type semiconductor in which electrons are the majority carriers. The degeneracy of ITO is caused by [Sn^{4+}] ion substitution in Equation 1.3 as well as the oxygen vacancies in Equation 1.2.

The electrical conductivity of most materials depends on two factors, the concentration of free carriers (N) and the mobility of free carriers (μ) which can be written as:

$$\sigma = N\mu e \tag{1.4}$$

Where σ is the electrical conductivity and e is the electron charge. To increase the electrical conductivity, high carrier concentration and mobility are required.

Theoretically, the conductivity of semiconductors can be improved by increasing the concentration of free carriers (N) with doping. For ITO material, this only works below a certain concentration of tin doping. It has been widely reported that the electrical conductivity of ITO reaches a maximum at about 6-10 at% tin doping [36, 42], and decreases after this limit. Figure 1.4 shows an example. The ITO films reach lowest sheet resistivity when the carrier concentration is the highest with 7 wt% tin doping [43]. Any higher tin doping increases the electrical resistivity.

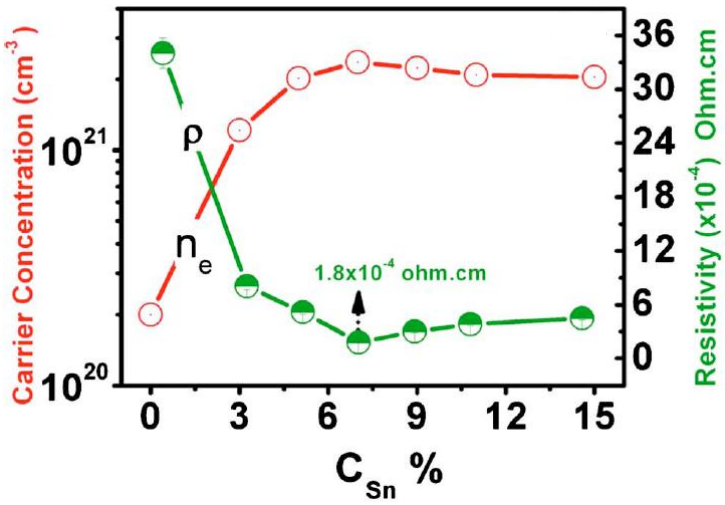

Figure 1.4. Electrical resistivity and carrier concentration of ITO with different tin concentration (wt%) [43].

One reason is that the increasing impurity doping atoms affect the mobility of free carriers since [44]:

$$\frac{1}{\mu_{total}} = \frac{1}{\mu_{impurity}} + \frac{1}{\mu_{gb}} + \frac{1}{\mu_{defect}} + \cdots \quad (1.5)$$

When the mobility of grain boundaries and defects is intrinsic, the impurity term is the most important source to affect the final mobility number. Thus the lowest possible resistivity is a balance between impurity doping and mobility [45]. Another reason is the solubility limit of tin oxide in indium oxide. Frank et al. [46] reported that the maximum solubility of tin is about 7 ± 2 at% in indium oxide. In addition, at high tin doping concentration, some portions of tin doping in ITO remain electrically inactive where each tin should contribute one free electron. This could be due to the formation of electrical neutral clusters such as [$In_4Sn_3O_{12}$] [34], $2(2Sn_{In}^{\cdot} \cdot O_i^{''})^{\times}$ [36] and [Sn_2O_4] [47].

1.2.3 Optical properties

Figure 1.5 shows simplified band structures of pure indium oxide (left) and ITO (right). The conduction band curved upwards and the valence band curved downwards. The band gap is a forbidden energy region which separates the conduction band and valence band [48]. When the lowest-energy state in conduction and highest-energy state in valence band have the same k-vector number, it is called a direct gap. When the k-vectors are different, an indirect gap is formed.

Pure indium oxide film is transparent in the visible light region [49]. The nature of its band gap is still not fully resolved. The widely-quoted direct band gap for pure indium oxide is 3.5-3.9 eV [50, 51] and the indirect band gap is 2.6 eV [42].

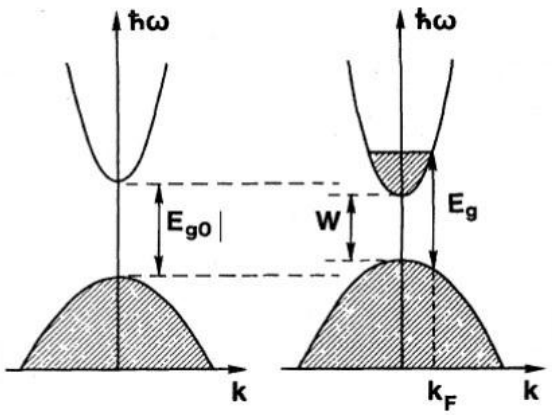

Figure 1.5. Band structures of pure indium oxide (left) and ITO (right) [48].

Recently, researchers have found that the actual direct band gap for indium oxide should be 2.9 ± 0.15 eV [53-55] by density-functional theory calculation and experimental measurements using X-ray photo-electron spectroscopy (XPS). With this band gap, indium oxide is still transparent in most of the visible light region (400-700 nm), according to the Equation 1.6:

$$\mathrm{E} = \frac{hc}{\lambda} \tag{1.6}$$

Where h is Planck constant, c is speed of light, E is the energy of photon, λ is the light wavelength. The photons with wavelength less than 427 nm can have energy larger than 2.9 eV. When the light wavelength is larger than 427 nm, the photon energy is less than the band gap of indium oxide. So the indium oxide film can be transparent. As a comparison, silicon and other non-transparent semiconductors have band gaps around 1-1.5 eV [56]. As shown in Figure 1.5, the real band gap (W) of ITO is decreased with the tin doping. But the effective indirect band gap (E_g) is actually increased because of the partially filled conduction band [57]. This band gap is large enough to prevent the inter-band transitions in the visible range and the plasma frequency of this band is also below

the visible range [58]. Thus, the ITO material is transparent in most of the visible light region.

1.3 Processing of ITO films

To obtain highly transparent and conductive ITO films, researchers discovered and developed various thin film fabrication methods. In general, the fabrication methods for ITO films can be separated into two categories: vacuum deposition and solution processing.

1.3.1 Vacuum deposition

Currently, commercial ITO films are typically deposited onto substrates using vacuum deposition, in which the processes are always operated under vacuum conditions. One can deposit thin films atom-by-atom or molecule-by-molecule, thus the thickness of products can be well-controlled. Also, the vacuum environment can remove impurities other than the source material in the chamber before deposition. This prevents the impurity from reacting with the source material and improves the quality of the products. Several vacuum deposition methods have been used to fabricate ITO films, such as evaporation [59-61], chemical vapor deposition (CVD) [62], and sputtering [63]. Some examples are shown in Figure 1.6.

In the evaporation deposition, the source material is first evaporated by energy source. Then the vapor of source material is transported to the substrate. At last, the vapor is condensed on the substrate as a solid film. Different energy sources can be used to evaporate ITO material. Plasma enhanced reactive thermal evaporation used resistively heated evaporation crucibles to deposit ITO films on polymer substrates with electrical

resistivity of 10^{-3} Ω·cm and transmittance around 80% [59]. Electron beam evaporation applied high energy electron beams to evaporate ITO and produce transparent ITO films with resistivity as low as 1.44×10^{-4} Ω·cm after post annealing [60]. Pulsed-laser deposition focused high power laser on ITO target and vaporized ITO onto substrate. The 200 nm ITO films on polyethylene terephthalate substrate were visible transparent (87%) and conductive (resistivity of 7×10^{-4} Ω·cm) [61].

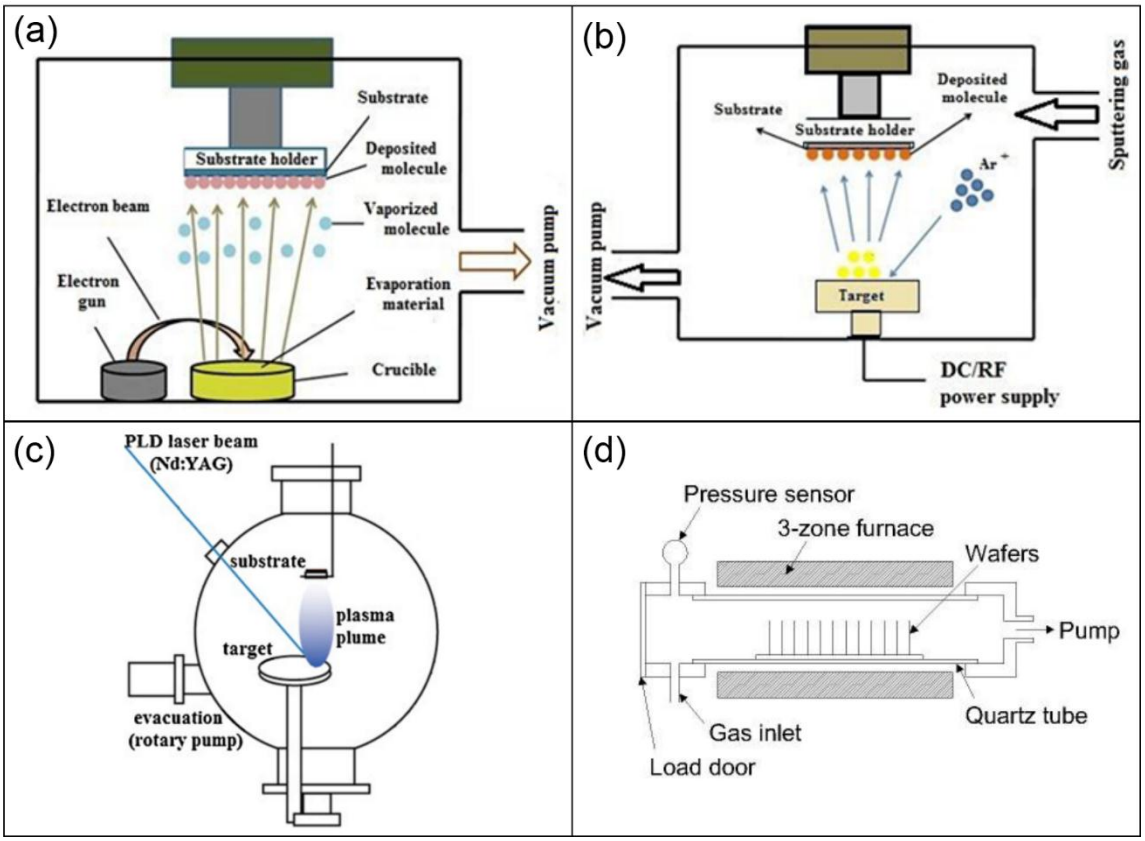

Figure 1.6. Schematics of different vacuum deposition methods: (a) Electron beam evaporation [64]; (b) Sputtering [64]; (c) Pulsed laser deposition [65]; (d) CVD [66].

Different from evaporation methods that directly evaporate ITO as source material, CVD uses chemical vapor of indium and tin precursors as source. The indium and tin precursors are reacted and/or decompose on the substrate to form ITO films with designed thickness.

Usually, a high chamber temperature is required for CVD process. Maruyama et al. [62] fabricated ITO films with resistivity of 4.9×10^{-4} Ω·cm and optical transmittance of 90% by CVD using indium acetylacetonate and tin acetylacetonate precursors. Under a reaction temperature of 350-500°C, the ITO films can achieve above quality without post annealing process.

In sputtering, high-energy ions are used to bombard the solid target. Then, particles are ejected from the target surface and deposited on the substrate to form thin films. Because of its high repeatability, wide applicability and mass producibility, sputtering is the main method for manufacturing of commercial quantities of ITO films [10]. As an example, You et al. [67] sputtered ITO films on glass substrates by DC magnetron sputtering. Using glass as substrates, ITO films had a high 89% optical transmittance and low sheet resistivity of 4×10^{-4} Ω·cm.

However, the drawbacks for vacuum deposition methods are that they require not only high-cost equipment but also strict processing conditions (high vacuum and high temperature). In addition, a large amount of ITO materials are normally wasted during the deposition. According to the literature [10, 34], the efficiency of an ITO target is only 20-30% during sputtering. Since the price of indium is very expensive ($340/kg in 2016 [68]), easily scalable processing methods with less waste should be more favorable for manufacturing ITO films.

1.3.2 Solution processing

Solution processing is one direction which has great potential to cost-effectively deposit ITO films under atmospheric conditions. Actually, one of the methods, spray coating has

been manufacturing thin films for about half a century which was first developed by Chamberlin and Skarman in 1966 [69]. Other typical solution processing methods include spin coating [70], dip-coating [71], screen printing [72] and ink-jet printing [73]. Figure 1.7 shows several different solution processing methods [44].

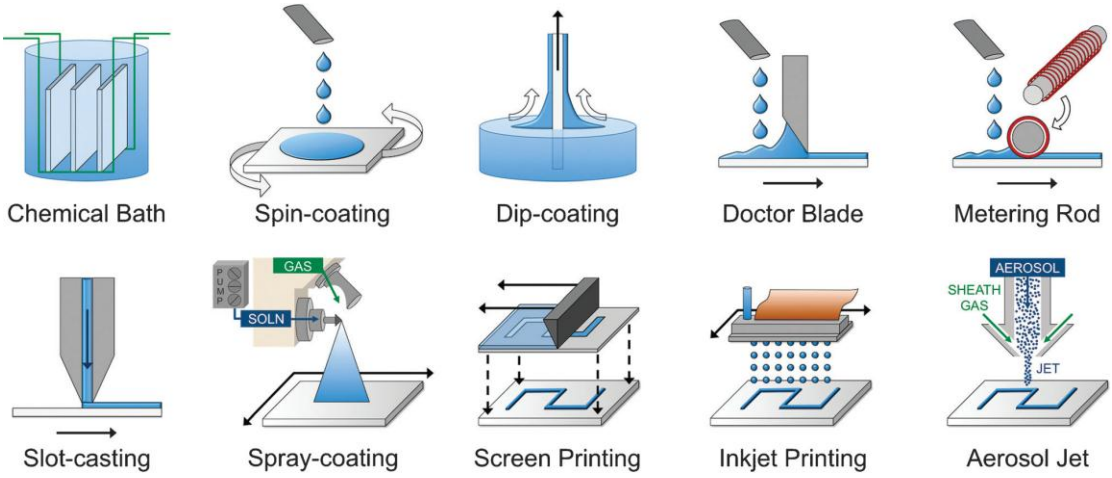

Figure 1.7. Various solution deposition methods [44].

One of the advantages of solution deposition is that it is a simple process. There are three main steps in solution processing: precursor preparation, film deposition and thermal treatment.

The precursor usually contains the material of interest or other forms of this material. For ITO film deposition, different kinds of precursors can be used such as commercial ITO nanoparticle suspensions [71], indium (and tin) salts solution [74, 75], and ITO-organic colloidal [70]. When using ITO nanoparticle suspension as precursor, relatively low annealing temperature can be achieved since ITO nanoparticles are already in crystalline form. For precursors of indium (and tin) salts, they are usually cheap and can be obtained from most commercial suppliers. As inorganic or organic salts, they can be dissolved in

water and most of organic solvents which may simplify the process. ITO-organic colloidal method represents those synthesized ITO nanoparticles surrounded with organic ligands. Although this precursor requires the organic synthesis step, the size and shape of ITO nanoparticles can be well-controlled by reaction time and organic ligands [76, 77]. Thus, all these ITO precursors can be chosen for solution deposition of ITO films.

The second step is film deposition. Almost all the methods in Figure 1.7 can be used for ITO film deposition. Depending on the characteristics of precursors, different solution deposition methods may give ITO films with different properties. To try a new ITO precursor, spin coating is usually the first choice since spin coater is a small, low-cost device often used in research laboratories. Spin coating also requires small amounts of solution to obtain a uniform thin film. As an example, Lee et al. [78] fabricated highly transparent (93%) and conductive (5.2×10^{-3} Ω·cm) ITO films with 140 nm thickness on glass substrates by spin coating. Dip-coating is another method often used to fabricate ITO films. This method needs relatively large amount of precursor solution because the substrate has to be withdrawn from the solution to form the film. For example, Ito et al. [79] reported dip-coated ITO films with high transmittance of 80% and low resistivity of 4.23×10^{-3} Ω·cm. For relatively larger size of substrates, dip-coating is better than spin-coating because the latter has thickness difference between the center and edge.

The final steps for solution deposition is the heat treatment (or annealing). This step has several important functions for thin film fabrication. First, it removes the remaining solvent in the film. Second, it helps transfer the precursor into the final product film by burning the organic ligands or decomposing salts into oxides. Third, the form or composition of the film can be changed to achieve better properties. This process usually requires a high

temperature over 500°C in the furnace. Several new heat treatment methods were developed to anneal ITO films with better properties and lower temperature, such as rapid thermal process [80], laser sintering [81] and arc plasma sintering [82]. The final film properties are similar or lower than the conventional high temperature methods. Thus it is still a challenge to anneal ITO films under low temperature for solution-processed films.

It has been proven that these solution processing methods can be used to fabricate ITO films with a good combination of electrical and optical properties. With the increasing market of display and photovoltaic devices, solution processing will be an alternative to the vacuum deposition methods for making ITO films.

1.4 Applications of ITO films

As discussed previously, ITO is the dominant material in the TCO market and thus widely used in many applications such as display technologies, solar cells, touch screens and functional glasses [83-86]. Figure 1.8 shows the sheet resistance requirements of TCO material for these devices. ITO films can achieve these properties by varying the film thickness.

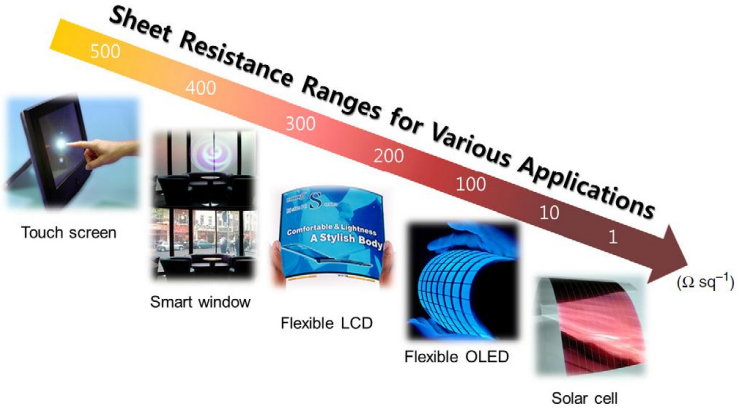

Figure 1.8. Sheet resistance requirements for TCO material for various applications [87].

Touch screen is one screen technique, which can detect the location of a touch on a normal display area. Most cell phones, tablets and computers are using this kind of screen. In a basic capacitive touch screen, two electrodes are separated by flexible insulator and form a capacitor. When touching the screen with pressure, the gap between electrode changes and thus alter the capacitance of the device. Then the touch position can be determined by measuring the capacitance [88]. Most metal electrodes can form a capacitor but their transparency is not good enough to show displays. With an optical transmittance of more than 90%, ITO is one of the best materials to work as this electrode. The actual sheet resistance requirement for this device is between 100-1500 Ω/sq [89]. Most solution-processed ITO films can reach this resistance.

Other applications of ITO films are as functional glasses, such as heating defrost glass [90], electrochromic windows [91] and smart glass [92]. In ITO-made defrost glass, ITO layer was sandwiched inside two glasses to be a transparent heaters. Comparing the normal metal-made defrost glass, ITO-made defrost glass has much better transparency. This kind of application has already been used in aircraft glass windows and military vehicles [93].

Both electrochromic windows and smart glass have the function that the light transmission or color of the glass can be altered with the application of a voltage. These glasses are usually made by putting the color changing material between two ITO-coated glasses. As an example, the electrochromic glass which uses ethyl viologen as the active layer is shown in Figure 1.9. The color of the device can be changed from transparent to blue under 1.8V voltage [94]. Different from electrochromic mechanism, smart glass uses polymer dispersed liquid crystal to alter the light direction by changing the applied voltage. Without transparent conducting ITO layer, these devices cannot show the transparent state.

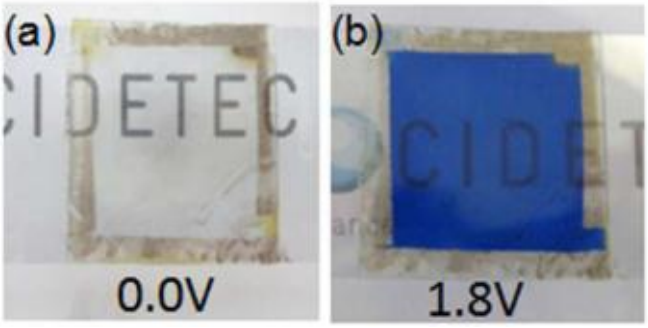

Figure 1.9. The color change of electrochromic glass under different voltages [94].

Lastly, one of the most important applications for ITO film is solar cells or photovoltaic devices. Solar energy is an inexhaustible and clean energy which will be a major source for human's future energy needs. When using metal grids as the front electrodes for solar cells, some of the light will be reflected by the metal. The solar cells using ITO film as front electrodes can prevent this and thus increase the efficiency. To manufacture large amount of solar cells and lower the total cost, solution-processed solar cells are under heavy investigation such as polymer solar cells [95], dye-sensitized solar cells [96] and perovskite solar cells [97]. High quality solution-deposited ITO films may serve as the transparent conductors for these devices and make the whole process all printable.

1.5 Research objectives and overview

The objectives for this research are to investigate the optimal conditions for obtaining high-quality ITO films with solution-based processing methods, to understand the microstructural evolution of multi-layer ITO films non-destructively and to study the impedance behavior of ITO films by experiments and simulations. The structure of this dissertation is based on achieving these objectives.

In Chapter 1, the overall background and current state of transparent conducting materials are summarized. As the most important transparent conducting material and the main research topic, the properties, processing methods and applications of ITO films are further discussed.

Chapter 2 discusses the overall experimental procedures for the preparation of ITO ink, solution processing methods and characterization techniques. Some specific experiments and characterization steps are provided in each chapter and discussed later.

Chapter 3 shows the characterization of ITO ink and the optimization of two solution processing methods for making single-layer ITO films. Multi-layer ITO films were fabricated to achieve better properties based on the best recipe for single-layer ITO films. The factors that affected the microstructure, electrical and optical properties are investigated.

Chapter 4 gives some background about neutron reflectometry and current investigation about porosity in ITO films. The electro-optical properties and microstructure of ITO films were characterized in detail. Porosity in these ITO films are quantitatively analyzed by two methods. Correlation of porosity and electrical properties are discussed.

Chapter 5 introduces impedance spectroscopy. Conduction mechanism in ITO films is proposed by providing its equivalent circuit model. The model is used to fit the experimental data for multi-layer ITO films. The influence of open circuit capacitance from in-plane measurement is analyzed. A comparison is made between DC sheet resistance and AC impedance.

Chapter 6 uses the FEA method to simulate ITO films in 2D and 3D models. The impedance and capacitance of ITO films are simulated and compared to the experimental data. The effects of sample geometry and electrode geometry are studied.

Chapter 7 presents the applications of solution-processed ITO films in this work.

Chapter 8 concludes the dissertation and suggests possible future works.

CHAPTER 2. RESEARCH METHODS

2.1 Preparation of ITO inks

To fabricate ITO films by solution-based methods, the ITO ink was made by dissolving sol-gel ITO precursors in acetylacetone. This method is modified from Chen's method [98]. Indium(III) nitrate hydrate and tin(IV) chloride pentahydrate were dissolved together in acetylacetone. The concentration of this ink is 1 mol/L for [In^{3+}] and 1/9 mol/L for [Sn^{4+}]. Thus the molar ratio of [In^{3+}] versus [Sn^{4+}] is also 9. The solution was put on a 60°C hot plate with magnetic stirring for 24 hours. The color of this ink is light brown as shown in Figure 2.1. This ink is very stable and can be kept for a few months when stored in a desiccator. Some other ITO inks were tried and discussed in Appendix A, but the resultant ITO films were not as good as films made from this ITO ink.

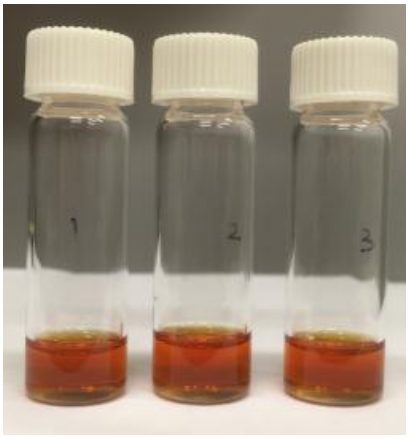

Figure 2.1. Appearance of ITO ink in the glass vials (3 vials have the same ink).

2.2 ITO Thin film deposition

In this work, two different solution-based deposition methods were used to deposit ITO films: spin coating and ink-jet printing. Borosilicate glass and quartz slides were the

primary substrates used. Slides were cut into 0.25 $inch^2$ or 1 $inch^2$ square pieces. All the substrates were cleaned with acetone and isopropanol, then treated with a UV-ozone cleaner (Novascan) for 10 minutes. Before ITO film deposition, the substrates were heated up to 120^oC to remove solvent residue and moisture.

2.2.1 Spin coating

Spin coating is a solution-processing method which deposits uniform thin films on flat surface substrates. Usually, the coating solution is drop-casted on the center of the flat substrate without rotating. Then the substrate is rotated to uniformly spread the coating solution on the substrate by centrifugal force. The film thickness is dependent on the substrate surface property, solution viscosity, concentration and spin speed. The most common way to control film thickness is by varying the spin speed. The higher spin speed can produce thinner films [99]. A CEE 100 spin coater (shown in Figure 2.2) was used to fabricate ITO films with spin coating method.

Figure 2.2. CEE 100 spin coater for spin coating.

The spin coating was done by dropping 10-25 µL of ITO ink on the substrate with a pipette. Different spin times and rates were compared to fabricate ITO films with target

thicknesses. The accelerating time is 5 s and the maximum spin time is 55 s. After each deposition, the ITO films were annealed at 120°C for 10 minutes and 450°C for 10 minutes on a hot plate to remove excess solvent and organics. Repetition of this process was used to build multi-layer ITO films on the same substrate. Post annealing steps were required to further remove organics and improve the properties of the ITO films.

2.2.2 Ink-jet printing

Ink-jet printing is another low-cost solution deposition method. This method can directly print patterned thin films by injecting ink droplets onto the substrate surface. The film thickness can be varied by changing the droplet size, droplet spacing, ink concentration and the surface affinity of the substrate. All the ink-jet printed ITO films were made by using a JetlabII ink-jet printer (shown in Figure 2.3) with ink-jet printing method.

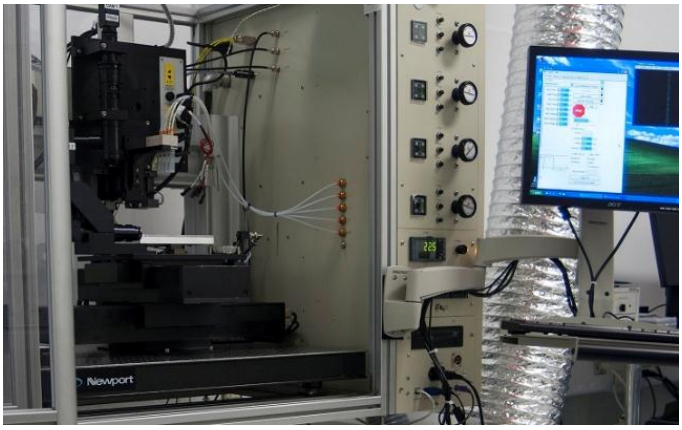

Figure 2.3. JetlabII ink-jet printer for ink-jet printing.

The printer was equipped with a 50 µm diameter jet device. 20-80 µm diameter jet devices are available to print films and patterns with different droplet sizes. After installing the jet device on the device holder, isopropanol and acetylacetone were used to rinse the jet and fluidic blocks respectively. It is important to make sure that the liquid stream is straight

from the jet and no clogs can be observed. Then filtered ITO inks were loaded into the fluidics reservoir. The pressure, dwell/echo times and voltages of the jet were set up to achieve a stable droplet with velocity of 1-3 m/s. ITO droplets can be printed on the substrate with different center spacings to change the amount of overlap, which can be used to obtain ITO films with different thickness. The diameter for a single ITO droplet on the substrate is about 200 μm. The ITO films were annealed on a hot plate at 120°C for 10 minutes and 450°C for 10 minutes. Multi-layer deposition and a post-annealing process were also used in this method.

2.3 Characterization methods

In materials science, characterization refers to general methods that use physical or chemical methods to measure, analyze and identify the nature of the structures and properties of testing materials. Characterization links the four factors of materials science: processing, structure, properties and performance. Characterization includes many specific methods, such as atomic force microscopy (AFM), thermogravimetric analysis (TGA), various microscopic techniques and electrical property measurements.

2.3.1 Atomic force microscopy

AFM is a type of scanning probe microscopy with 0.1 nm resolution, originally developed to examine insulating surfaces and invented by Bining and Quate in 1986 [100]. Basically, AFM has a sharp probe tip at the end of a cantilever to scan over the sample surface and measures the changes in forces between the probe and the sample. A laser is focused on the back of the cantilever and is reflected to a photodetector. During scanning, the position change of the laser spot on the photodetector reflects the movement of the probe tip, which

can be converted to sample surface information. AFM is a versatile characterization tool in this work which was used to investigate the size of the ITO nanoparticles, the thickness of the film and the surface morphology of the ITO films. All AFM images were taken on a Park Systems XE-100E atomic force microscope which was placed on a TS-150 vibration isolation table inside a standard acoustic box (Figure 2.4).

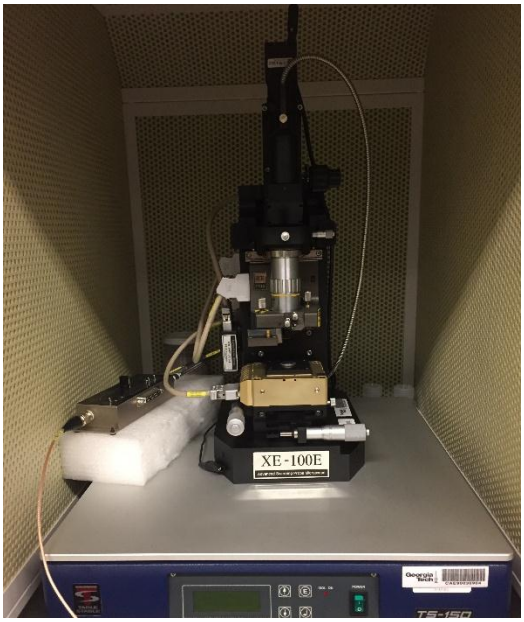

Figure 2.4. Park Systems XE-100E atomic force microscope.

An AFM usually contains several scanning modes which utilize different forces to obtain various types of surface information. To measure the thickness of thin films, a deep scratch was made on the sample surface and then contact mode AFM was used to scan across this scratch with ACTA probes (Figure 2.5(a)). Since in contact mode, the tip is always touching the sample surface, it can provide accurate topography information. The height difference of the profile is the thickness of the film. Thus, thickness can be estimated by averaging these data from several measurements in different places on the same sample.

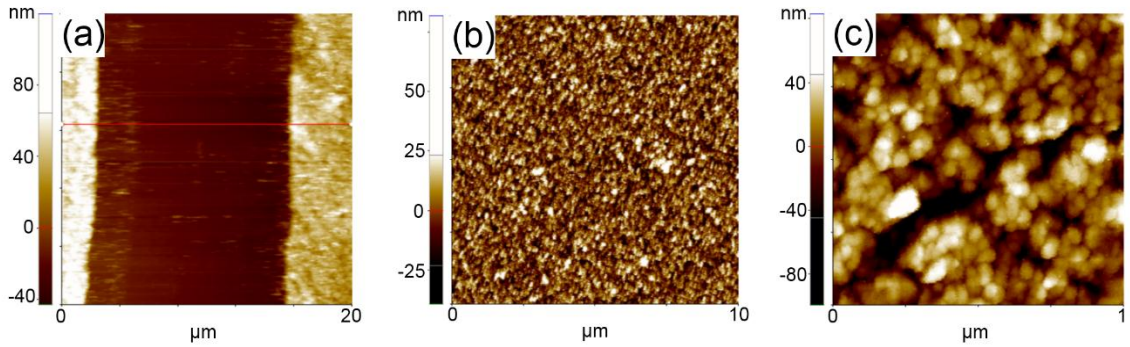

Figure 2.5. AFM images of ITO films from different scan modes. (a) Contact mode to image scratch. (b) Non-contact mode to image surface morphology. (c) Non-contact mode to image particle sizes.

For measuring particle size and surface morphology, non-contact (NC) mode is better than contact mode because non-contact scans greatly reduce tip wear and sample damage. The van der Waals force between the surface and the tip affect the tip's height and resonant frequency. With a 10 nm spike AFM tip, the topography of the sample surface (Figure 2.5(b)), as well as ITO nanoparticle size (Figure 2.5(c)), can be measured precisely. The image sizes for surface morphology measurements are usually 5×5 μm^2 and 10×10 μm^2. To better show ITO nanoparticles, the scan size is decreased to 2×2 μm^2 and 1×1 μm^2. The surface roughness is compared by using the root mean square roughness (R_{ms}) which can be read from the AFM software. R_{ms} is the root mean square average of the profile height deviation from the mean line, recorded within the evaluation length.

The ACTA AFM tips used in this work have a length of 125 μm, width of 40 μm and thickness of 4 μm. The force constant is about 40 N/m and the resonant frequency is between 250-300 kHz.

2.3.2 Thermogravimetric analysis (TGA)

Thermogravimetric analysis (TGA) is a thermal characterization method used to measure the weight loss of a sample as a function of temperature with constant heating [101]. TGA can provide physical information of samples such as the glass-transition temperature as well as chemical information like the decomposition temperature. All TGA experiments in this work were done on a SDT simultaneous Q600 TGA/DSC (thermogravimetric analysis/differential scanning calorimeter) thermogravimetric analyzer (TA Instruments) which had two horizontal dual beams design as shown in Figure 2.6.

Figure 2.6. SDT Q600 TGA/DSC for thermal analysis.

Two 90 μL alumina sample pans were put on two beams. One pan served as reference pan and another pan was used to put samples in. The purge gas flow was fixed at 100 ml/min and the temperature ramping rate was 10 °C/min. Before each experiment, the TGA was heated up to 1200°C with the designed purge gas to make sure the inside of the furnace and the pans were clean. The sample weight is controlled within 5-10 mg to make sure it covers

the bottom of the alumina pan. TGA analysis was used to find out the crystallization water content in the nitrate salts and the decomposition temperature of ITO ink solids.

2.3.3 X-ray diffraction (XRD)

XRD is a powerful non-destructive detection technique which can characterize the composition, crystallinity and crystal structure of crystalline samples and separate different crystal phases in a mixture. The reason is that every crystalline material gives different diffraction patterns when it interacts with X-rays [102]. All X-ray diffraction scans were conducted on a Panalytical XPert Systems PRO Alpha-1 diffractometer with Cu Kα source (λ = 1.5406 Å) as shown in Figure 2.7.

Figure 2.7. Panalytical XPert Systems PRO Alpha-1 diffractometer for XRD.

The instrument is equipped with an incident beam monochromator and a fast linear X'celerator detector which can generate high-resolution diffraction patterns. During the measurement, the X-ray tube stayed fixed and the sample stage and detector both rotated to collect the signals. All the incident beam and diffracted beam optics were optimized to

suit samples with different sizes. To obtain a good signal-to-noise ratio, the diffraction angle was set from 10° to 70° with a step size less than 0.02°.

2.3.4 Scanning electron microscopy (SEM)

As a common electron microscope technique, SEM can produce high-resolution images of sample surfaces with a high-energy electron beam. It has a wide measurement range from nanometer to hundreds of micrometers. In a cold field emission SEM, a highly coherent electron beam (diameter of about 0.5 nm) with accelerating voltage of 0.5-30 kV is produced by a cold cathode field emission source. This electron beam gives better spatial resolution and brighter image than the typical electron beam created by thermionic guns [103]. A Hitachi SU8230 cold field emission SEM (shown in Figure 2.8) with secondary electron (SE) mode was used to study sample surfaces and cross-sectional microstructure.

Figure 2.8. Hitachi SU8230 cold field emission SEM.

The range of SEM accelerating voltage for samples was 1-5 kV. The beam current was controlled between 10-20 μA. The working distance was set between 2-5 mm. Copper tape was used to mount samples on the stage and connect the surface to stage to minimize

charging effects. Energy dispersive X-ray analysis (EDS) was also done on this machine to determine chemical elements in the samples using the Oxford EDS detector.

2.3.5 Ultraviolet-visible spectroscopy (UV-vis spectroscopy)

UV-vis spectroscopy can measure the absorption or transmission spectroscopy in the ultraviolet-visible light region. A beam source with multiple wavelengths is focused on the sample and the detector measures the intensity of the beam after passing through it. By comparing the original intensity and transmitted intensity, the transmission or absorption can be calculated [104]. Optical transmittance of ITO films was collected by UV-vis spectroscopy with an Agilent Cary 60 UV-vis spectrophotometer (Figure 2.9).

Figure 2.9. Cary 60 UV-vis spectrophotometer.

Well-cleaned substrates were used as the baseline, which means the transmittance of the pure substrate is set to 100%. The wavelength range was 400-800 nm because high transparency in the visible light range is essential for ITO films. The transmittance at 550 nm wavelength also needs to be considered, because this is the most sensitive wavelength for the human eye.

2.3.6 Electrical characterization

The electrical properties of ITO films were characterized using two approaches: 2-probe alternating current (AC) impedance spectroscopy (IS) and 4-probe direct current (DC) resistance measurements.

For 2-probe AC IS, two sets of instruments were used. A Solartron 1260 impedance analyzer and a Solarton 1296 dielectric interface were combined together with a four-point probe setup (Figure 2.10(a)) for semiconducting and insulating samples. A Gamry 5000E potentionstat was connected with a four-point probe station for conducting and semiconducting samples (Figure 2.10(b)). The AC frequency range used was 0.1 Hz to 1 MHz with 0.1-0.5 V AC voltage. Actually, this in-plane measurement only requires two probes to conduct impedance analysis. The tungsten carbide tip spacing is 62.5 mils (1.5874 mm) and the tip radius is 1.6 mils (40.64 μm) for this four-point probe. In impedance spectroscopy, impedance (Z^*) is a complex quantity which has a real part (Z') and an imaginary part (Z''). In this method, impedance magnitude ($|Z|$) was calculated to examine the electrical properties of ITO films.

$$Z^* = Z' + jZ'' \tag{2.1}$$

$$|Z| = \sqrt{(Z'^2 + Z''^2)} \tag{2.2}$$

The second electrical characterization for ITO films was 4-probe DC resistance measurements in delta mode using a Signatone four-point probe station connected with a Keithley 2182A nanovoltmeter and a Keithley 6221 current source (Figure 2.10(c)).

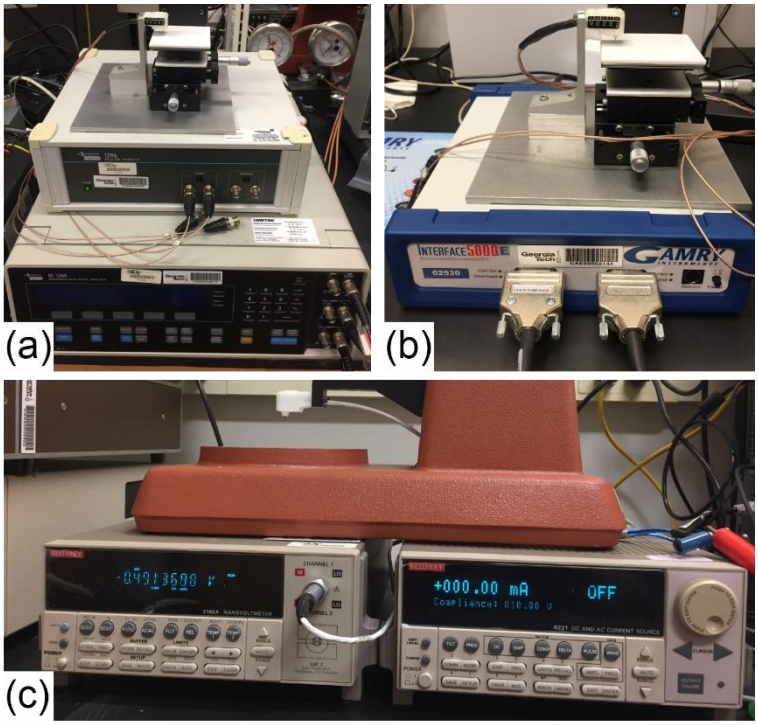

Figure 2.10. (a) Solartron instruments combination with probe station for high AC impedance samples. (b) Gamry instrument with probe station for low AC impedance samples. (c) Keithley instruments combination with probe station for DC resistance measurements.

The four-point probes in this setup have the same specifications as the ones in the 2-probe AC impedance spectroscopy measurements. During this delta mode measurement, the program alternates the current (I) source polarity and averages the measured voltage (V) automatically. This not only removes the Joule heating effect but also increases the accuracy of the measurements. Assuming that tip spacing is much bigger than film thickness, the sheet resistance (R_s) of ITO films can be calculated by Equation 2.3. $R_{reading}$ is the resistance reading from the measurement program (V/I). F is a geometric correction factor which accounts for the finite thickness of the sample, the alignment of the probes in the proximity of a sample edge and the lateral width of the sample [105]. The

correction factor for the samples in this work were calculated by finite element analysis discussed in Chapter 6.

$$R_s = F \times \frac{\pi}{ln2} \times \frac{V}{I} = F \times \frac{\pi}{ln2} \times R_{reading} \quad (2.3)$$

The sheet resistivity (ρ) can also be calculated by this sheet resistance with film thickness (t). The detailed derivation of these equations can be found in reference [105].

$$\rho = R_s \times t \quad (2.4)$$

2.3.7 Neutron reflectometry (NR)

NR is a type of neutron diffraction technique for characterizing thickness, density and structure of thin films non-destructively. In NR, a highly collimated neutron beam is directed on the sample surface, and the information of the reflected neutron beam will be measured by a detector. The reflection phenomenon of neutrons was first reported by Fermi and co-workers in 1944. However, the application of this technique as a probe started around 1980's [106]. In this work, all the NR experiments were conducted on the magnetism reflectometer (Figure 2.11) at the Spallation Neutron Source in Oak Ridge National Laboratory (ORNL) [107]. The experimental details are discussed in Chapter 4.

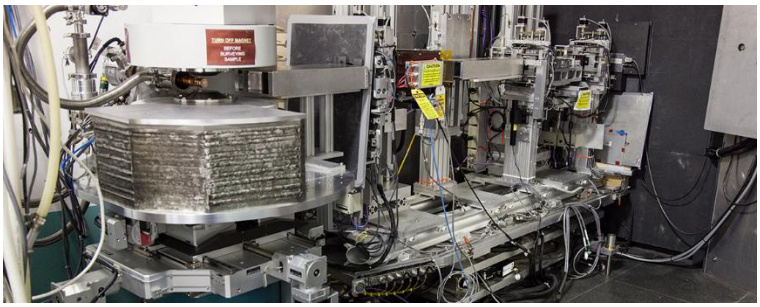

Figure 2.11. The magnetism reflectometer at ORNL [108].

2.3.8 FTIR characterization

Fourier transform infrared spectroscopy (FTIR) is a technique used to obtain the absorbance or transmission of material in the infrared range. It was a widely used analytical technique to identify organic materials as well as some inorganic materials because different functional groups (or chemical bonds, structures) in materials show different peaks in FTIR spectra [109]. In this work, a Thermo Scientific FTIR spectrometer in ATR mode with ZnSe crystal (Figure 2.12) was used to obtain the FTIR spectra of different liquid samples.

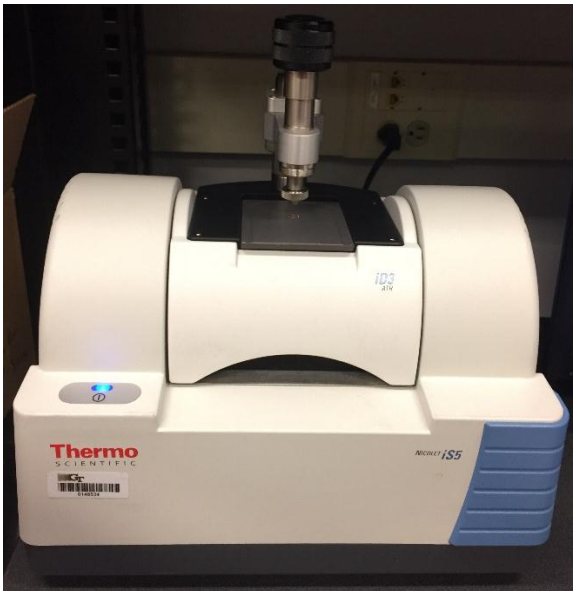

Figure 2.12. Thermo Scientific Nicolet iS5 FT-IR Spectrometer with a ZnSe crystal.

The wavenumber ranged from 4000 cm^{-1} to 600 cm^{-1}. The background was collected under atmospheric conditions. To measure liquid samples, NaCl powder was pressed into pellets and one drop liquid was placed on the pellet. The pellet with the liquid was measured when touching the ZnSe crystal.

CHAPTER 3. FABRICATION AND CHARACTERIZATION OF SPIN-COATED AND INK-JET PRINTED ITO FILMS

In this chapter, ITO films fabricated by two different solution-based processing methods, spin coating and ink-jet printing, are presented. All the ITO films were made using the same ITO inks described in Chapter 2 and same substrate (glass) under atmospheric condition (25°C, 1 ATM). The electrical resistivity, optical transmittance and surface morphology of these ITO films were characterized and compared using several different characterization tools, including 4-probe DC measurements, UV-vis spectroscopy and AFM. The goals are to determine the optimal conditions to fabricate high quality solution-processed ITO thin films and find out whether the deposition methods used affect the properties of ITO films with the custom-made ITO inks.

3.1 Characterization of ITO ink

3.1.1 FTIR analysis

For measuring IR spectra of liquid sample, one drop of liquid was placed on the surface of a NaCl pellet and then the pellet was measured by FTIR spectrometer. Figure 3.1 compares the FTIR spectra for the (a) solvent, (b) fresh ITO ink and (c) 6 months old ITO ink. Since the pure solvent (acetylacetone) is the main component in the ITO ink, the peak positions of ITO ink are similar to the ones in the solvent. The biggest difference is the peaks between wavenumber of 1500 cm^{-1} to 1600 cm^{-1}. In the pure solvent, the strongest 1600 cm^{-1} peak belongs to the stretching of carbonyl group (C=O) [110, 111]. In contrast, the ITO inks show the strongest IR peak at 1525cm^{-1} which matches the peak position of indium

acetylacetonate (In-O-C=O) [112-114]. The absorption peak at 670 cm^{-1} is another vibration peak of In-O [115]. These results mean that the solvent acetylacetonate successfully chelated the indium ion in the ITO ink and formed the more stable form of indium acetylacetonate as displayed in Figure 3.2. It has been reported that the hydrolysis rate of indium ion can be slowed down by forming this chelation compound [98]. This helps the formation of a uniform and smooth ITO film. The absorption band around 1360 cm^{-1} comes from the vibration of NO^{3-} ions because one of the precursors used is indium nitrate.

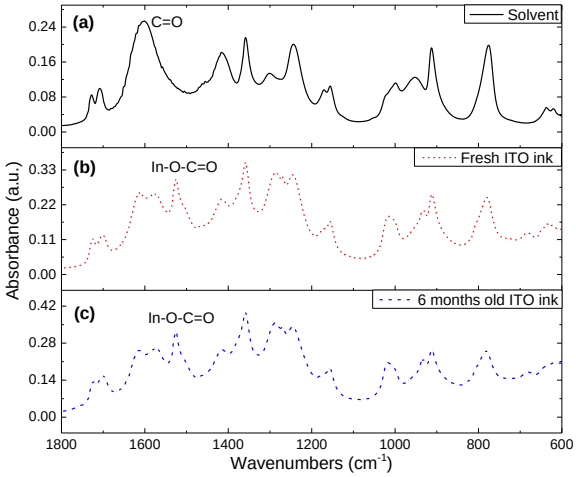

Figure 3.1. FTIR spectra of (a) solvent; (b) fresh ITO ink; (c) 6 months old ITO ink.

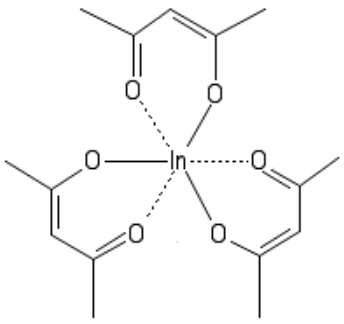

Figure 3.2. Chemical structure of indium acetylacetonate.

The FTIR also proved that the ITO ink did not degrade after long time storage. By comparing Figure 3.1(b) and (c), the IR peak positions for fresh ITO ink and 6 months old ITO ink are almost identical. So there are no other compositions formed in aged ITO ink. It was observed that old ITO ink always appears darker than the fresh prepared ITO ink. This matches the fact that 6 months ITO ink had slightly higher absorbance in IR spectra.

3.1.2 TGA analysis

It is important to understand the thermal property of ITO ink in order to choose the annealing temperature for ITO films. Figure 3.3 shows the TGA results of ITO ink solids. To obtain the ink solids, several drops of ITO ink (100 µL) were cast onto a glass substrate and dried at 120°C overnight.

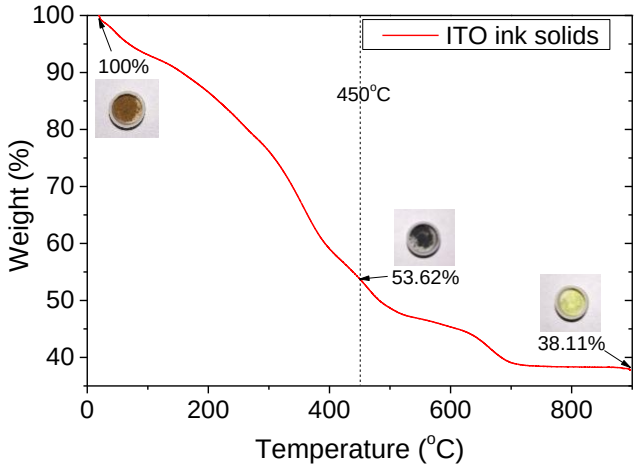

Figure 3.3. TGA results of ITO ink solids. Insets are the visual images for ITO solids at different stages.

The brown-colour ITO ink solids were scratched off from glass substrate gently and put inside TGA alumina pans. The weight curve of ITO ink solids does not become flat until the temperature reaches 750°C. 38.11% residues were left after the test and show a yellow

colour. The weight loss in the annealing process should come from the evaporation of residual solvent, decomposition of nitrate (NO^{3-}) and burning of the organic ligands [116]. However, 750°C is a very high temperature, which can easily damage or melt the normal glass substrate (melts at 500°C). In this work, 450°C was used as the highest temperature to anneal ITO films deposited on glass. This not only protects the glass substrate, but also simplifies the process by allowing the use of a hot plate to anneal the ITO films. In addition, the next section's characterization proves that 450°C annealed ITO films were already in crystalline phase and had relatively good opto-electrical properties.

One thing we notice is that when the ITO solids were annealed at 450°C, the residue powder was in black colour which means not enough annealing. However, when ITO films were annealed at 450°C, the resulting films were transparent and clear. It is possible that the particle size or sample dimension affects this annealing process. The uniformly distributed ITO nanoparticle and thin film dimension can create a much bigger surface area and thus help reduce the required annealing temperature [117].

3.2 Optimization of ITO film fabrication

3.2.1 Spin-coated ITO films

3.2.1.1 Effect of annealing temperature

One layer (1L) spin-coated ITO films were made by depositing 10 µL ITO ink (1 mol/L concentration) on 0.25 $inch^2$ well-cleaned borosilicate glass substrates using 6000 rpm spin speed. The ramping rate was 1200 rpm/s and the total spin time was 60 s. The ITO films were quickly annealed at 120°C on a hot plate for 10 minutes to remove moisture and

residual solvent. If not annealed, the films on sample surface may reflow and form big voids as shown in Figure 3.4. The formation of these big voids are mainly due to the wetting phenomena of the ITO ink on the substrate [118].

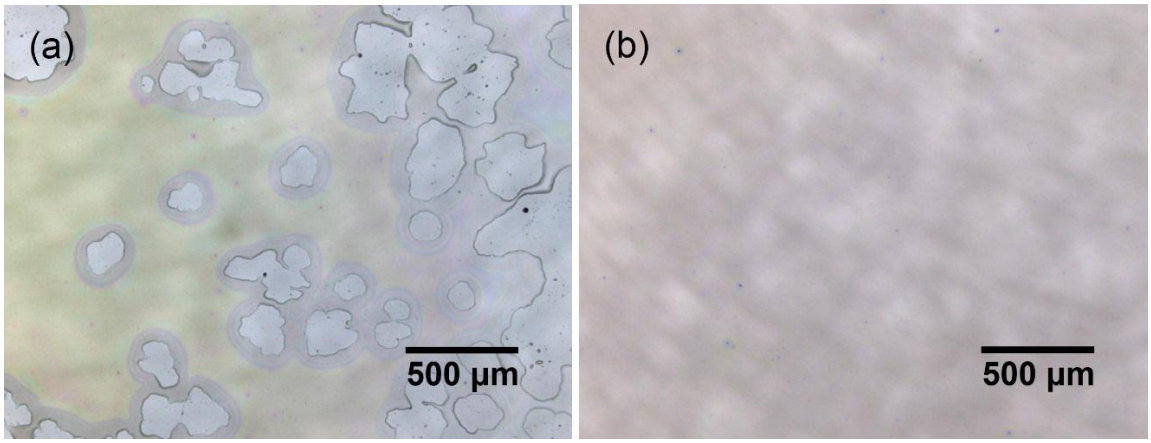

Figure 3.4. (a) As-coated 1L ITO film without any annealing; (b) 120°C annealed 1L ITO film on glass substrates.

After 120°C annealing process, several 1L ITO film samples were annealed at temperatures ranging from 200°C to 450°C on a hot plate at 50°C intervals for 10 minutes. The annealing temperature can greatly affect the electrical and optical properties as displayed in Figure 3.5. One measurement was done for each sample. Impedance spectroscopy was used here to measure electrical property because some spin-coated ITO films had very high sheet resistance which exceeded the limit of the 4-probe DC resistance measurement equipment. By controlling the annealing temperature, the impedance magnitude |Z| of 1L ITO films can be varied from 10^{12} Ω/sq to 10^{4} Ω/sq as shown in Figure 3.5(a). Indeed, not all annealing temperatures reduce the impedance magnitude of 1L ITO films. When the annealing temperature is within the range of 200°C to 300°C, the actual impedance of ITO films is higher than for the as-coated ITO films. It is possible that these temperatures caused incomplete pyrolysis or charring of the organics [119], which may impede the connection

of ITO nanoparticles. This insufficient annealing also lowered optical transparency of ITO films in Figure 3.5(b). The three curves below 90% transmittance are for annealing temperatures of 200°C, 250°C and 300°C. By increasing the annealing temperature above 350°C, the sheet resistance of ITO films gradually decreases. Finally, the 450°C annealed 1L ITO films had lowest impedance magnitude of 1.8×10^4 Ω/sq and a good optical transmittance higher than 95%. Since higher temperatures can damage the substrate, 450°C was chosen as the highest annealing temperature to anneal ITO films.

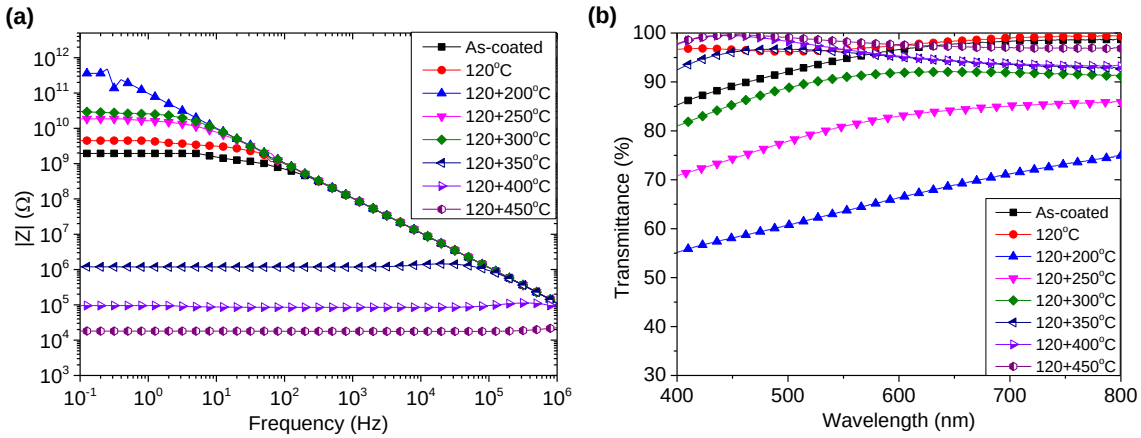

Figure 3.5. (a) Impedance magnitude and (b) optical transmittance for 1L spin-coated ITO film on glass substrates with different annealing temperature.

3.2.1.2 Effect of spin speed

1-layer ITO films were fabricated on borosilicate glass substrates with spinning rates ranging from 2000 rpm to 6000 rpm. The accelerating time is 5 s and maximum spin time of 55 s. The 6000 rpm is the maximum spin speed for the spin coater. The annealing process was 120°C for 10 minutes and 450°C for 10 minutes on a hot plate. Figure 3.6 shows the visual images of these ITO films compared with a blank substrate. All the films are transparent clear, except for the ITO films made by low spin speeds which had black color on the corners.

Figure 3.6. Visual images of 1L ITO films on glass substrates fabricated with different spin speeds. A blank substrate is on top left.

In general, the film thickness is inversely proportional to the square root of spin speed [120]. Higher spin speeds usually result into thinner films. In this work, the average middle thickness of ITO films decreased from about 200 nm to 125 nm by increasing the spin speed from 2000 rpm to 6000 rpm, which was measured by AFM. However, the 2000 rpm ITO film thickness is not as uniform as the 6000 rpm ITO film. With low spin speed, the centrifugal force is insufficient to push the ITO ink out of the substrate corner during spin coating. More ITO ink stayed on the corner than in the middle of the substrate. During the annealing process, the corners are too thick to be fully annealed and become black due to carbonization of organics, which is similar to the TGA results in Figure 3.3. By increasing the spinning rate higher than 4000 rpm, a uniform ITO film without black corners can be obtained as displayed in Figure 3.6. This phenomenon proves that different film thickness can affect the required annealing temperature for ITO films.

The electrical and optical properties of these films are shown in Figure 3.7. Five impedance measurements were done for each sample. All the 1L ITO films have an impedance magnitude in the range of 10^4-10^5 Ω/sq. By increasing the spinning rate, the electrical

property of ITO films improved with decreased thickness. Considering Equation 2.4, if all the ITO films have the same resistivity, a thicker ITO film will have lower sheet resistance. In this work, the thinnest ITO film (6000 rpm) had the lowest sheet resistance. This can be explained by different annealing effect. With exactly the same annealing conditions, the thinner ITO films are better annealed with large surface areas. Also, thinner ITO films are more transparent in the visible light range. The 6000 rpm ITO film has an optical transmittance of more than 95% as displayed in Figure 3.7(b).

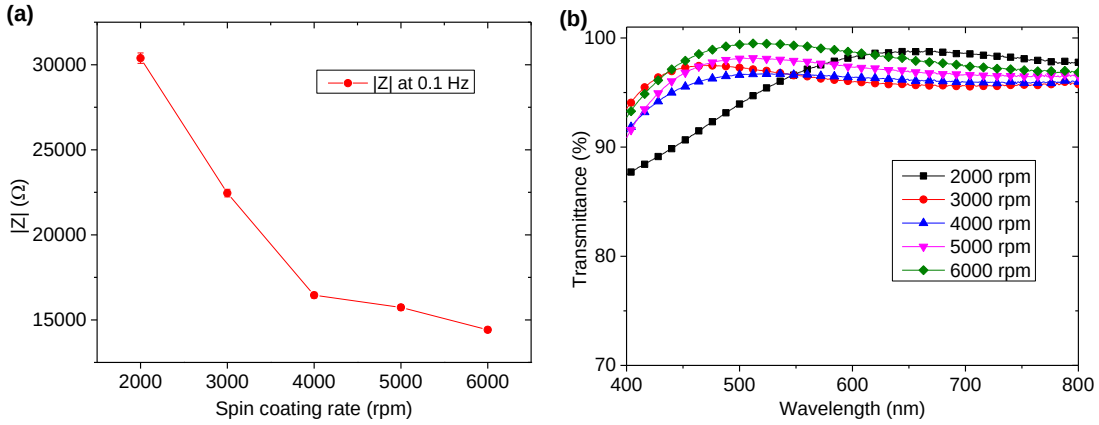

Figure 3.7. (a) Impedance magnitude at 0.1 Hz and (b) optical transmittance for 1L ITO film on glass substrates with different spin speeds after annealing.

Thus, 6000 rpm spin speed was used to make 1L ITO films. The 1L ITO films were spin coated on glass substrates with 6000 rpm, and then annealed at 120°C for 10 minutes and 450°C for 10 minutes on a hot plate. Multi-layer (2 to 5L) ITO films were made on the substrate by repeating this process. To further remove the organics and residue, all the ITO films were annealed at 300°C in a tube furnace for 3h under argon gas environment as a post annealing process.

3.2.2 Ink-jet printed ITO films

3.2.2.1 Effect of printing recipes [121]

It is important to find out the best printing recipe for fabricating high quality ITO films with the ink-jet printer. Several one layer ITO films were printed on 0.25 inch^2 well-cleaned borosilicate glass substrates with different printing recipes using 1 mol/L ITO ink. The ITO films were annealed at 120°C for 10 minutes and 450°C for another 10 minutes on a hot plate. Different printing recipes can change center-center distance between two continuous droplets on the substrate. 65 × 65 pixel recipe gives 200 µm droplets center-center spacing, whereas 130 × 130 pixel recipe gives 100 µm droplets center-center spacing. An optical microscope was used to image these ITO films as displayed in Figure 3.8. Different droplets center spacing can produce ITO films with very different surface morphologies. When the printing recipe is less than 87 × 87 pixel (droplets center spacing of 150 µm), the regular printing patterns are seen on the films surface. The regular printing patterns gradually disappear when increasing the printing recipes because the ink starts to reflow with highly coincident droplets. As shown in Figure 3.8(e), the surface of a 130 × 130 pixel ITO film showed no printing patterns.

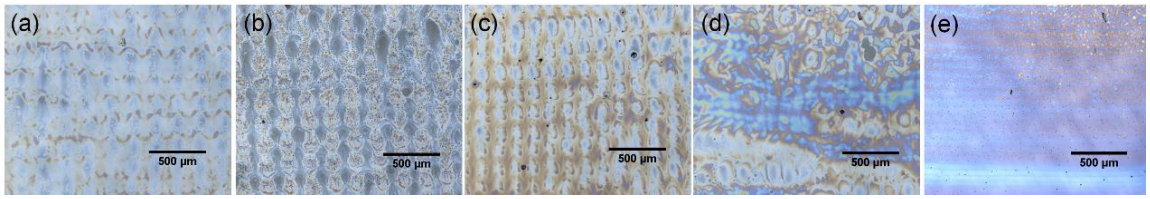

Figure 3.8. Optical micrographs of annealed ink-jet printed ITO films on glass substrates with different printing recipes: (a) 65 × 65 pixel (b) 72 × 72 pixel (c) 87 × 87 pixel (d) 100 × 100 pixel (e) 130 × 130 pixel [121].

ITO films with different printing recipes were compared by measuring the impedance magnitude and optical transmittance. Figure 3.9(a) shows the impedance magnitude vs frequency plot for different ITO films. One measurement was done for each annealing temperature. The 130 × 130 pixel ITO film had a very high impedance magnitude of 1.90 × 10^9 Ω when all other one layer ITO films had impedance magnitude in the range of 10^4-10^5 Ω. The possible reason for the high impedance of the 130 × 130 pixel ITO film is that too much ITO ink was printed on the substrate which resulted into thicker film. The quick hot plate annealing process might be insufficient to anneal the thick ITO film to form the conducting network. UV-vis spectra in Figure 3.9(b) show that all ITO films had very good transmittance. The 130 × 130 pixel ITO films were less transparent than the other films, but still maintained a high transmittance larger than 95% in the visible light region.

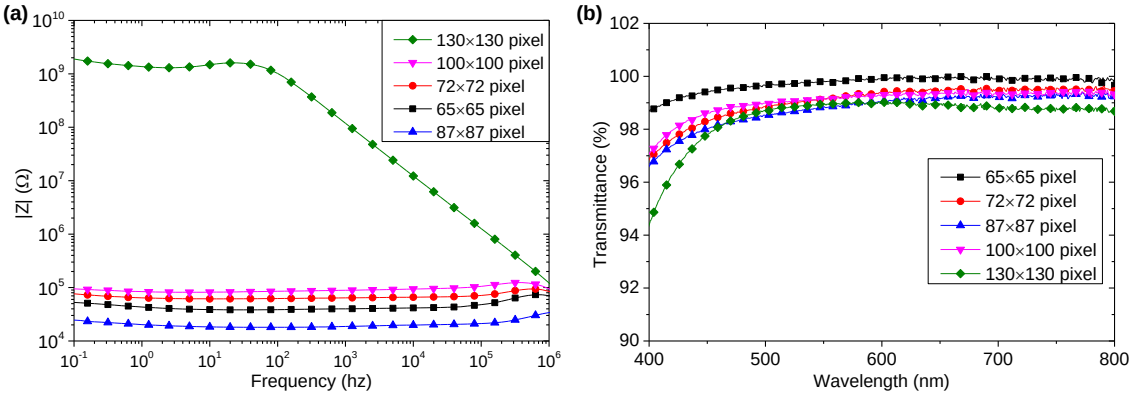

Figure 3.9. (a) Impedance magnitude and (b) optical transmittance of annealed ink-jet printed ITO films on glass substrates with different printing recipes [121].

After comparing the optical microscope images, impedance magnitude and transmittance, 87 × 87 pixel was chosen as the ideal printing recipe for multi-layer ITO films on glass substrates. The most important reason is that this recipe provided the lowest resistance in the ITO films. The distance between two adjacent droplets is about 150 µm for this recipe.

The 2 to 5L ink-jet printed ITO films were made by 87 × 87 pixel recipe and annealed after each ITO layer deposition. The post annealing process for these ITO films was the same as that used with spin-coated ITO films.

3.3 Characterization results and discussion

All the processing variables used for spin coating and ink-jet printing films in this thesis are listed in Table 3.1.

Table 3.1. Processing variables for spin coating and ink-jet printing.

	Spin coating	Ink-jet printing
Ink molarity	0.5 M, 1 M	0.5 M, 1 M
In: Sn ratio	9:1	9:1
Solvent	Acetylacetone	Acetylacetone
Number of ITO layers	1 to 5 layers	1 to 5 layers
Glass substrate type	Soda-lime, borosilicate, quartz	Soda-lime, borosilicate, quartz
Annealing temperature	120°C + (200-750)°C	120°C + 450°C
Relative humidity	10% - 65%	40 %
Post annealing	3h in Ar at 300°C	3h in Ar at 300°C
Deposition recipe	Spin speed (2000 rpm-6000 rpm)	Droplets center-center spacing (100-200 μm)

3.3.1 Effect of Ar annealing on electrical properties

As mentioned before, a post annealing process with Ar atmosphere was conducted on all the ITO films. The electrical properties of ITO films changed after annealing process. Sheet resistance is one of the most important properties to evaluate the quality of ITO films, which can be accurately measured by 4-probe DC resistance method. Figure 3.10 shows

average sheet resistance versus number of deposited layers for all the spin-coated and ink-jet printed ITO films deposited on borosilicate glass before and after post annealing process. Three measurements were done for each sample. Standard deviations are so small that they are indistinguishable from the average symbols.

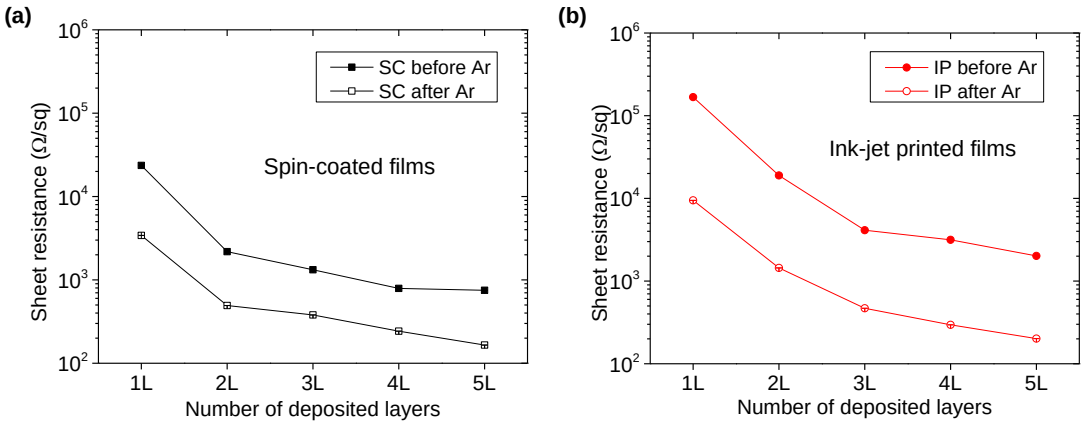

Figure 3.10. The sheet resistance versus number of deposited ITO layers on glass substrates before (solid symbols) and after (hollow symbols) Ar annealing process. (a) Black lines are for spin coated ITO films, (b) red lines are for ink-jet printed ITO films.

The post annealing process can substantially reduce the sheet resistance for all the ITO films by about one order of magnitude. As an example, the sheet resistance of 5L ink-jet printed ITO films decreased from 2.015×10^3 Ω/sq to 2.014×10^2 Ω/sq. The improvement of electrical properties can be explained by two reasons. First, this post annealing process may help further remove some organic residues. Second, the post annealing process creates a reducing atmosphere and lowers the partial pressure of oxygen. According to Equation 1.2 and 1.3, this can increase the carrier (electrons) concentration in ITO films [119]. Since no apparent optical properties and surface morphology changes were observed after post annealing process, the increasing carrier concentration should be the main reason for a lower sheet resistance.

3.3.2 Optical micrographs

All the multi-layer (1 to 5L) ITO films after post annealing were highly transparent visually as shown in the visual image of Figure 3.11. The optical micrographs for spin-coated ITO films are shown in Figure 3.12 with different magnification. The surface of borosilicate substrate is flat without any patterns. ITO films with different layers show different colours because the incident light interferes with different thickness of ITO. Besides very few 'comet' defects (which occurred when relatively large solid particles dropped on the substrate), striation patterns can be found on the surface of multi-layer spin-coated ITO films. These radially-oriented striation patterns are formed following the direction of major fluid flow during the early stages of the drying. It is mainly due to solvent-evaporation caused surface tension effect and Marangoni forces [122-124]. In addition, the humidity condition in the environment can have an effect on the formation of surface patterns [125]. Since all the solvent was gone after annealing, the striation patterns only slightly varied in thickness and had no chemical composition difference with other parts.

The optical micrographs of 1-5L ink-jet printed ITO films after annealing are shown in Figure 3.13. The regular ink-jet printing patterns can be found on all the ITO films. With a higher magnification, the pattern of dried ITO droplets can be identified. During the printing process, these droplets are overlapped on each other and cover the whole substrate. The color difference on these ITO films are also a result of the thickness differences. Overall, the multi-layer spin-coated ITO films are smoother than the multi-layer ink-jet printed ITO films when comparing the optical micrographs. The surface morphology of ITO films in this scale is different for the two solution-deposition methods.

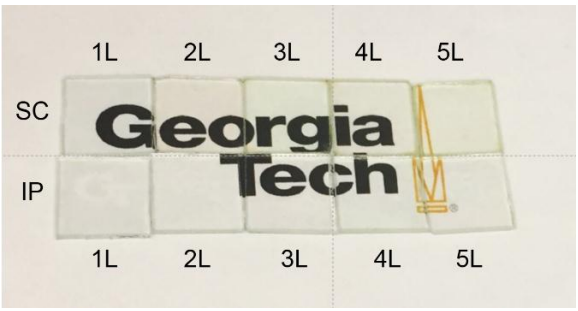

Figure 3.11. Visual images of multi-layer spin-coated (SC) ITO films (top row) and ink-jet printed (IP) ITO films (bottom row) on glass substrates.

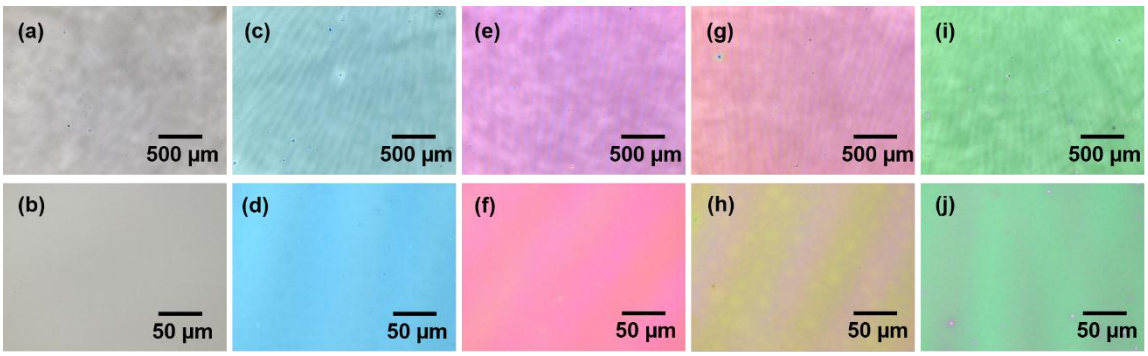

Figure 3.12. Optical micrographs with different magnifications for multi-layer spin-coated ITO films on glass substrates after annealing: (a, b) 1L ITO film; (c, d) 2L ITO film; (e, f) 3L ITO film; (g, h) 4L ITO film; (i, j) 5L ITO film.

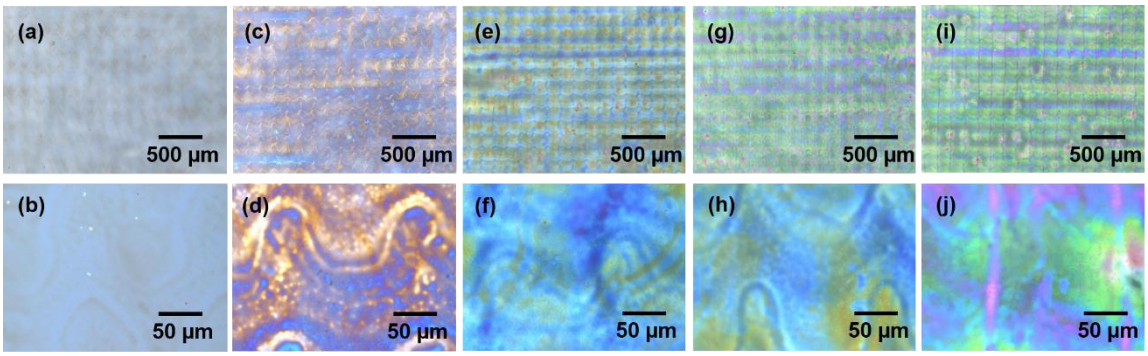

Figure 3.13. Optical micrographs with different magnifications for multi-layer ink-jet printed ITO films on glass substrates after annealing: (a, b) 1L ITO film; (c, d) 2L ITO film; (e, f) 3L ITO film; (g, h) 4L ITO film; (i, j) 5L ITO film.

3.3.3 Surface morphology and cross section for the 5L ITO films

Due to the limited magnification, optical microscopy is insufficient to investigate the microstructure of spin coated and ink-jet printed ITO films. SEM was used to characterize the top surface with better resolution. No major surface changes could be found from 1L to 5L ITO films, thus 5L samples were used to show the surface morphology. Figure 3.14 (a, c) shows SEM images of 5L spin-coated ITO films surface at different magnification. At relatively low magnification (Figure 3.14(a)), the film surface is very uniform without any defects. At relatively high magnification (Figure 3.14(c)), the film surface is still uniform with some small holes (darker spots). The surface of 5L ink-jet printed ITO films were imaged by SEM as shown in Figure 3.14(b, d). The ITO films have very smooth surface at this micrometer scale. The ink-jet printed ITO films also have small holes on the surface, as were observed on the spin-coated films.

To further investigate the surface morphology, random places on the top surface of 5L spin-coated and ink-jet printed ITO films were measured by NC-AFM as shown in Figure 3.15. Different from SEM, the AFM can clearly show the topography of the top surface because AFM has better resolution in the Z-direction.

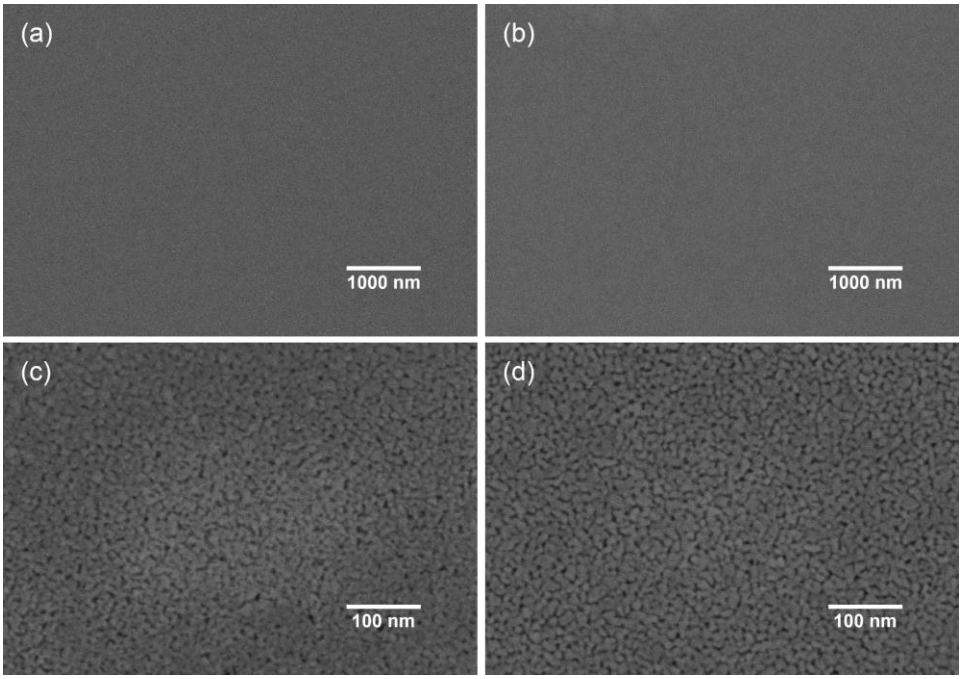

Figure 3.14. SEM images with different magnifications for 5L ITO films on glass substrates after annealing made by two methods: (a, c) spin coating; (b, d) ink-jet printing.

Figures 3.15(a, c) show that the top surface of the 5L spin-coated ITO films are slightly porous which cannot be seen in the SEM image of Figure 3.14(a). The holes on the surface may come from the fast evaporation of solvent and burning of organic residues during the annealing process. The size (<10 nm) and depth (2-3 nm) of these holes are much smaller than our previous work in which large volcano-shape voids were found on the film surface [126]. The main reason for the difference may be coming from the deposition of ITO films under different RH conditions. At relatively low humidity condition, it is generally easy to obtain a uniform and flat film surface. In contrast, the high humidity may affect the substrate wetting phenomena of ITO inks and increase the possibility of hydrolysis during deposition. To quantify the surface roughness, the root mean square roughness (R_{ms}) was measured from the AFM images. A smaller R_{ms} number means a smoother surface

morphology. The R_{ms} for the 5L spin-coated ITO film in 5 × 5 μm^2 AFM image and 2 × 2 μm^2 AFM image are 1.63 nm and 1.04 nm, respectively in Figures 3.15(a, c).

For the 5L ink-jet printed ITO films, the AFM topography images are shown in Figure 3.15 (b, d). The top surface is very uniform with slight roughness. The R_{ms} for 5L ink-jet printed ITO film are lowered to 0.83 nm and 0.80 nm for Figure 3.15(b) and Figure 3.15(d) compared to spin-coated films displayed in Figures 3.15(a, c).

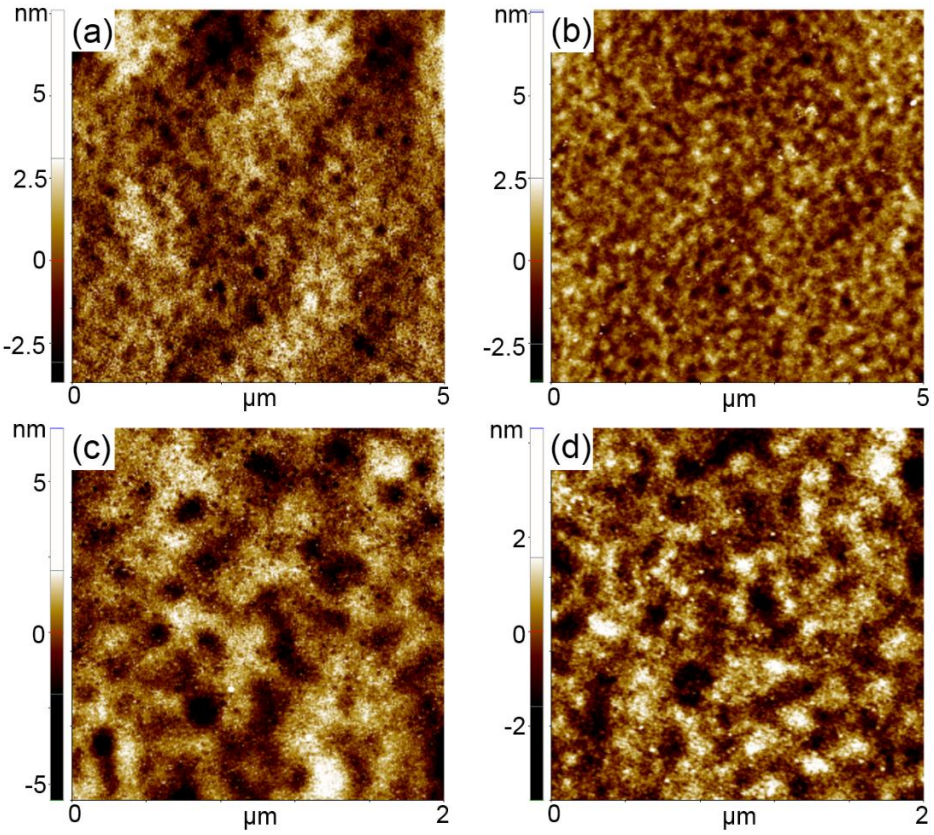

Figure 3.15. Different sizes of non-contact AFM images for 5L ITO films on glass substrates after annealing with different processing methods: (a) 5 × 5 μm^2 for spin coating; (b) 5 × 5 μm^2 for ink-jet printing; (c) 2 × 2 μm^2 for spin coating; (d) 2 × 2 μm^2 for ink-jet printing.

Although the SEM characterization shows that 5L ITO films made by spin coating and ink-jet printed have similar surface morphology at the micrometer and sub-micrometer scales, the AFM characterization reveals that they have some differences. The ink-jet printed ITO films are smoother than the spin-coated ITO films because the surface roughness numbers are smaller. Also, comparing the $5 \times 5\ \mu m^2$ AFM images (Figure 3.15(a, b), the spin-coated ITO film is not as uniform as the ink-jet printed ITO film. The different processing methods used should be the main reason for these differences.

To accurately measure the film thickness, SEM was used to image the cross section of 5L spin-coated ITO films (shown in Figure 3.16(a)) and 5L ink-jet printed ITO films (shown in Figure 3.16(b)). To prepare the SEM samples, the ITO films on glass substrates were cut into half in the middle and the cross section of films were imaged. For 5L spin-coated ITO films, five different deposited ITO layers with four interfaces can be identified on the borosilicate glass substrate in Figure 3.15(a). The interfacial regions seem to be not as compact as the ITO layer regions, especially for the interface between the bottom ITO layer and 2^{nd} bottom ITO layer. The total thickness is about 590 nm where the bottom ITO layer is thicker than all the other layers. In the cross section, ITO films are composed of small ITO nanoparticles which had a particle size around 5-15 nm. The bottom ITO layer appears to contain slightly larger ITO nanoparticles than the top layer. This is reasonable because the bottom ITO layer experienced the longest annealing time and ITO nanoparticle may have gradually increased into bigger size.

For the 5L ink-jet printed ITO films, the SEM cross sectional image (Figure 3.16(b)) shows that the ITO films are well attached on the substrate. Each single layer of the ITO film can be easily identified. The thickness of one layer is around 80 nm, which gives a total

thickness of about 390 nm. Except for the top layer, there is little difference between each layer, which means that the ink-jet printing process is highly repeatable. The average particle size is around 10 nm estimated from this image, which is similar to the size of ITO nanoparticles obtained from the spin coating method. Comparing the SEM cross sectional images, the ink-jet printed ITO films had better cross section because there are no apparent big spaces between each ITO layer.

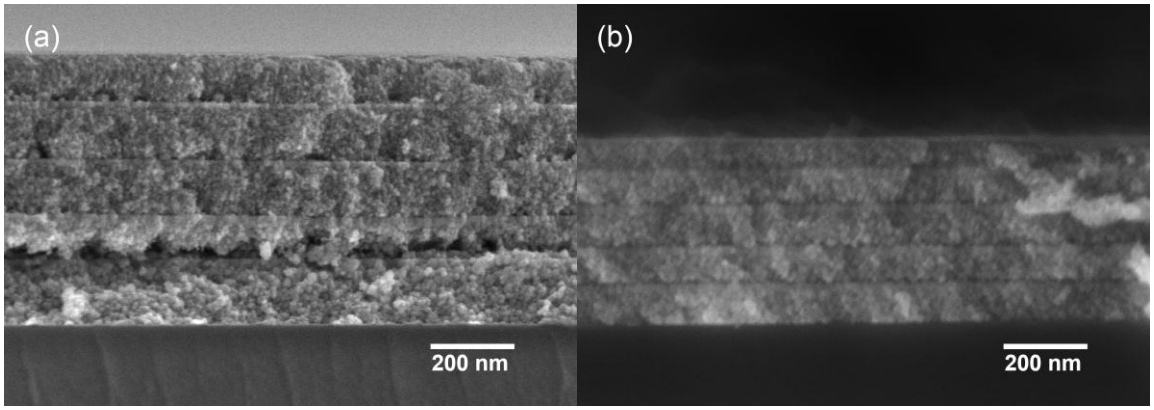

Figure 3.16. SEM cross sectional images of (a) 5L spin-coated ITO film; (b) 5L ink-jet printed ITO film on glass substrates.

3.3.4 Effect of number of deposited layers

3.3.4.1 Film thickness

The thickness of 1-5L spin-coated ITO films and 1-5L ink-jet printed ITO films after annealing were measured by AFM in contact mode. Deep scratches were made on the ITO films to reveal the glass substrate and the scratches were scanned by AFM tips. The results are shown in Table 3.1. This method can give a rough estimation about the thickness. It was demonstrated that the film thickness increased with the number of deposited ITO layers in both spin coating and ink-jet printing.

Table 3.2. Thickness for 1-5L spin-coated ITO films and 1-5L ink-jet printed ITO films on glass substrates after annealing.

Thickness	Spin coating (nm)	Ink-jet printing (nm)
1L	120 – 130	90 – 100
2L	220 – 230	160 – 165
3L	330 – 340	230 – 240
4L	450 – 465	310 – 320
5L	570 – 580	390 – 400

3.3.4.2 XRD results

XRD scans were done on all the spin-coated ITO films using the powder diffraction method. The XRD patterns are shown in Figure 3.17(a). These annealed films were deposited onto borosilicate glass substrates. All of the spin-coated ITO films had major diffraction peaks of (222), (400), (440) and (622), which were similar to the expected pattern of cubic bixbyite In_2O_3. With increasing number of deposited layers from 1 to 5L, the intensities of the diffraction peaks became stronger and the diffraction peak of (211) also showed up (another In_2O_3 peak). The amorphous glass substrate was the main reason for the broad peak observed in the low angle region due to X-ray penetration into the ITO films and detected the signal from the underlying substrate. These results prove that the 1 to 5L spin-coated ITO films are in crystalline phase without any other phases.

The 1 to 5L ink-jet printed ITO films were also characterized by Alpha-1 diffractometer using the same measurement parameters as the spin-coated films. The XRD patterns are shown in Figure 3.17(b). All the major diffraction peaks matched reference In_2O_3 peaks (JCPDS card no. 06-0416) and the peaks intensity increased with more deposited ITO layers. Thus the multi-layer ink-jet printed ITO films are also proven to be crystalline ITO.

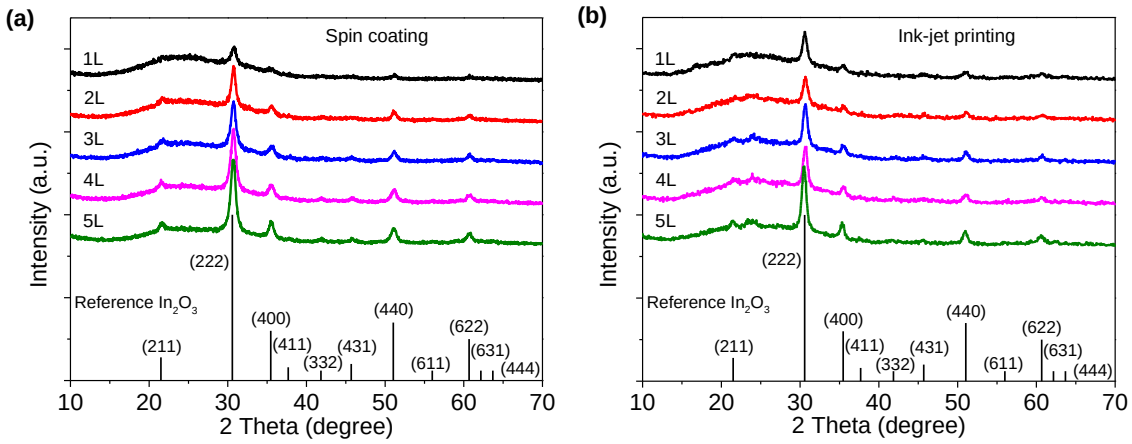

Figure 3.17. XRD patterns of multi-layer ITO films deposited on glass substrates after annealing: (a) spin-coated films; (b) ink-jet printed films. (The reference In_2O_3 peaks are shown at the bottom of the figures)

Comparing the XRD patterns of spin-coated ITO films and ink-jet printed films, no major differences can be found between the two processing methods. This is reasonable because both processing methods used the same ITO ink and the same annealing methods. The slight difference in the peak intensities may come from difference in film thickness (see Table 3.1). In both solution-processing methods, the increasing number of deposited layers improves the crystallinity of the ITO films.

3.3.4.3 Optical properties

The optical transmittance of 1-5L spin-coated ITO films and 1-5L ink-jet printed ITO films were measured by UV-vis spectroscopy and are displayed in Figure 3.18. A blank borosilicate glass with the same heat treatments as the ITO films was used as the baseline (transmittance 100%). All the spin-coated ITO films have very good optical transmittance (> 90%) in most of the visible light region (Figure 3.18(a)). When the light wavelength approaches 400 nm, the transmittance of all the ITO films tends to decrease. This is a common phenomenon for ITO films because ITO films are not fully transparent in

ultraviolet light region, where the UV photon can excite electrons from valence band to conduction band [127]. Another interesting phenomenon is that the transmittance curves of multi-layer ITO films have wave-like features. This may come from light interference between each deposited layer when the film thickness is comparable to the wavelength of incident light [80].

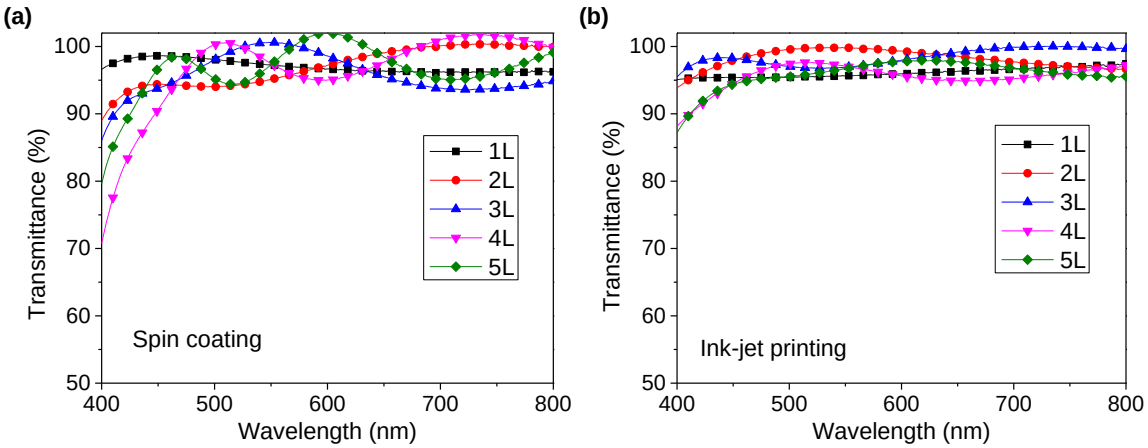

Figure 3.18. Optical transmittance of 1-5L ITO films on glass substrate after annealing made by two methods: (a) spin coating; (b) ink-jet printing. A blank borosilicate glass substrate was used as baseline (100% transmittance).

Figure 3.18(b) shows the UV-vis spectroscopy of multi-layer ink-jet printed ITO films. These ITO films also had high optical transmittance in the visible light region. In addition, these transmittance curves are smoother than the curves from spin-coated films. The wave-like feature is not as obvious. One possible reason is that the film thickness of ink-jet printed films are thinner than spin-coated films which can cause less interference with incident light. In addition, the interfaces between individual layer are smoother in ink-jet printed films as shown in the SEM images displayed in Figure 3.16(a, b).

With increasing number of deposited layers, all the multilayer ITO films can still keep high transparency with >90% transmittance in most of the visible light range. This meets optical

requirements for most electronic applications using ITO. The ink-jet printed ITO films showed smoother UV-vis spectra curves and better optical properties than the spin-coated ITO films.

3.3.4.4 Electrical properties

To better compare the electrical properties for ITO films made by the two different processing methods, sheet resistivity was plotted versus thickness in Figure 3.19 after post annealing process (sheet resistance data were obtained from Figure 3.10 and thickness data were obtained from Table 3.1). The sheet resistivity decreases with increasing film thickness and numbers of deposited ITO layers. From 1L to 3L, the sheet resistivity decreases very fast. It is possible that only one deposited layer cannot form a uniform conducting film. The second ITO deposition may fill the space between ITO nanoparticles in the first ITO layer and improve the conductivity. This needs further characterization about buried film microstructure. From 3L to 5L, the sheet resistivity decreases slowly. This is similar to the percolation phenomenon which means that depositing more than three layers will not greatly improve the electrical properties.

In summary, both spin-coated ITO films and ink-jet printed ITO films had very good electrical properties. The sheet resistivity of ITO films decreased with increasing number of deposited ITO layers. The multi-layer ink-jet printed ITO films had lower sheet resistivity than multi-layer spin-coated ITO films of the same thickness. The possible reason is that ink-jet printed ITO films may have better layer-to-layer connections as shown in the SEM cross sectional images in Figure 3.16.

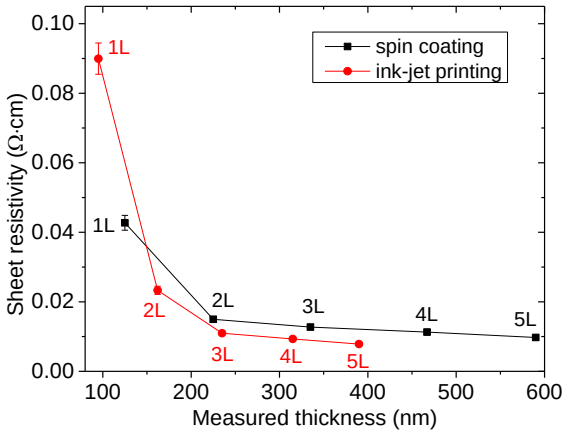

Figure 3.19. Sheet resistivity versus film thickness for multi-layer ITO films on glass substrates made by spin coating and ink-jet printing after Ar annealing.

3.4 Conclusion

Multi-layer ITO films were made by spin coating and ink-jet printing methods with the same ITO ink on borosilicate glass substrates under atmospheric conditions. The fabrication processes for each method were optimized. From AFM and SEM images, it was observed that ITO films from the two methods had similar surface topography. The ink-jet printed ITO films had a more uniform surface in the nanoscale with a smaller R_{ms}. Both ITO films had excellent optical transparency and good electrical conductivity. The optical transmittance is higher than 90% for all the ITO films in most of the visible light region, where the curves for the ink-jet printed ITO films are smoother. After post annealing process, the 5L spin-coated ITO films and 5L ink-jet printed ITO films had sheet resistance as low as 165.32 Ω/sq and 201.43 Ω/sq, respectively. The ink-jet printed ITO films had a lower sheet resistivity when taking the film thickness into account. In summary, different solution deposition methods can affect the overall properties of ITO films made from same ITO ink. Multi-layer processing strategy can significantly improve the electrical properties of ITO films with minimal effects on the optical properties and surface morphology.

CHAPTER 4. QUANTITATIVE ANALYSIS OF POROSITY IN SOLUTION-PROCESSED ITO FILMS BY NEUTRON REFLECTOMETRY

It is always a challenge to investigate the buried microstructure under film surfaces non-destructively. For example, traditionally, thin films have to be scratched or cut into half to measure thickness. In this chapter, multi-layer spin-coated ITO films deposited on quartz substrates were quantitatively analyzed by neutron reflectometry. Detailed ITO film microstructure information including film thickness, density and porosity were obtained without damaging the samples. The surface morphology, electrical and optical properties of these ITO films were also characterized with different techniques such as SEM, AFM, 4-probe DC measurement and UV-vis spectroscopy after the neutron reflectometry (NR) measurements were conducted. Many of the figures and contents in this chapter are from reference [128].

4.1 Introduction

When comparing the solution-processed ITO films with vacuum-processed ITO films, one of the property differences observed is the electrical conductivity. The sheet resistance of solution-processed ITO films is usually not as good as that for ITO films processed by vacuum-based methods. It is possible that the presence of pores and/or insufficient contact between the ITO nanoparticles affects the electrical transport mechanism in solution-processed ITO films. The formation of pores can be due to various phenomena that may occur in solution-processed ITO films. For example, wetting phenomena of the ITO ink

and substrate may create big pores on ITO films [129]. When evaporating the solvent and impurities with low boiling point in the annealing steps, small pores may form between the polycrystalline ITO nanoparticles. Additionally, if the ITO solutions or dispersions contain organic compounds, remnants of these materials may persist [119].

Different methods have been attempted to characterize the porosity of solution-processed ITO films. For example, Ederth et al. [130] reported ITO films produced by spin coating methods using an ITO nanoparticle dispersion. With fulfillment of quasistatic approximation, the Bruggeman effective medium model [131] was first used to fit optical spectroscopy measurements for ITO films before and after the annealing process. Low filling factors of 0.33 were obtained for these ITO films which meant that the porosity could be as high as 67%. This is a good method to estimate porosity. However, there are quite a few of parameters that need to be estimated, which may cause inaccuracy issues.

The porosity of ITO films has also been investigated by other characterization methods. One example is Rutherford backscattering spectrometry (RBS). Sol-gel dip-coating method was used to coat multi-layer ITO films on pyrex substrates as reported by Daoudi et al. [132]. The mass density of ITO films increased with the number of deposited layers. The 1-layer films gave 64.1% density of bulk In_2O_3. When converted to porosity, this method yielded about 35.9% porosity in these ITO films. Another useful method is spectroscopic ellipsometry (SE). Sol-gel solution was used to deposit ITO films by spin coating followed by annealing up to 550^{o}C [133]. The analysis of the ellipsometric measurements showed that single-layer ITO film had a porosity of 50%.

Non-destructive and highly penetrating neutron reflectometry is ideally suited for depth characterization of the microstructure of thin films. NR is a neutron specular reflection technique which can measure the near surface structure information of materials. The general principle is similar to RBS [132], SE [133] and X-ray reflectivity [134], using a highly collimated beam to shine the flat surface of material and then measure the information from the reflected beam. However, NR has several advantages with respect to other reflectivity techniques because NR uses neutrons as the beam source. NR is more sensitive for measuring lighter elements, isotopic elements, composition and density because it has more contrast arising from different nuclei instead of electron density only [135]. As an example, hydrogen and deuterium can be differentiated by NR.

Also, NR shows information about deeply buried interfaces non-destructively due to the high penetrability and low absorption of neutrons inside materials [136]. As reported, the largest penetration depth of NR is around 5000 Å which is much deeper than other reflectivity techniques. [137]

NR has been previously applied to probe the structure of multi-layer thin films and multilayers with buried interfaces, and used to determine the thickness of each layer together with the structure and the composition depth profile [138-140]. Additional information about the 3D morphology of the system can be obtained by using the combination of neutron specular reflection and off-specular scattering, which allows for monitoring the details of lateral inhomogeneities [141, 142]. In this chapter, NR is used to characterize highly transparent and conductive multi-layer ITO films fabricated by spin coating methods. Porosity in these ITO films are quantitatively analyzed by two methods.

4.2 Experimental details

4.2.1 Spin coating

The preparation procedure for the ITO ink was described in Chapter 2. The concentration of the ITO ink used in this chapter was 0.5 mol/L for [In^{3+}] instead of 1 mol/L. Spin coating was used to deposit the 25 μL ITO ink onto the 1 × 1 $inch^2$ amorphous quartz substrates with 4000 rpm spin speed. The ramping rate was 800 rpm/s and total spin time was 60 s. After deposition, all the ITO films were annealed at 120°C for 10 min and then at 450°C for 10 min on a hot plate. Multiple coating layers (1 to 5 layers) were deposited on the same type of quartz substrate to get ITO films with different thickness [126]. To further improve the electrical properties, all the ITO films were annealed at 300°C for 3h under argon atmosphere in a tube furnace [119].

4.2.2 Neutron reflectometry

The neutron reflectometry experiments and analysis were done by Dr. Valeria Lauter at the Magnetism Reflectometer [107] at the Spallation Neutron Source at Oak Ridge National Laboratory (Oak Ridge) using the time-of-flight method. A well-collimated neutron beam impinges on the sample surface at a glancing angle α_i and specularly reflects at an angle α_f, so that $\alpha_i = \alpha_f$. In the time-of-flight method, neutrons of different wavelengths are sorted according to the time needed for going from the source to the detector, i.e. the neutrons are sorted by neutron wavelength. The data were recorded with a position sensitive detector for a wide range of incoming and outgoing wave vectors k_i and k_f. The reflected and scattered intensities are normalized for the detector efficiency and for the intensity spectrum of the incident beam. The data are presented in two-dimensional (2D) intensity

maps as a function of p_i and p_f, where $p_i = 2\pi \sin \alpha_i/\lambda$ and $p_f = 2\pi \sin \alpha_f/\lambda$ are the components perpendicular to the sample surface of the incoming and outgoing wave vectors, respectively (see schematic in Figure 4.1).

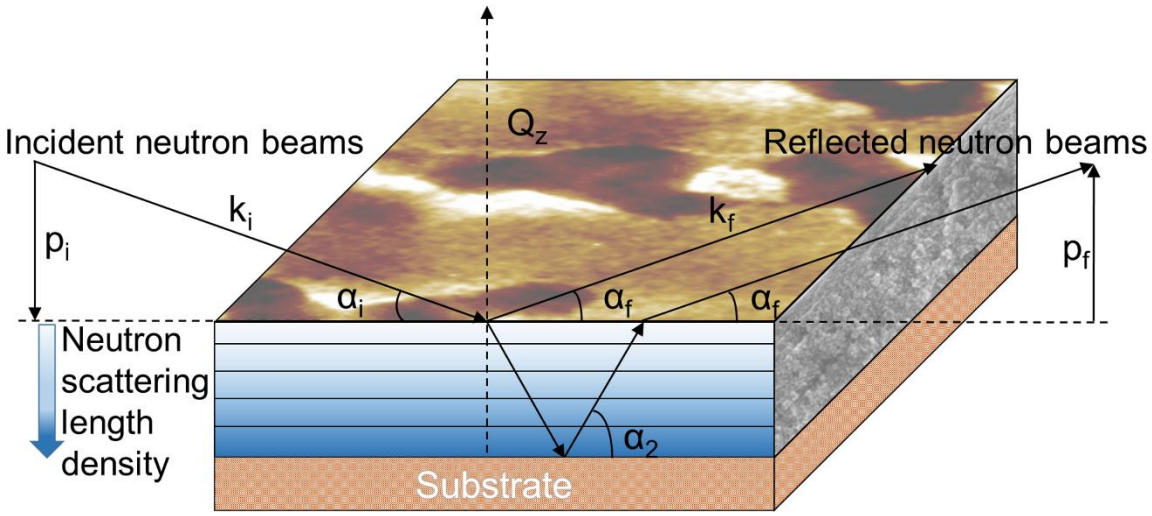

Figure 4.1. Schematic of neutron reflectometry experiment with superimposed AFM image of the top surface and SEM cross-section of the 5-layer ITO film on quartz substrate [128].

The specular reflectivities are extracted from these 2D intensity maps as a function of the incident momentum transfer normal to the surface, $Q_z = p_i + p_f = 4\pi \sin \alpha_i/\lambda$ (see Figures 4.2(a)-(d)). Neutron reflectometry experiments directly explore the depth profile of the films [142, 143]. From the experimental data, the neutron scattering length density (NSLD) is obtained. NSLD measures the Nb (with N being the atomic number density and b the scattering length averaged over a unit volume), thus being sensitive to the atomic density distribution with depth sensitivity. The depth resolution in the present reflectometry experiments is 0.5 nm, which is limited by the measurement range and the instrumental resolution.

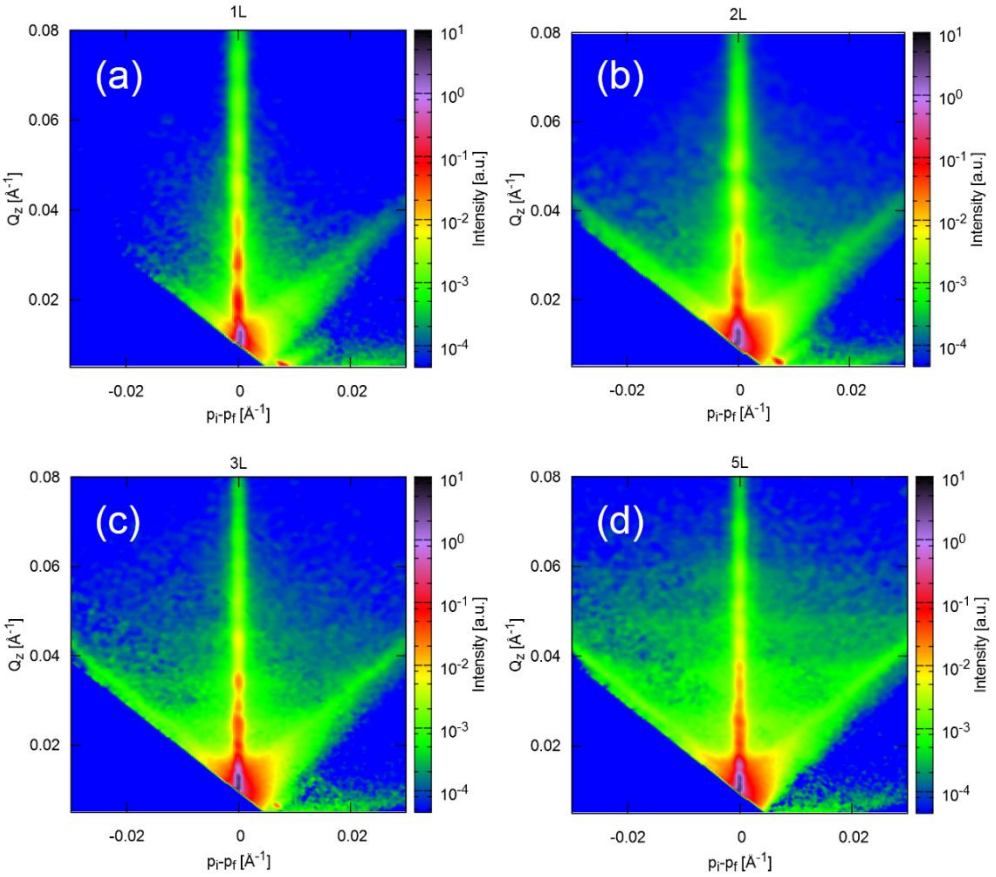

Figure 4.2. 2D intensity maps for multi-layer ITO films on quartz substrates: (a) 1-layer (1L); (b) 2-layer (2L); (c) 3-layer (3L); (d) 5-layer (5L) [128].

4.3 Characterization results and discussion

4.3.1 XRD characterization

Figure 4.3 shows XRD patterns of four multi-layer ITO films after all annealing steps. The crystal structure of these ITO films is body-centered cubic bixbyite, since the positions of the most intense four peaks (222), (400), (440) and (622) matched well with the In_2O_3 reference (JCPDS card no. 06-0416). The XRD patterns show that upon increasing the number of deposited layers, the intensity of the major diffraction peaks became stronger. This is probably related to the different thickness of the films and different degree of

crystallization in the films [144]. The broad peak observed in the low angle region (< 28°) comes from the amorphous quartz substrate, because our ITO films are very thin (75 – 340 nm). Although the intensities of some ITO films were not very strong, the XRD tests proved that our spin coating procedure followed by low temperature Ar annealing produce ITO films in crystalline phase, as was demonstrated in Chapter 3 for films deposited onto borosilicate glass. No other phases or contaminations were found from XRD analysis.

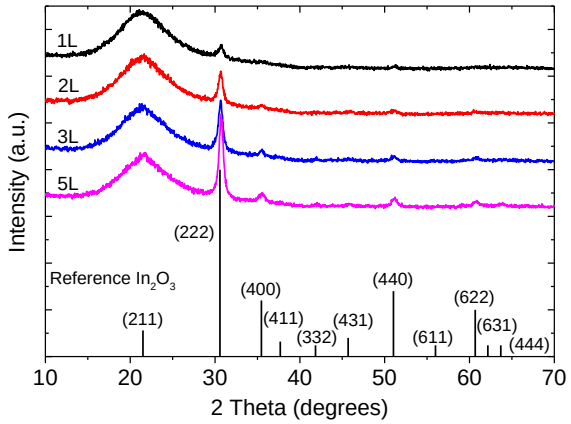

Figure 4.3. XRD patterns of multi-layer ITO films deposited on quartz substrate compared to reference In_2O_3 peaks. The intensities of major peaks became stronger with increasing number of deposited layers [128].

4.3.2 Optical micrographs

All of the ITO films were characterized by optical microscopy. On a relatively large scale (~100 μm), the annealed ITO films appeared smooth and uniform without any big defects as shown in Figure 4.4. However, it is possible to notice that there are some uniformly distributed patterns on the surface. Nevertheless, the insets in each of the images show that all of the ITO films were visually transparent and devoid of any large defects.

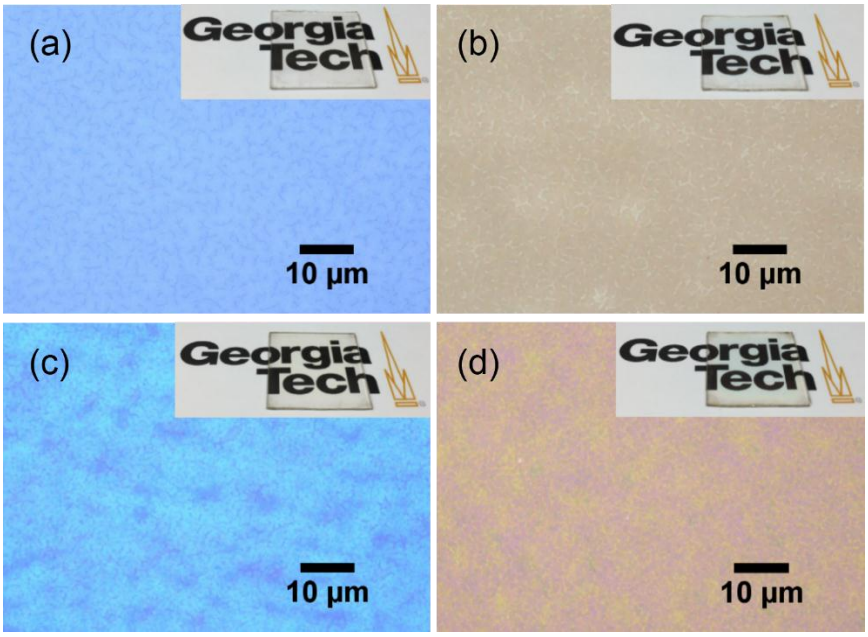

Figure 4.4. Optical micrographs of ITO films deposited on quartz with different number of deposited layers: (a) 1-layer; (b) 2-layer; (c) 3-layer; (d) 5-layer. The large scale surface morphology for all the ITO films is uniform without any large defects. Insets are the corresponding visual images for each film [128].

4.3.3 Surface morphology

To investigate the surface morphology in more detail, both SEM and AFM were used. Figure 4.5 shows the appearance of multilayer ITO thin films that contained from 1 to 5 layers taken by SEM. Each of the films show light and dark regions. It is clear that the light contrast regions slowly become interconnected as the number of layers was increased (see Figure 4.5(a-d)). Energy dispersive analysis of these regions was conducted but no obvious changes in composition could be detected between the dark and lighter regions. It was only after we imaged these same samples in NC-AFM that the source of the light and dark regions could be identified. Figure 4.6, displaying the NC-AFM images, reveals that the lighter regions contain elongated pores with very small roughness of < 10 nm. Even though SEM imaging is known to be a good method to detect depth of field, it was unable to reveal

the source of the lighter patterns because the pore depth was below its resolution at that magnification. It should be noted that the shapes of these pores are very different from our previous results of films deposited on a different substrate which showed volcano type pores [126].

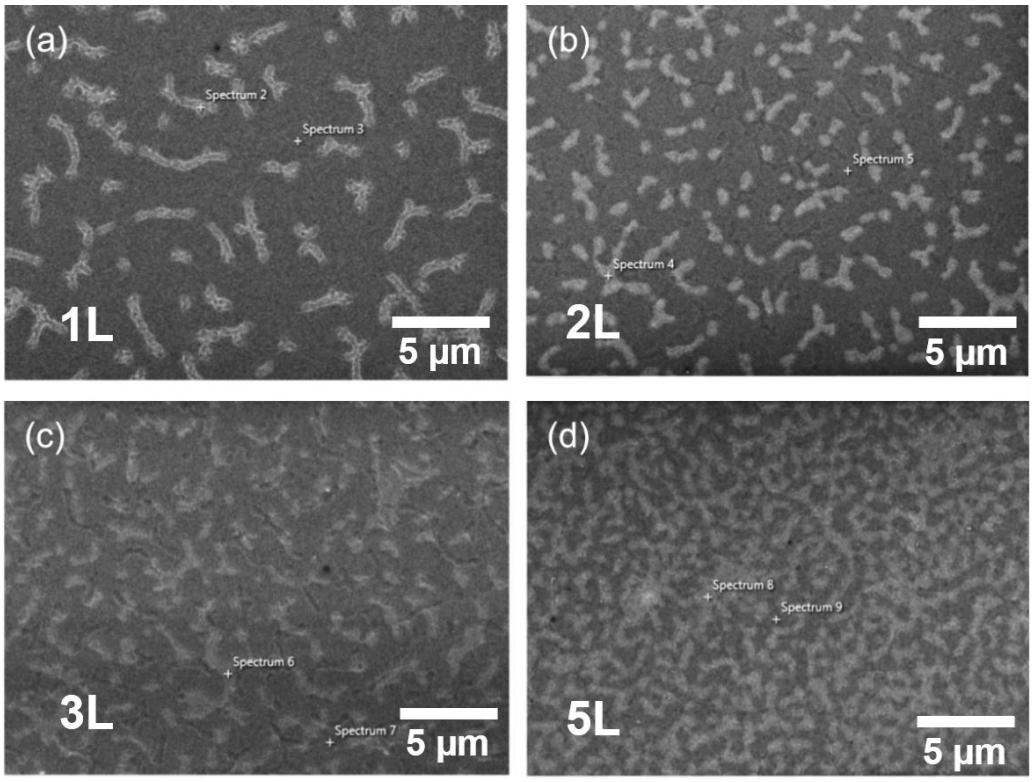

Figure 4.5. SEM images of ITO films deposited on quartz with different numbers of deposited layers: (a) 1-layer; (b) 2-layer; (c) 3-layer; (d) 5-layer. EDS analysis demonstrated that there are no big composition differences between the light and dark regions (not shown) [128].

The existence of the pores seen in Figure 4.6 (a-d) means that all of the solution-processed ITO films investigated here have a porous structure that can only be seen at high enough magnification (i.e. on the 10 × 10 μm^2 NC-AFM images). However, the surface morphology of the 5-layer ITO film (Figure 4.6 (d)) was completely different from that of the 1-layer ITO film (Figure 4.6(a)). The reason is because the pores become inter-

connected to each other as we add additional layers when multiple layers are deposited (e.g. 3L ITO film shown in Figure 4.6(c) is different from Figure 4.6(b) for 2L ITO film), now revealing why the lighter images in the SEM micrographs presented in Figure 4.5 appeared to connect. More recent experiments have indicated that these voids might be the effects of air humidity and substrate type during fabrication. Since the films investigated in this chapter were all made under the same conditions, any changes seen are a function of the film thickness and number of layers only.

Figure 4.6 (e, f) shows the 2×2 μm^2 NC-AFM images for 1-layer ITO film and 5-layer ITO film. Without the big voids, the 1-layer ITO films are relatively uniform at this scale. Since too many big voids are on the film surface, a relatively flat region cannot be found on the 5-layer ITO film as shown in the Z-scale.

The surface morphology numbers for these samples are also much larger than the ones in Chapter 3 because of the large pores. The depth of the pores can be as deep as 15 nm. The R_{ms} increased from 3.85 nm for 1L ITO film (Figure 4.6(a)) to 6.14 nm for 5L ITO films (Figure 4.6(d)) in 10×10 μm^2 AFM images. In a small size (2×2 μm^2) and relatively flat region (Figure 4.6(e)), the 1L ITO film has a smaller R_{ms} of 1.39 nm.

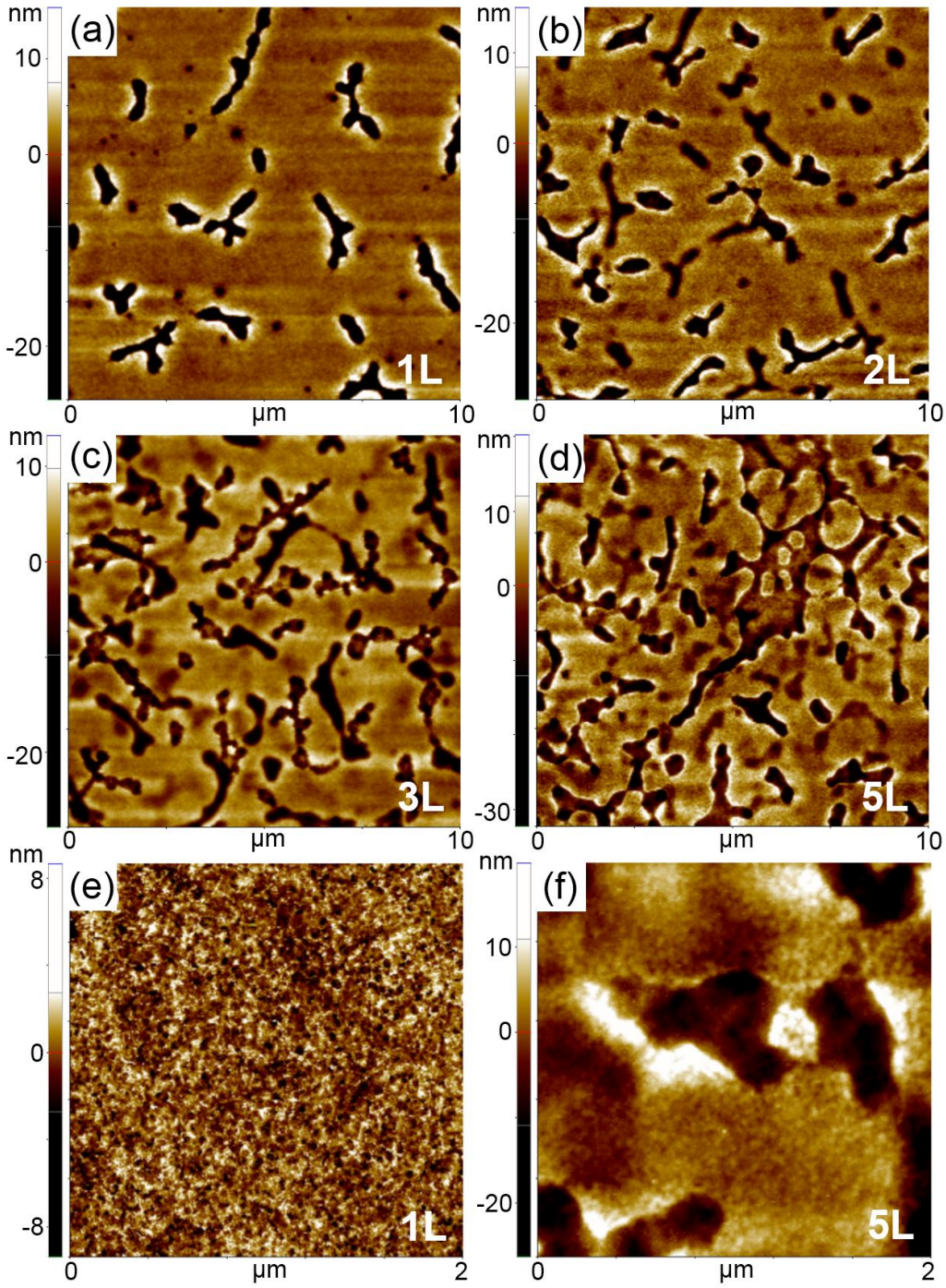

Figure 4.6. Non-contact AFM images for ITO films deposited on quartz for the series of 1-layer to 5-layer films: (a) 10 × 10 µm^2 for 1-layer; (b) 10 × 10 µm^2 for 2-layer; (c) 10 × 10 µm^2 for 3-layer; (d) 10 × 10 µm^2 for 5-layer; Higher magnification images: (e) 2 × 2 µm^2 for 1-layer; (f) 2 × 2 µm^2 for 5-layer. The images show that there are pores of different sizes present on the surface of all the ITO films [128].

4.3.4 Neutron reflectometry results

To better understand the microstructure of the ITO films and to explore the depth profile and the hidden interfaces of the multi-layer ITO films we deployed the depth-sensitive NR technique. NR experiments were conducted on four films with 1-layer, 2-layer, 3-layer and 5-layer ITO layers deposited on fused quartz. In addition, a reference measurement was performed on a bare quartz substrate. Figure 4.7(a) displays the neutron specular reflectivity for all four ITO films as a function of the out-of-plane wave vector transfer, Q_z. Here, $Q_z = (4\pi/\lambda)\sin\alpha_i$ with λ and α_i being the wavelength and the incident angle of the neutron beam, respectively. The filled points show the experimental data with the error bars, whereas the solid lines are the best fitted curves to the data. The associated fit to the data is based on the Parratt recursion formalism [145]. The sample's reflectivity below its critical edge $Q_c < 0.012$ Å^{-1} shown in Figure 4.7(b), called the total reflection region (unity in the absence of absorption) has pronounced features determined by the distribution of the absorbing Indium atoms, thus providing an element sensitivity with depth resolution [146, 147] and confirming the uniform distribution of In.

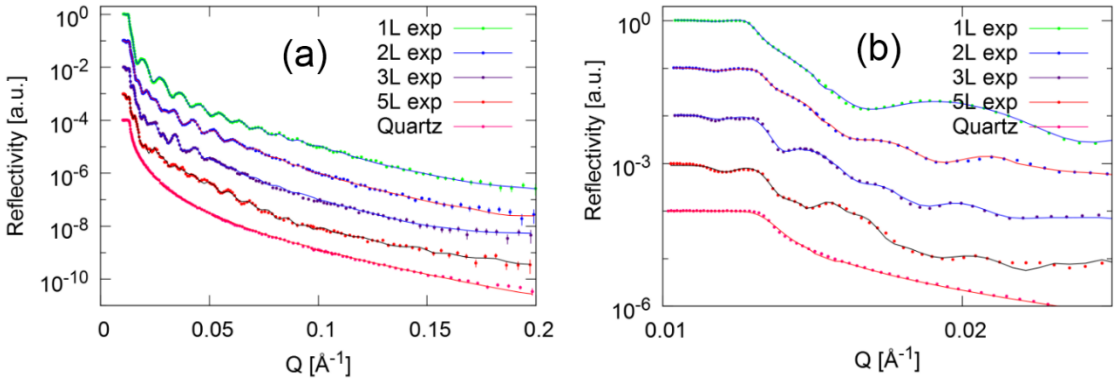

Figure 4.7. (a) Experimental and fitting results of neutron reflectivity data for 1L-5L ITO films deposited on quartz. (b) Total reflection region for figure (a) (Dots are experimental data and lines are fitting results) [128].

The depth profiles of the NSLD corresponds to the chemical (atomic) density distribution and were obtained from a fit to the data. The detailed depth, thickness and NSLD values for all four ITO films are shown in the Tables 4.1-4.4.

Table 4.1. Depth profile, NSLD and roughness for 1-layer ITO film on quartz substrate.

Depth (Å)	Thickness (Å)	Re_NSLD (10^{-6} Å^{-2})	Im_NSLD (10^{-6} Å^{-2})	Roughness	
0	59.96	0.3546	0	15.00	surface
59.96	69.61	1.408	-0.0080	8.000	
129.6	106.3	1.653	-0.011	3.500	
235.8	381.6	2.170	-0.011	50.00	
617.4	64.95	1.796	-0.011	31.00	
682.3	43.28	1.476	-0.0080	6.000	
725.6	24.61	0.2724	-0.0011	10.00	
750.2	0	3.331	0	13.00	substrate

Table 4.2. Depth profile, NSLD and roughness for 2-layer ITO film on quartz substrate.

Depth (Å)	Thickness (Å)	Re_NSLD (10^{-6} Å^{-2})	Im_NSLD (10^{-6} Å^{-2})	Roughness	
0	64.02	1.527	-0.011	25.00	surface
64.02	73.94	1.945	-0.011	18.00	
139.0	26.88	1.533	-0.0080	20.00	
164.8	509.1	2.106	-0.011	10.00	
674.0	64.14	1.330	-0.003	10.00	
738.1	118.3	3.442	-0.016	10.40	
856.4	459.0	3.653	-0.016	24.60	
1315	26.38	2.177	-0.016	10.00	
1342	13.82	1.883	-0.011	10.00	
1356	0	3.512	0	4.000	substrate

Table 4.3. Depth profile, NSLD and roughness for 3-layer ITO film on quartz substrate.

Depth (Å)	Thickness (Å)	Re_NSLD (10^{-6} Å^{-2})	Im_NSLD (10^{-6} Å^{-2})	Roughness	
0	49.51	9.193	-0.010	14.47	surface
49.51	55.30	1.518	-0.010	5.000	
104.8	624.1	2.339	-0.013	10.00	
728.9	33.48	2.129	-0.0026	20.00	
762.4	100.1	3.257	-0.013	15.00	
862.6	501.3	2.857	-0.014	28.13	
1364	16.41	2.015	-0.014	10.00	
1380	141.4	3.671	-0.016	10.00	
1522	375.7	3.837	-0.016	20.00	
1897	68.75	2.857	-0.016	25.86	
1966	0	3.620	0	20.00	substrate

Table 4.4. Depth profile, NSLD and roughness for 5-layer ITO film on quartz substrate.

Depth (Å)	Thickness (Å)	Re_NSLD (10^{-6}Å^{-2})	Im_NSLD (10^{-6}Å^{-2})	Roughness	
0	345.9	2.688	-0.010	6.764	surface
345.9	151.3	2.281	-0.014	16.19	
497.3	48.54	1.830	-0.014	14.98	
545.8	518.7	2.627	-0.013	16.35	
1065	133.6	3.100	-0.016	5.445	
1198	589.5	3.371	-0.014	5.257	
1788	99.66	3.517	-0.016	5.000	
1887	589.3	3.486	-0.015	5.000	
2477	133.9	3.535	-0.016	5.000	
2611	698.1	3.810	-0.016	6.915	
3309	66.24	2.392	-0.016	8.834	
3375	0	3.660	0	6.833	substrate

The NSLD were also plotted as functions of the depth from the surface as shown in Figure 4.8. The leftmost region in each graph represents the top ITO/air interface whereas the rightmost region corresponds to the ITO bottom film/substrate interface. Using the Igor pro scattering contrast calculator [148], we estimated the ideal (bulk) value of NSLD for ITO to be 4.090×10^{-6} Å^{-2} based on the bulk density of 7.155 g/cm^3 of ITO and neutron scattering lengths of the constituent elements, shown with the dashed line in Figure 4.8 for a fully dense ideal ITO film in each case. NR reveals that the density is not uniform through the whole film thickness and that there are very thin interfacial regions between the deposited layers with a lower NSLD value, thus we can easily identify different layers in the multi-layer ITO films. The absorption SLD (ASLD) depth profile, also shown in Figure 4.8 as red regions, represent the signature of solely the indium atoms.

Another remarkable phenomenon is a systematic evolution of an increasing density in the underlying layer with the deposition of the next layer. At the same time, in any combination of the layers, the NSLD for the top layer was consistently around 2.5×10^{-6} Å^{-2} in each ITO film. As we go from the 1-layer to the 2-layer and the 3-layer film, the NSLD for each region closest to the substrate keeps increasing. In fact, the NSLD for the bottom layer in the 5-layer ITO film was about 3.810×10^{-6} Å^{-2} which is very close to the ideal value of the bulk NSLD for ITO films (4.090×10^{-6} Å^{-2}) shown as a dashed line in Figure 4.8. The above results suggest the following scenario. The reduced NSLD of the 1-layer ITO film demonstrates that it has a very porous structure. With deposition of the next layer, the ITO solution fills into the porous regions of the previous layer. Further, the multi-layer deposition process makes the bottom layer ITO films more dense and they gradually

approach the ideal (bulk) value density of ITO films. This sequence of events is supported by the changes seen in the NC-AFM images displayed in Figure 4.6(a)-(d).

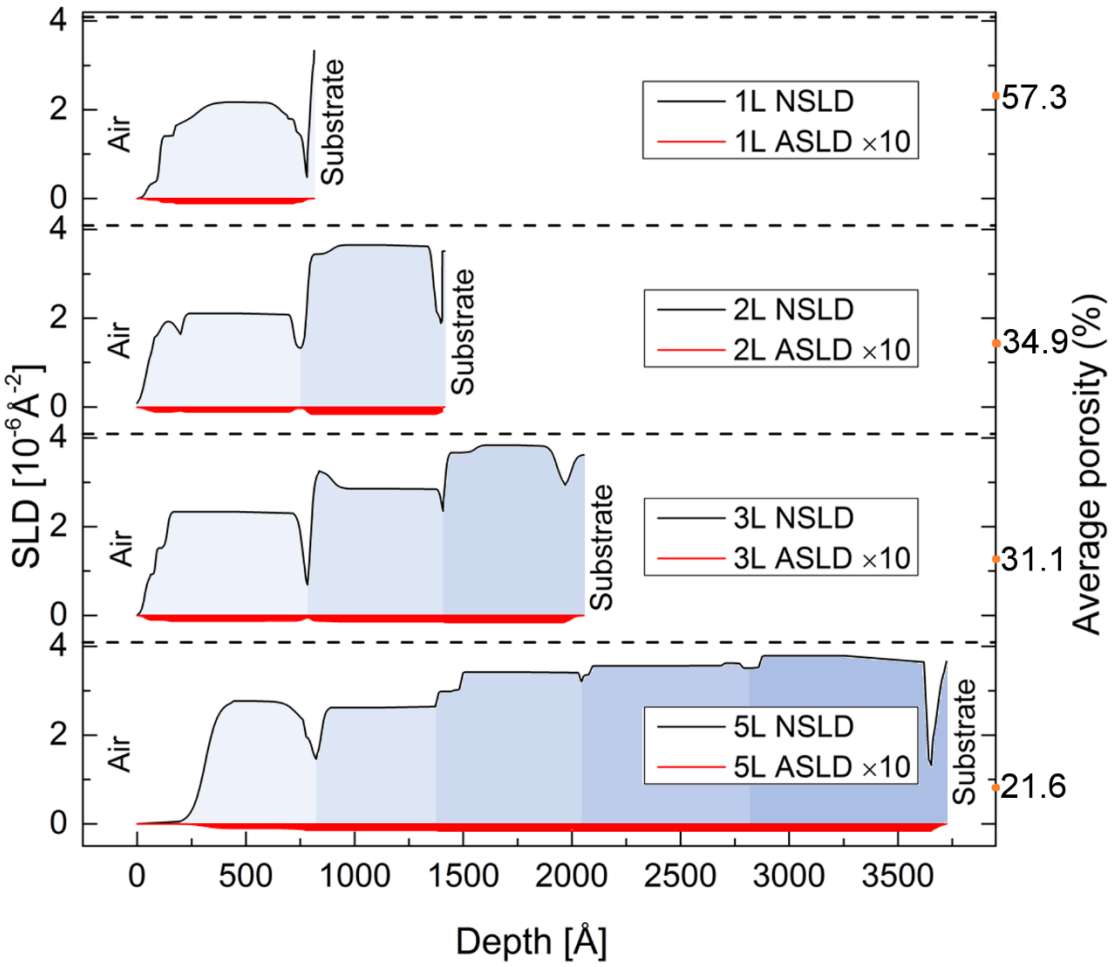

Figure 4.8. NSLD vs depth for 1-layer, 2-layer, 3-layer and 5-layer ITO film on quartz substrates from top of the film to substrate. Both NSLD (film density) and ASLD (Indium atoms) are shown. In all the images, leftmost region represents the top surface of the ITO film whereas the rightmost region is the substrate. The dashed line in each case indicates the location of the theoretical NSLD for a fully dense ITO film. The right y-axis shows the estimated average porosity for each film [128].

4.3.5 Optical properties and electrical properties

Figure 4.9 presents the optical transmission spectra of ITO films with different number of deposited layers on a quartz substrate. The optical transmission generally decreases with increasing thickness for sputtered ITO films [149]. In contrast, increasing film thickness didn't apparently decrease the overall transmittance for these solution-processed ITO films. All ITO films were highly transparent with optical transmittance higher than 85% throughout most of the visible light region. The optical transmission curves for the multi-layer ITO films tended to have wave-like features, similar to the optical properties of spin-coated ITO films discussed in Chapter 3. This might come from light interference between each deposited ITO layer [150] or it may be due to defects at the interfaces between them. Also, the pores present in each ITO layer are possibly affecting the optical properties.

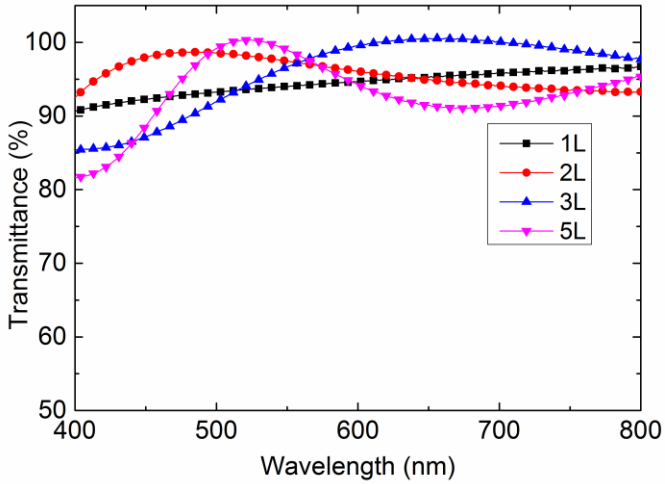

Figure 4.9. UV-Vis spectroscopy of multi-layer ITO films deposited on quartz substrates taken after annealing process. The transmittance of all films is higher than 85% in most of the visible light region [128].

The electrical properties of the ITO films were measured by 4-probe DC method, after argon annealing to ensure getting the lowest sheet resistance possible. Three measurements

were done for each sample. For the 1-layer ITO film, the average sheet resistance was 1.19 × 10^4 Ω/sq. As a comparison, the average sheet resistance for the 5-layer ITO films improved to 4.74 × 10^2 Ω/sq. The sheet resistance decreased as we increased the number of layers from 1 to 5. One of the important reasons is that the film thickness increases with the number of deposited layers. The sheet resistance values are shown in Table 4.5 together with the thickness measurements obtained from the AFM scratch tests.

Table 4.5. Average thickness for multi-layer ITO films on quartz substrates from AFM, NR and measured sheet resistivity for each sample.

	AFM thickness (nm)	NR thickness (nm)	Sheet resistance (Ω/sq)
1-layer	70 – 80	75.0	$1.19 \times 10^4 \pm 58.4$
2-layer	150 – 160	135.6	$3.19 \times 10^3 \pm 6.01$
3-layer	210 – 240	196.6	$1.69 \times 10^3 \pm 8.17$
5-layer	320 – 340	337.5	$4.74 \times 10^2 \pm 0.904$

4.3.6 Cross section

SEM was used to image the cross section of the thickest films with 3.0 kV accelerating voltage as shown in Figure 4.10. The 5-layer ITO film was well attached on the quartz substrate. Different layers could be differentiated in this high magnification image. One thing we noticed is that, even though each layer was deposited using the same spin coating recipe, the bottom layer had much larger thickness than the layers above it. The total thickness of the 5-layer ITO film was around 330– 340 nm, which agreed with the results from the AFM scratch measurements as well as neutron reflectometry results in Table 4.5.

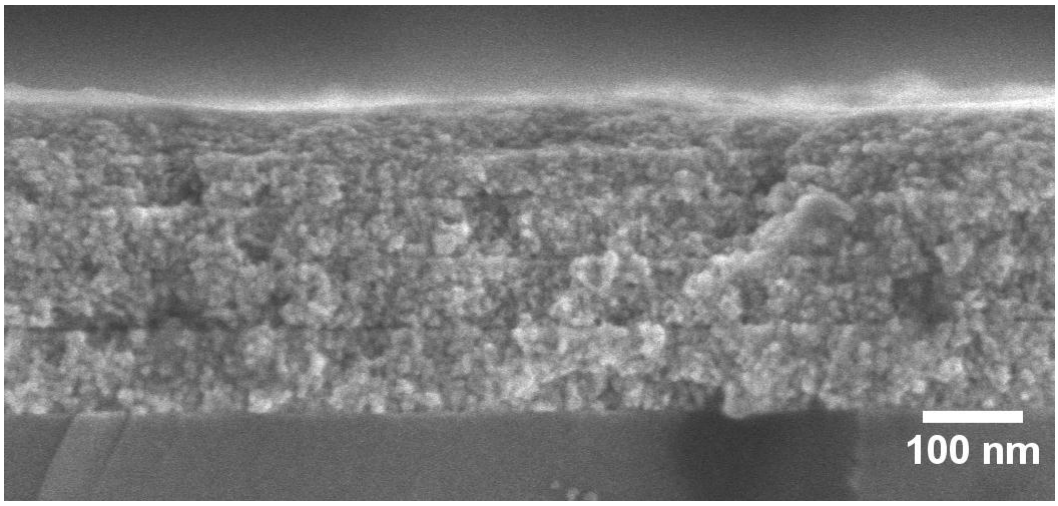

Figure 4.10. SEM cross sectional image of the 5-layer ITO film deposited on quartz, showing a total thickness of about 330-340 nm. Each deposited layer can be clearly differentiated [128].

4.4 Quantitative analysis of porosity

4.4.1 Porosity from systematic point counting

To quantitatively analyze the porosity of the 1-layer ITO film, systematic manual image point counting was first used to count the volume fraction of these big voids [151]. Four different 10 × 10 μm^2 AFM images were randomly taken on the sample surface. The dark region represents the large pores whose volume fraction was to be estimated. A test grid containing 20 test points was placed on the image at 9 systematic random locations. An example with one grid is shown in Figure 4.11(a). The statistical sample size (N) for this test is 36. The number of test points contained in the dark region ($P_p(i)$) was counted in each grid placement, where i = 1 to 36. If a test point falls on a boundary, it will be counted as 0.5.

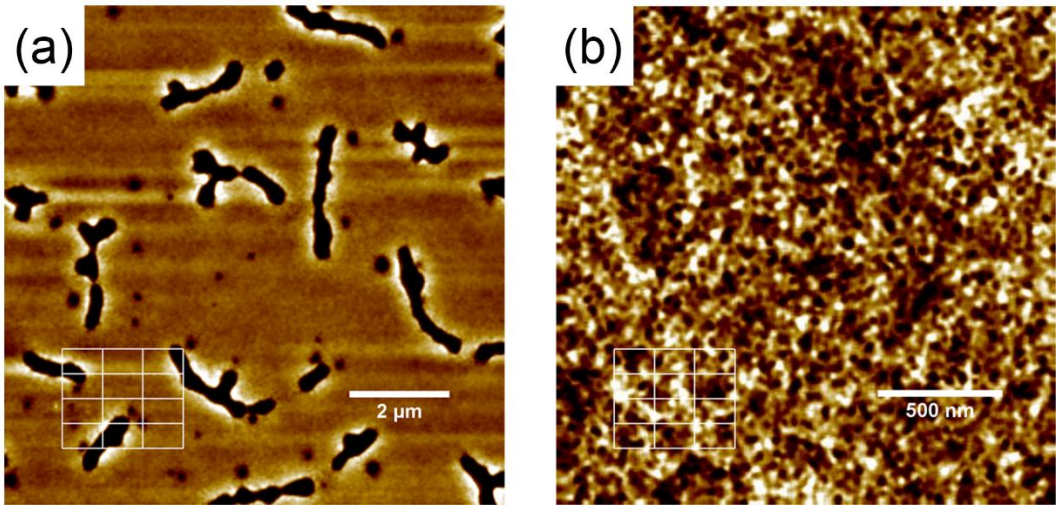

Figure 4.11. Systematic point counting for 1-layer ITO films on quartz substrates: (a) One 20-points test grid was put on a 10 × 10 μm² AFM images to count large pores. (b) One 20-points test grid was put on a 2 × 2 μm² AFM images to count small pores. (Images were flatten and smoothed to increase the contrast)

Sample average number of test points in dark region is:

$$\bar{P}_p = \frac{1}{N}\sum_{i=1}^{N} P_p(i) \tag{4.1}$$

Sample variance is:

$$s^2 = \frac{1}{N-1}\sum_{i=1}^{N}[P_p(i) - \bar{P}_p]^2 \tag{4.2}$$

There is 95% probability that the true volume fraction of the dark region (pores) is in the range [151]:

$$V_V = \frac{\bar{P}_p}{20} \pm 0.098\left(\frac{s^2}{N}\right)^{0.5} \tag{4.3}$$

The width of these big voids was around 200-250 nm whereas the length could be as long as 1-2 μm. The resulting average volume fraction was about 13.1%. When we decreased the AFM image scan size to 2 μm × 2 μm, small voids could also be identified as shown

in Figure 4.11(b). These small size voids ranged in size from 10-30 nm. Using a similar counting method as was done for the larger pores, the volume fraction of these small pores was determined to be about 32.7%. Thus, the estimated total volume fraction of pores in the 1-layer ITO film was 45.7% using the point counting method. However, it should be mentioned that this method is only a rough estimate for the 1-layer ITO film because for the multi-layer ITO films, the microstructure of the previous ITO layer affects the subsequent layers (see Figure 4.6(a, b)). Also, it can be seen that for the 5-layer ITO film (shown in Figure 4.6(d)), that the pores are well distributed and interconnected across several layers which would make point counting very difficult and most likely inaccurate.

4.4.2 Porosity from neutron reflectometry

Quantitative information on the porosity in ITO films can be readily obtained from the analysis of the detailed NSLD depth profiles. First we obtain the average NLSD for each multi-layer ITO film. As follows from the results displayed in Figure 4.8, the NSLD for each sublayer and interface in each multi-layer ITO film is different. The average NSLD ($\overline{\rho}_{NR}$) for each multi-layer ITO film was calculated with Equation 4.4 [152] using the data in Tables 4.1-4.4.

$$\overline{\rho}_{NR} = \frac{\sum_i t_i \rho_i}{\sum_i t_i} \tag{4.4}$$

where t_i is the thickness for each sublayer or interface and ρ_i is the corresponding NSLD.

Using the Igor pro scattering contrast calculator [148], the ideal bulk NSLD values for ITO and air are ρ_{NR}^{ITO} = 4.09 × 10^{-6} Å^{-2} and ρ_{NR}^{air} = 1.43 × 10^{-9} Å^{-2}, respectively.

Our samples should be chemically pure ITO films without any other phases being present, as determined by XRD analysis. Assuming the porosity is composed of air only, a simple rule of mixtures model could be applied to calculate the volume fraction of pores using the SLD [153].

$$\overline{\rho}_{NR} = V_{ITO} \times \rho_{NR}^{ITO} + V_{pores} \times \rho_{NR}^{air} \tag{4.5}$$

$$1 = V_{ITO} + V_{pores} \tag{4.6}$$

where V_{ITO} and V_{pores} are the volume fractions of ITO and air pores, respectively. Substituting the NSLD numbers, the calculated volume fraction of pores for different ITO films are shown in Table 4.6.

Table 4.6. Average NSLD, average mass density of multi-layer ITO films on quartz substrates and corresponding porosity volume fraction results.

	Average NSLD (10^{-6} Å^{-2})*	Porosity from average NSLD	Average mass density (g·cm^{-3})	Porosity from average mass density
1-layer	1.747	57.31%	3.057	57.28%
2-layer	2.662	34.93%	4.659	34.90%
3-layer	2.818	31.11%	4.932	31.08%
5-layer	3.207	21.60%	5.612	21.57%
Theoretical	4.09		7.155	

*The numbers are calculated from detailed data in Tables 4.1-4.4.

The volume fraction of pores in the 1-layer ITO films obtained from the NR calculation was 57.31%, which is higher than the number we obtained from systematic point counting (45.7%). The possible reason is that, in the point counting method, we cannot correctly account for all nanometer-sized pores within the 2 × 2 μm^2 AFM images used to estimate

the volume contributed by the smaller pore sizes revealed in Figure 4.6(e)-(f). In other words, the resolution is not as good as would be needed to quantify pores smaller than 10 nm in size. On the other hand, the NR calculation gives more accurate results as its resolution is sub-nm (Å dimensions). For the 5-layer ITO films, as determined from the NR fitted results, the total volume fraction of pores decreased to 21.60%. This is fairly close to porosity values reported in other solution-processed ITO films that were studied using other characterization methods [154, 155].

The average mass density ($\overline{\rho}_{mass}$) of the ITO films can also be derived from the NSLD values. The NSLD should be proportional to mass density when the nominal composition of the ITO films remains the same [156] as is the case here. Then the average mass density of ITO films can be calculated using Equation 4.7:

$$\overline{\rho}_{mass} = \frac{\rho_{mass}^{ITO}}{\rho_{NR}^{ITO}} \times \overline{\rho}_{NR} \tag{4.7}$$

Here we applied a rule of mixtures model again (Equation 4.8), using the average mass density [157] to calculate the volume fraction of pores. The theoretical mass density of our ITO films (ρ_{mass}^{ITO}) is 7.155 g/cm^3. The theoretical mass density of air (ρ_{mass}^{air}) is 1.2041 × 10^{-3} g/cm^3 (under 20^{o}C and 101.325kPa).

$$\overline{\rho}_{mass} = V'_{ITO} \times \rho_{mass}^{ITO} + V'_{pores} \times \rho_{mass}^{air} \tag{4.8}$$

The porosity results obtained using Equation 4.8 are also listed in Table 4.6 and are very close to the results from the NSLD calculations as should be expected.

The quantitative analysis of the porosity obtained from the NR analysis demonstrates that the ITO solution fills in the voids of the previously deposited layer (see values of NSLD increase from the 1-layer to the 5-layer films). In this way, the denser multi-layer ITO films are obtained. Additionally, the different porosity observed for each single layer might give different refractive indices. This could also be the reason we saw wave-like curves in the UV-vis spectroscopy results displayed in Figure 4.9.

For most current porosity estimation methods, a round shape and a fixed size for the ITO nanoparticles and air pores are requirements to analyze the porosity for solution-processed ITO films. In reality, the ITO nanoparticles may not be in round-shape and the sizes of the particles may vary. The annealing process may also cause the ITO nanoparticles to fuse together. Because the NSLD accounts for the atomic number density, the chemical composition and the void space simultaneously without the need to estimate particle size and shape, we conclude that the neutron reflectivity can give more accurate estimation of porosity as a whole as well as for each of the individual layers. In addition, the sheet resistance values displayed in Table 4.5 suggest that additional factors may be controlling the properties of the ITO thin films.

4.5 Correlation of porosity and electrical properties

If the multi-layer ITO films were fully dense, they would all provide the same bulk sheet resistivity (~ 3×10^{-4} Ω·cm) regardless of thickness. However, it is not the case in this study. Using the thickness data obtained in the earlier sections, the sheet resistivity of the films can be calculated from the sheet resistance and film thickness using Equation 2.4. All the sheet resistance and thickness numbers were given in Table 4.5. The best films, 5L ITO

films have an average sheet resistivity of 1.60×10^{-2} Ω·cm. It is about two orders of magnitude higher than the theoretical value of bulk ITO.

One reason for high resistivity is that ITO films were porous as described in detail earlier in this chapter. The NSLD data did also indicate that the maximum value of 4.090×10^{-6} Å^{-2} was never achieved (see dashed lines in Figure 4.8). The high porosity can weaken the contacts between the ITO nanoparticles and make the electrical paths in ITO films longer. A parallel model was used to calculate the bulk resistivity for these multi-layer ITO films [158]:

$$\frac{1}{\rho_{average}} = \frac{V_{ITO}}{\rho_{ITO}} + \frac{V_{pores}}{\rho_{air}} \tag{4.9}$$

Where $\rho_{average}$ is the measured average resistivity, ρ_{ITO} is the bulk resistivity and ρ_{air} is the air resistivity (3.3×10^{12} Ω·cm). The calculated results are shown in Figure 4.12.

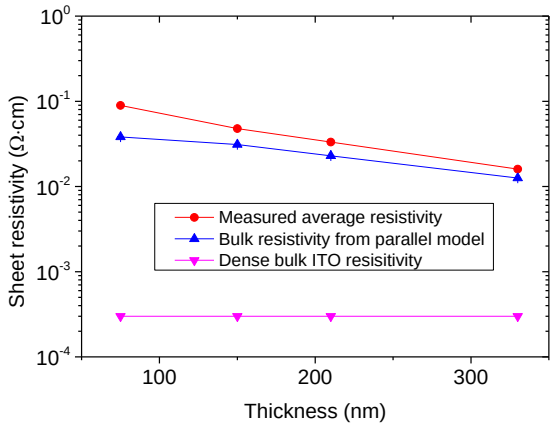

Figure 4.12. Sheet resistivity of multi-layer ITO films deposited on a quartz substrate after Ar annealing. The sheet resistivity decreased as the number of layers (i.e. thickness) was increased. After accounting for porosity obtained by NR data fitting, it is clear that the sheet resistivity is still at least one order of magnitude larger than it would be expected.

Another possible reason is that the ITO nanoparticles may not yet have reached the best

electrical properties with the current annealing process. The XRD patterns showed that the multi-layer ITO films were in polycrystalline phase but the crystallinity was not perfect. A highly crystalline material would have sharp and strong peaks instead of small and broad peaks. A higher annealing temperature using a tube furnace can improve the sheet resistivity of ITO films, which is proved in Appendix B. But the process of annealing in tube furnace will be much longer and time-consuming (includes ramping and cooling) compared to the quick hot plate annealing method, which falls out of our goal of simple and efficient processing.

4.6 Conclusion

In this chapter, multi-layer ITO films with different thicknesses on quartz substrates were fabricated by spin coating method. The ITO films had a good combination of relative low sheet resistance and high optical transmittance. The surface morphology analysis revealed that these ITO films had porous microstructures with different sizes of pores. Neutron reflectometry was first used to characterize these ITO films. The fitting of the NR data matched well with the experimental results obtained by other methods. Accurate information for film thickness, surface roughness and NSLD were obtained. The porosity of the multi-layer ITO films was quantitatively analyzed and compared to results from systematic point counting method for the 1L ITO film. While systematic point counting is only good for the 1L homogenous films, the NR characterization can be applied to all the samples to obtain more accurate average porosity data. Also, the average mass density of these ITO films were calculated from the NSLD results. It was shown that the ITO films became denser and less porous with increased number of deposited layers. A better annealing process may further improve the conductivity of multi-layer ITO films.

CHAPTER 5. ANALYSIS OF IMPEDANCE SPECTROSCOPY

5.1 Introduction

In the previous chapters, 4-probe DC method was used to measure the electrical properties of ITO films based on Ohm's law. It is usually assumed that a steady state has been reached and the measurement is time-invariant [159]. Actually, the system may not be steady under an electrical stimulation, due to different processes which may happen such as electrochemical reactions, energy storage and dissipation, transportation of charge carriers (electrons and holes) and molecular or dipolar polarization [160]. These types of information are lost during the DC measurement. To reveal the information of these processes, impedance spectroscopy (IS) needs to be used to characterize samples. IS is a powerful AC technique to characterize the complex impedance of samples by measuring the voltage (V), current (I) and phase angle (θ) over a wide frequency range using Equation 5.1 [160]:

$$Z^* = \frac{V(\omega)}{I(\omega)} = Z' + jZ'' \tag{5.1}$$

where $V(\omega) = V_m \sin(\omega t)$, $I(\omega) = I_m \sin(\omega t + \theta)$, $\omega = 2\pi f$, $j = \sqrt{-1}$. θ is the phase angle between voltage and current which can be calculated by real and imaginary impedance using Equation 5.2:

$$\theta = \tan^{-1} \frac{Z''}{Z'} \tag{5.2}$$

Three electrical elements: resistor, capacitor and inductor are commonly used to represent sample impedance in IS. Their impedances can be represented by Equation 5.3-5.5:

$$Z_R = R \tag{5.3}$$

$$Z_c = \frac{1}{j\omega C} \tag{5.4}$$

$$Z_L = j\omega L \tag{5.5}$$

Where, R is resistance, C is capacitance and L is inductance. The impedance of a resistor is independent of frequency whereas the impedances of capacitor and inductor change with different frequency. The phase angles for pure resistor, pure capacitor and pure inductor are 0°, -90° and 90°, respectively. This can help identify different circuit elements in impedance plots.

There are two main categories of impedance plots to help understand the impedance data: Nyquist plots and Bode plots. In the Nyquist plots, the real part of the data is on the X-axis and the imaginary part of the data is on the Y-axis where the imaginary part is conventionally drawn in a reversed direction. Thus the negative value of the imaginary part is in the first quadrant. Figure 5.1 shows two typical samples for Nyquist plots of impedance: parallel RC circuit and series RL circuit. A parallel RC circuit, consisting of a resistor and a capacitor in parallel, is the most typical impedance plot, which shows a semicircle in first quadrant as in Figure 5.1(a). It can represent the electric behavior of bulk material, grain boundary and thin film interfaces [161]. Series RL circuit shows a straight line in the fourth quadrant in Figure 5.1(b). Usually, series RL circuit can model the behavior of conducting materials such as metals.

Although the Nyquist plot can show real part and imaginary part at the same time, it cannot show the frequency information on the axis. Bode plots can show the impedance data as a

function of frequency. In Figure 5.2(a), the impedance magnitude of series RL circuit increases with increasing frequency from 10^4 to 10^6 Hz. In contrast, the impedance magnitude of parallel RC circuit decreases with increasing frequency at this frequency range. In Figure 5.2(b), the phase angle changes from 0 to 90° for the series RL circuit when the parallel RC circuit decreases from 0 to -90°. All this information can be used to identify resistors, capacitors and inductors in the electrical circuits [162].

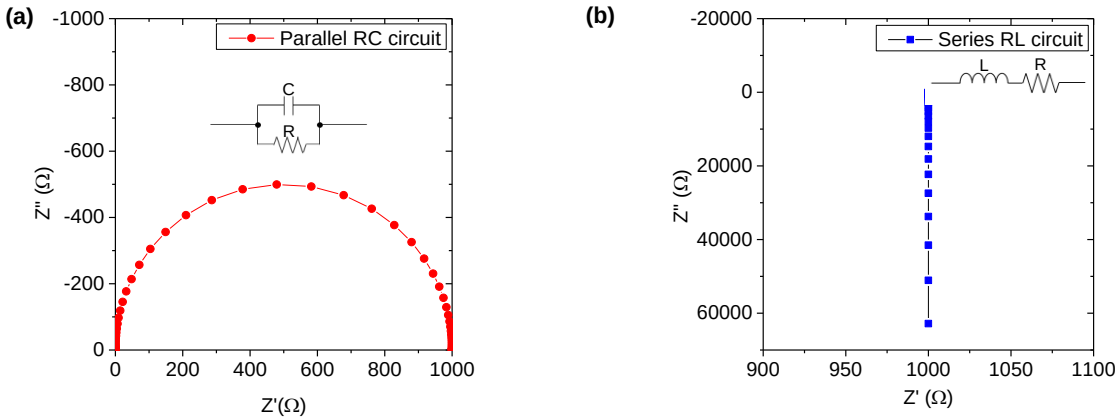

Figure 5.1. (a) Nyquist plots of impedance for (b) a parallel RC circuit (R=1000 Ω, C=1 μF); (b) a series RL circuit (R=1000 Ω, L=0.01 H). The frequency range is 1 mHz to 1 MHz.

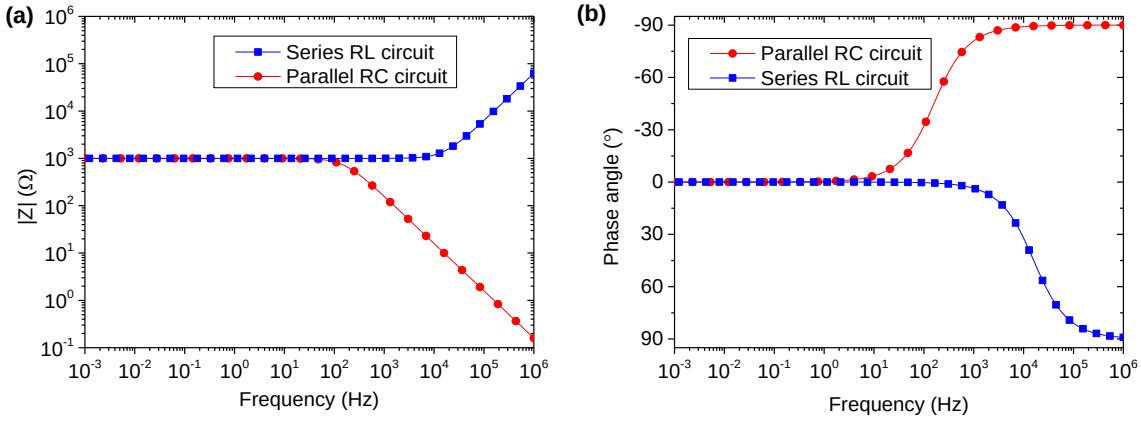

Figure 5.2. Bode plots of (a) impedance magnitude (|Z|) and (b) phase angle for a parallel RC circuit (R=1000 Ω, C=1 μF) and a series RL circuit (R=1000 Ω, L=0.01 H). The frequency range is 1 mHz to 1 MHz.

Another important information that can be obtained from the Bode plots is the relaxation time constant. The time constant is related to the transition behavior of the electrical circuits. The time constants for parallel RC circuits and series RL circuits can be calculated from the elements' values using Equation 5.6 and 5.7, respectively [163].

$$\tau = RC \tag{5.6}$$

$$\tau = \frac{R}{L} \tag{5.7}$$

Or it can be calculated from the relaxation frequency f using Equation 5.8:

$$\tau = \frac{1}{\omega} = \frac{1}{2\pi f} \tag{5.8}$$

For example, the time constant for parallel RC circuit (R=1000 Ω, C=1 μF) is 0.001 s. Thus the relaxation frequency is about 159 Hz. Around this frequency the circuit transfers from resistive behaviour to capacitive behaviour as displayed in Figure 5.2(a).

When analyzing the impedance data, other dielectric functions also need to be examined such as permittivity ε^*, admittance Y^* and modulus M^*. If only one dielectric function is used to analyze data or fit the experimental curves, the result may be incorrect [164].

In this chapter, impedance spectroscopy was used to characterize ITO films. The measurement setup was optimized to obtain data with low noise. Equivalent circuit models of multi-layer ITO films are discussed and related to their conduction mechanism.

5.2 Impedance spectroscopy results and discussion

5.2.1 Open circuit and short circuit

In this chapter, all the samples were measured inside a glove box with a controlled relative humidity (RH) of 10 ± 2% unless the RH was varied for comparison. An open circuit measurement was done on a pure quartz substrate using a 4-probe station connected with a Gamry impedance analyser as an in-plane configuration. The frequency range was set from 1 Hz to 1 MHz with a 500 mV AC voltage. Figure 5.3 shows the Nyquist plot and Bode plots for the open circuit measurement.

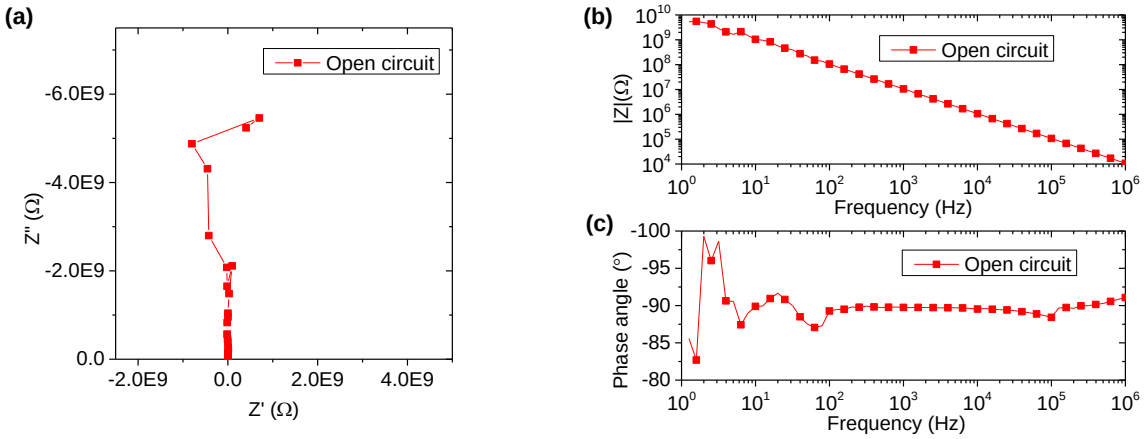

Figure 5.3. (a) Nyquist plot of impedance; Bode plots of (b) |Z| and (c) phase angle for an open circuit measured on quartz substrate.

A capacitor is the best circuit element to fit this open circuit. According to Equation 5.9,

$$|Z_c| = \frac{1}{\omega C} \tag{5.9}$$

For a single capacitor, the capacitance (C) does not change. The real part of impedance does not exist according to Equation 5.4. Therefore, the impedance magnitude ($|Z_c|$) increases with decreasing frequency. These match the Bode plots and Nyquist plot of the

open circuit measurement. The capacitance for this open circuit is about (1.60-1.64) × 10^{-11} F from calculation. This open circuit capacitance can come from the quartz substrate or the probe station or the instrument because of the in-plane configuration. Some noise peaks are observed when the impedance magnitude is higher than 10^9 Ω. Since the instrument setup is good for measuring samples between 100 μΩ to 1 MΩ, the noise at higher impedance is reasonable.

It is also important to characterize the short circuits of the measurement setup. The middle two probes of 4-probe station were shorted by touching a piece of silver foil. The AC voltage was set to 500 mV, and the frequency range was set from 1 Hz to 1 MHz.

Figure 5.4 shows the Nyquist plot and Bode plots of impedance for a short circuit. Because of the resistances from silver, cable and contact, the final impedance magnitude of this short circuit is about 1.66 Ω/sq. In theory, as a very conducting metal, the equivalent circuit for the silver should be a resistor and inductor in series (series RL), which usually shows a straight line in the 4^{th} quadrant in the Nyquist plot. However, the complex impedance of this silver had some curvature to the right. An equivalent circuit model displayed in Figure 5.4 inset was used to fit this short circuit. Z-view software was used to simulate and fit circuit models to the impedance data [165].

It is possible that the surface of silver foil had a very thin layer of oxide or sulphide [166] which contributes to the R_{ox}. This is parallel to the series elements R_{Ag} and L_{Ag} which represent the material behaviour of silver. The conducting cables also had an impact by adding a series R_0 and L_0 to the circuit.

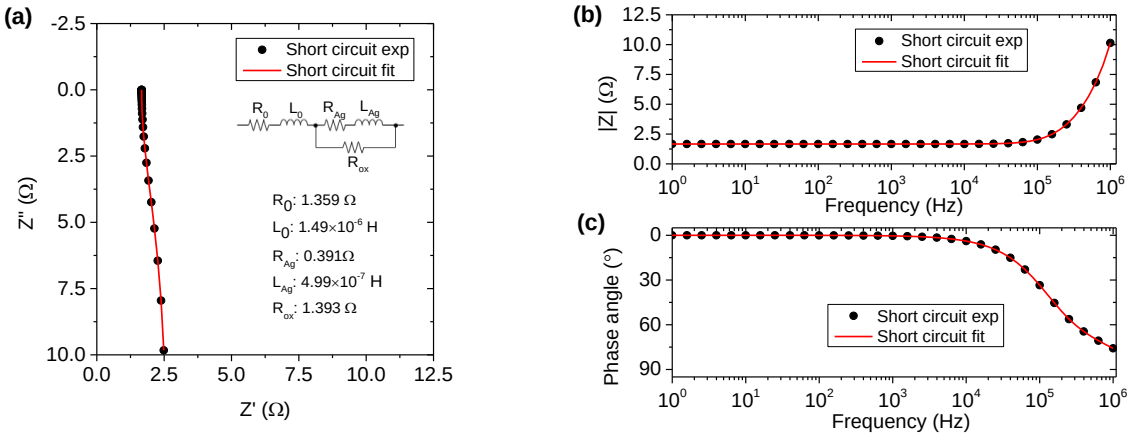

Figure 5.4. (a) Nyquist plot of impedance; Bode plots of (b) |Z| and (c) phase angle for short circuit measured on silver foil. The red curves show the best equivalent circuit fit. Inset image shows the equivalent circuit model and data for electrical elements.

Since there is no capacitive behaviour in the Bode plots, the open circuit capacitor does not need to be included. This equivalent circuit fits well with the experimental data of the silver foil short circuit in all the impedance plots. However, in the permittivity Bode plots, the fitting cannot match well with the data when the frequency is lower than 100 Hz, especially for the real permittivity Bode plot in Figure 5.5.

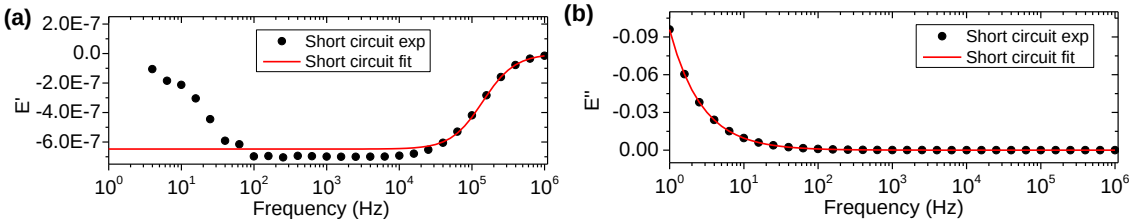

Figure 5.5. Bode plots of (a) real permittivity and (b) imaginary permittivity for short circuit. Black dots are experimental data, red curves are fitting curves (using C_g= 1).

A lot of noise peaks can be found between 1 Hz to 100 Hz in the measurement of open circuit and short circuits. This low frequency noise is common in many impedance measurements [167, 168]. The main sources of these noise are the instrument itself, the cables and the probe station. The samples also contribute some. For conducting samples,

the thermal effect induced by the current can be another reason for the low frequency noisy peaks [169]. Also, it was reported that films with notable granularity (polycrystalline) could be accompanied by a high low-frequency noise level because of the large number of grain boundaries [170]. Thus, when measuring ITO polycrystalline film samples, the frequency range 100 Hz to 1 MHz was used.

5.2.2 Effect of geometric factor

The dimensions of the sample and electrode are also important factors that can influence the measurement of impedance spectroscopy. The geometric factor (g) can be used to evaluate this dimension effect. The geometric factor can be calculated by Equation 5.10:

$$g = \frac{A}{s} \tag{5.10}$$

where A is the area of smallest current cross section and s is the electrodes spacing [171]. In this chapter, an in-plane measurement setup was used because conducting ITO films were deposited on insulating substrates. Thus no measurement can be done in a parallel-plate configuration. A simple schematic is shown in Figure 5.6.

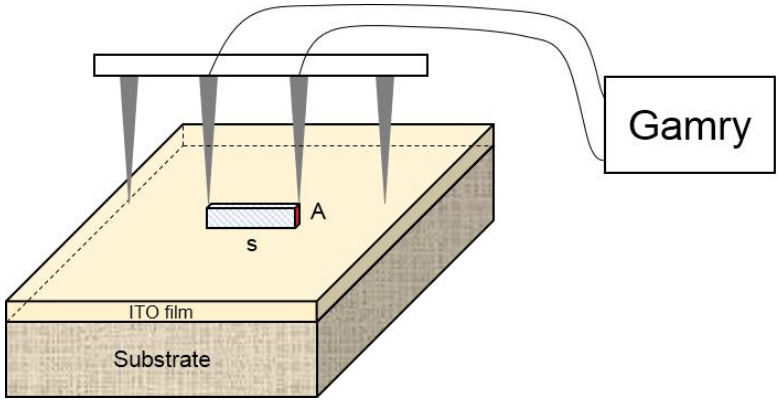

Figure 5.6. Schematic of the in-plane impedance measurement on ITO film (Blue shadow volume shows the shortest current path).

When the spacing between two probes is much larger than the film thickness, the A can be approximately calculated, using Equation 5.11 by multiplying the effective electrode length and the film thickness. Using a conducting thin film with 100 nm thickness (t) as an example, the electrode distance is 1.59×10^{-3} m (s, spacing between two probes) and the effective electrode length is fixed at 80×10^{-6} m (D, diameter of probe tips). The geometric factor is then 6.29×10^{-9} m. Thus the geometric capacitance [172] is:

$$C_g = \frac{\varepsilon_0 A}{s} = \frac{\varepsilon_0 tD}{s} = 4.46 \times 10^{-20} \text{ F} \tag{5.11}$$

where ε_0 is the vacuum permittivity (8.854×10^{-12} F/m). This geometric capacitance value is so small it is impossible to measure with current commercially available impedance instruments.

To determine the permittivity values, Equations 5.12 and 5.13 are used:

$$\varepsilon^* = \frac{1}{j\omega C_g Z^*} \tag{5.12}$$

$$\varepsilon' = -\frac{Z''}{\omega C_g \left[(Z')^2 + (Z'')^2\right]} \tag{5.13}$$

Where the impedance data is obtained from the instrument. Since C_g is in the denominator, any small fluctuation of the imaginary impedance will be enlarged in the complex permittivity data. This is especially true in the low frequency range (when ω is small), where imaginary impedance approaches zero when the lowest impedance limit for the instrument is 100 μΩ. The instrument noise or measurement limit can be the dominant data in the low frequency range of the complex permittivity plots as shown in Figure 5.5.

5.2.3 Effect of different AC voltages

In potentiostatic mode, a fixed value AC potential perturbation is applied to the sample. The impedance of the sample can be obtained by measuring the current response. For very conducting samples, a small change of AC voltage may result in a big current response and exceed the measurement range. Also, different conducting mechanisms may happen inside measured materials under different AC voltages. It was reported that the impedance of a fuel cell can be changed from an interfacial charge transfer dominant process to oxygen and gas diffusion dominant process with increasing AC voltages [173].

The 1L ITO film sample was made using a spin coating method on quartz substrate which under the same fabrication and annealing procedures described in Chapter 4. Different AC voltages were applied on the same 1L ITO film to measure the impedance as displayed in Nyquist plot Figure 5.7.

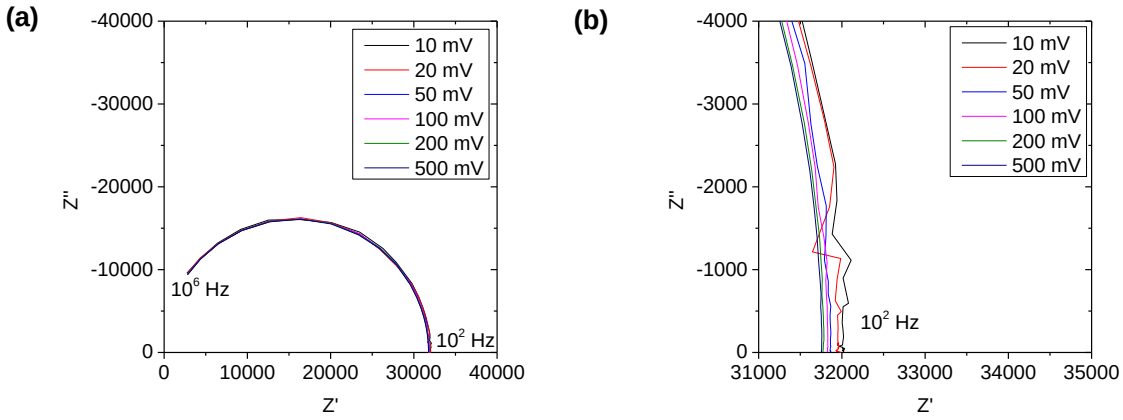

Figure 5.7. (a) Nyquist plots of impedance for 1L ITO film on quartz substrate measured under different AC voltages. (b) Magnified image of (a) at low frequency.

The characteristic feature for all these curves is a semicircle in the first quadrant. The intercepts of the semicircles with the X-axis show the real impedance value at low

frequency. With increasing AC voltage from 10 mV to 500 mV, the low-frequency real impedance values of 1L ITO film do not have any apparent changes (within 0.89% change).

Figure 5.8 shows the Bode plots of the impedance magnitude, phase angle, real impedance and imaginary impedance of same ITO film under different AC voltages. In the Bode plots of impedance magnitude, the impedance of all ITO films increases with decreasing frequency at high frequency range (10^5 Hz to 10^6 Hz) and then reaches a steady value without changing too much at lower frequency (10^2 HZ to 10^5 Hz). This is a typical behaviour in the parallel RC circuit. The Bode plots of real impedance are very similar to the magnitude plots. However, the real impedance value at high frequency is lower than the magnitude of impedance because the imaginary impedance has a big contribution to impedance magnitude at high frequency.

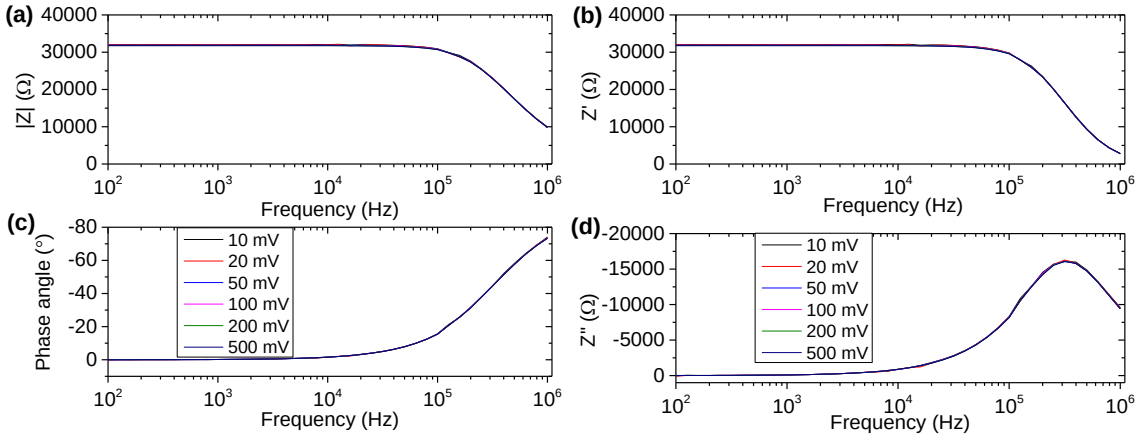

Figure 5.8. Bode plots of the (a) |Z|, (b) real impedance (c) phase angle and (d) imaginary impedance of 1L ITO film on quartz substrate measured under different AC voltages.

The Bode plots of the phase angle in Figure 5.8(c) further prove that the 1L ITO film has resistive and capacitive behaviour because the phase angle is in the range of -90° and 0°. The negative phase angle indicates the existence of a capacitive element, and the 0° phase

angle means a pure resistive behaviour. The Bode plots of imaginary impedance in Figure 5.8(d) show a relaxation peak for 1L ITO film between the frequency of 10^5 Hz and 10^6 Hz. The time constant for each relaxation peak can be calculated from the frequency value using Equation 5.8. According to the Equation 5.6, the capacitance (C) of 1L ITO film is about 1.60 $\times 10^{-11}$ F when using the low frequency impedance magnitude as R. This capacitance number is close to the open circuit capacitance number.

Although the changes of AC voltage does not apparently affect the impedance numbers for 1L ITO film, the impedance curves become smoother when using the higher AC voltages, especially in the complex capacitance plot as shown in Figure 5.9. The complex capacitance was calculated using Equation 5.14:

$$C^* = \frac{1}{j\omega Z^*} \tag{5.14}$$

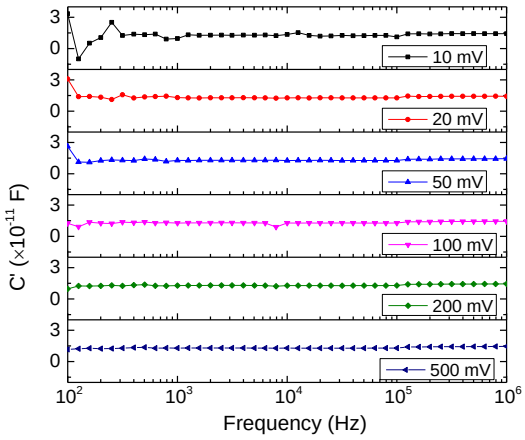

Figure 5.9. Bode plots of the real part complex capacitance of 1L ITO film on quartz substrate measured from 10 mV to 500 mV AC voltages.

It is possible that higher AC voltages can increase the signal to noise ratio. A higher AC voltage can generate higher current and more signals when the instrument noise is not

affected. The higher AC voltage also creates a stronger electric field between the probes which may force charge carriers to go the shortest route instead of traveling around the film surface. Since AC voltage always changes the bias direction, the accumulated charges may dissipate easily.

The impedance tests with different AC voltages prove that the 1L ITO film has a good electrical stability. No big changes of impedance or phenomena for charge traps can be found with varied AC voltage. A 500 mV AC voltage without DC bias was used to measure all the samples.

5.2.4 Effect of number of deposited layers

The impedance of multi-layer spin-coated ITO films was measured with 500 mV AC voltage by in-plane configuration as shown in Figure 5.10. Two different scales are used to better present all the complex impedance curves from 1L to 5L ITO films.

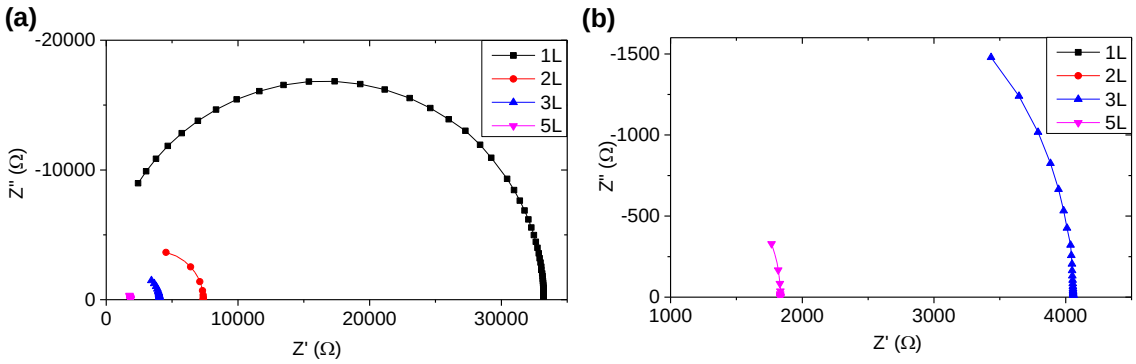

Figure 5.10. Nyquist plots of impedance for multi-layer spin-coated ITO films on quartz substrates. Different scales were used to better show all the curves.

With increasing number of deposited ITO layers, the semicircle in the first quadrant gradually shrinks to a small arc and the real impedance value decreases. Higher frequency

signals are required to get a full semicircle, but 10^6 Hz is the maximum frequency for the current instrument setup. Figure 5.11 show the Bode plots for these multi-layer ITO films. Only 1L ITO film shows a relaxation peak in the Bode plots of imaginary impedance. Again, the required frequency to see the relaxation peaks for 2L-5L ITO films is too high. All the ITO films have resistive and capacitive behaviour because the phase angle range is from -90° to 0°. The transition frequency from RC behaviour to a purely resistive behaviour are increased for ITO film with more deposited layers.

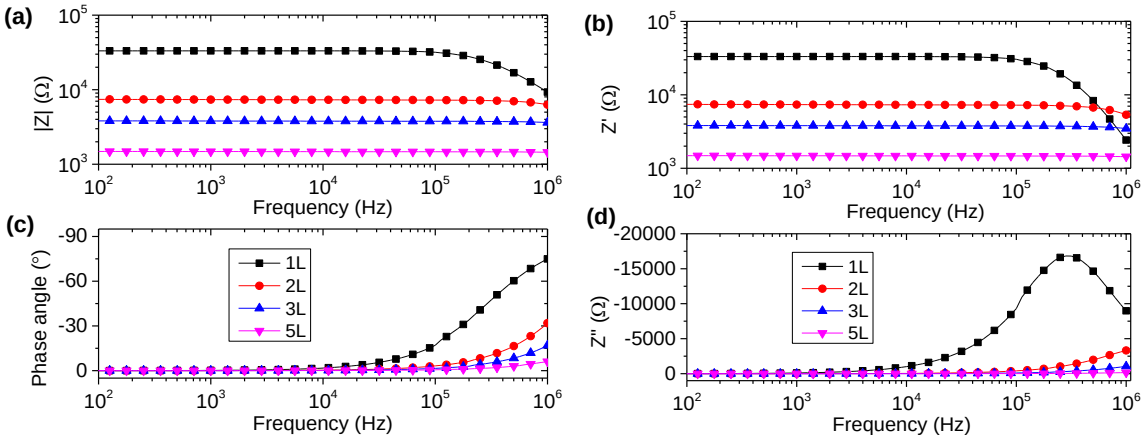

Figure 5.11. Bode plots of (a) |Z|, (b) real impedance, (c) phase angle and (d) imaginary impedance for multi-layer spin-coated ITO films on quartz substrates.

5.2.5 Effect of relative humidity

It is known that humidity can greatly affect the electrical properties of materials since pure water has an electrical conductivity of 5.5×10^{-6} S/m. Especially for insulating samples (e.g. porous silica films), they may become much more conductive under high relative humidity (RH) [174, 175]. The reason is that the water molecules from air can absorb onto the surface of the material and form a relatively conducting layer, which can greatly decrease the resistance.

The impedance of 1L ITO film was tested under different RH from 10% to 70% in a controlled atmosphere glove box as shown in Figure 5.12.

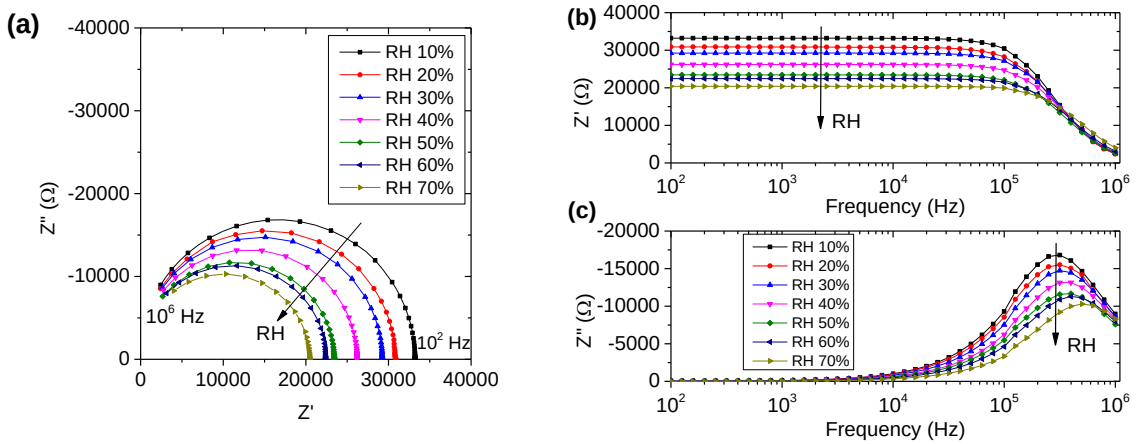

Figure 5.12. (a) Nyquist plots of impedance; Bode plots of (b) Z' and (c) Z" for 1L ITO film on quartz substrate under varied RH from 10% to 70%.

The shapes of the impedance plots are similar to previous plots. However the real impedance of 1L ITO film decreases from 3.32×10^4 Ω/sq to 2.04×10^4 Ω/sq when the RH is increased from 10% to 70%. This 62.8% impedance change cannot come from the measurement error. Considering the high porosity of 1L ITO film proved by NR in Chapter 4, it is possible that the water molecules are chemically and physically absorbed onto the porous surface ITO films under high RH. The absorbed water improved the electrical conductivity of 1L ITO film by ionic conduction of H^+ and OH^- ions. The high RH helps decrease the impedance of spin-coated ITO films more than the sputtered ITO films as shown in Table 5.1. In fact, the biggest change is observed for the 1L film which has much higher porosity (57.31%) than the 5L film (21.60%). When measuring commercial sputtered ITO glass, no obvious impedance changes are found with different RH, because the electronic conduction in the fully dense ITO layer is the dominant process. Also, the sputtered ITO films are expected to have much less porosity than the spin-coated ITO films.

It is still better to measure ITO films under low RH to remove the effect of water ionic conduction and also increase the repeatability of measurements. As Table 5.1 shows, the high RH measurements had higher standard deviations. Three measurements were done for each sample.

Table 5.1. Comparison of impedance magnitude for multi-layer spin-coated ITO films on quartz substrates and sputtered ITO films measured at high and low RH conditions.

ITO films	|Z| at RH 70% (Ω)	|Z| at RH 10% (Ω)	Change %
1L spin coating	$2.04 \times 10^4 \pm 57.3$	$3.32 \times 10^4 \pm 27.2$	+ 62.8%
2L spin coating	$5.44 \times 10^3 \pm 214$	$7.38 \times 10^3 \pm 5.63$	+ 34.9%
3L spin coating	$3.17 \times 10^3 \pm 65.7$	$4.06 \times 10^3 \pm 1.62$	+ 28.1%
5L spin coating	$1.62 \times 10^3 \pm 11.0$	$1.83 \times 10^3 \pm 1.79$	+ 13.2%
Sputtered ITO	136.1 ± 0.33	137.5 ± 0.07	+ 1.01%

5.3 Equivalent circuit simulation and fitting

5.3.1 Equivalent circuit model and simulation

In Chapter 4, the XRD results prove that the ITO films are polycrystalline films. The NR results show that ITO films have high porosity. It is assumed that ITO films are formed by loosely connected ITO polycrystalline particle spheres. Figure 5.13 shows some possible conducting mechanisms in ITO films using three typical electrical elements. The ITO intra-particle electrical behaviour can be represented by series RL circuit or parallel RC circuit. Considering ITO is a very conducting material, the intra-particle resistance should be small.

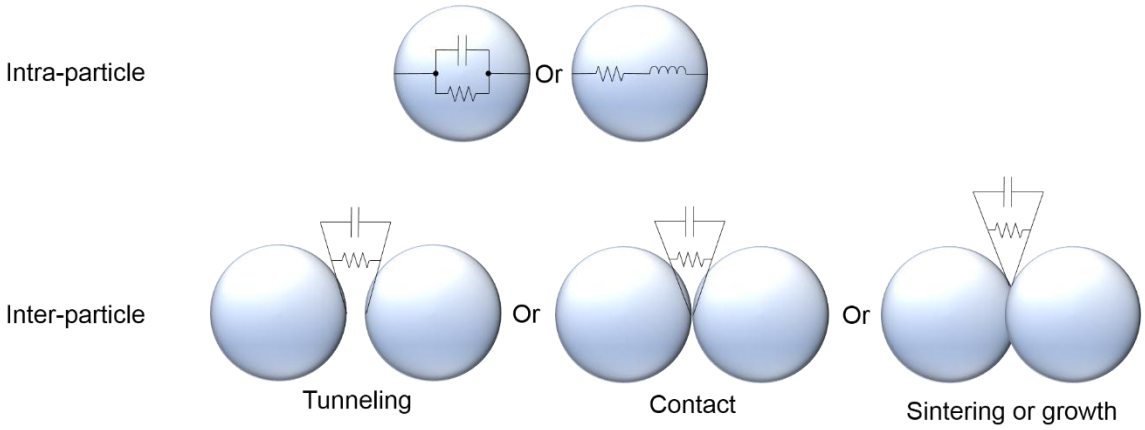

Figure 5.13. Schematics of the possible conducting mechanisms in ITO films using typical electrical elements. Schematic inspired by reference [176].

For 1L spin-coated ITO films, the ITO particles may not all have close contact because of the high porosity. During the inter-particle conduction, current can go through ITO particles which are barely contacted. Alternating, a tunnelling mechanism can happen when the distance between particles is small as shown in Figure 5.13. Under very low RH conditions (<10%), the space between ITO particles should be mainly filled with air. A parallel RC circuit can be used to represent these interfaces, but the resistance value should be much higher than intra-particle resistance when ITO particles are in contact.

As discussed in the Chapter 4, the deposition of the next ITO layer can fill some ITO ink into the porous regions of the previous ITO layer. In this way, the bottom ITO layer becomes denser and the ITO particles grow into a relatively bigger size than the top ITO layer. In addition, the bottom ITO layers have experienced longer annealing time which may cause some particle growth. Thus the contact between ITO particles can be improved by growth (or sintering process, if done at higher temperatures). When the grain boundary still exists between ITO nanoparticles, the equivalent circuit for these interfaces should still

be a resistor and capacitor in series. The resistance value should be in between the intra-particle resistance and the tunnelling interface resistance.

To better understand the electrical processes inside these multi-layer ITO films, a more detailed equivalent circuit model is required to fit the impedance plots. No inductance behaviour can be observed in the Bode plots of phase angle in Figure 5.11. If an inductor is added, the inductance should be very small so that it will not affect the impedance spectra that much. Thus the inductance is neglected in this study. The intra-particle electrical behaviour in ITO can still be represented by a parallel RC circuit. Then the equivalent circuit model for the 1L ITO film is two parallel RC circuits in series, which are R_{ITO}/C_{ITO} for intra-particle conduction and R_{grain}/C_{grain} for inter-particle conduction.

Figure 5.14 shows the in-plane configuration for IS measurements of 1L and 2L ITO films. The electric field can go through the insulating substrate but the current flow should be always in the ITO films. Since interfaces between each ITO layer always have less NSLD as shown in Chapter 4, the main current flow in each ITO layer should be parallel to each other.

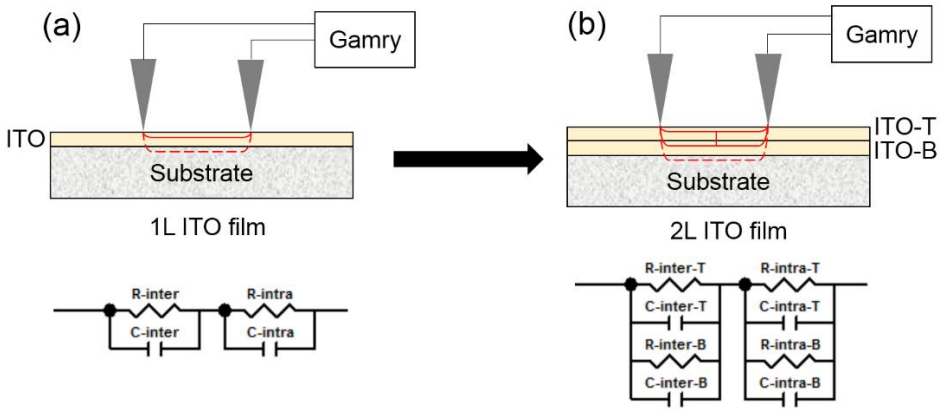

Figure 5.14. In-plane configuration for IS measurements of (a) 1L and (b) 2L ITO films. Simplified equivalent circuit for each film is shown below the film schematics.

It is also possible that the current flow can go across the interface between ITO layers when the interfaces have some points with good contact. Thus the electrical elements in each ITO layer can be in parallel or in series with the elements in another ITO layer as displayed in Figure 5.14(b). Parallel combination of electrical elements can be calculated by Equation 5.15 and 5.16:

$$\frac{1}{R_{parallel}} = \frac{1}{R_1} + \frac{1}{R_2} \tag{5.15}$$

$$C_{parallel} = C_1 + C_2 \tag{5.16}$$

Where R_1 and R_2 are two parallel resistors, C_1 and C_2 are two parallel capacitors. The equivalent circuit in Figure 5.14b can be simplified into a two parallel RC circuit in series.

A full equivalent circuit model for 1L ITO film can be drawn as in Figure 5.15. R_0 is the combination of contact resistance, cable resistance and instrument compensation resistance. Two parallel RC circuits in series represent the impedance behaviour inside ITO films. C_0 is the open circuit capacitance which should be parallel to the ITO films. This capacitance also becomes the experimental limitation for in-plane measurements of ITO thin films. Different situations can happen with different values of open circuit capacitance. A simulation for the influence of open circuit capacitance is shown in Figure 5.16.

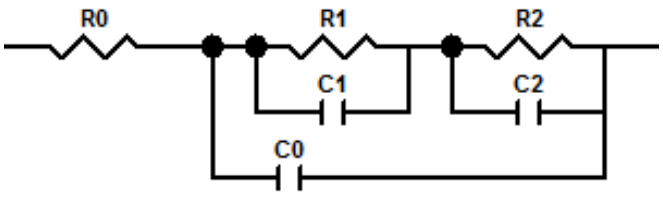

Figure 5.15. A full equivalent circuit model for 1L ITO film.

If the open circuit capacitance (C_0) is much smaller than intra-particle (C1) and inter-particle (C2) capacitance (about 3 orders of magnitude smaller), it should have a very small impact on the experimental impedance data of ITO films (Figure 5.17(a)). Then this capacitance can be neglected in the circuit. The equivalent circuit can be simplified to two RC parallel in series, and therefore it is easier to separate two dielectric relaxations (RC parallel) in ITO films.

If the open circuit capacitance (C_0) is much larger than the capacitance in ITO films (about 3 orders of magnitude larger), it will dominate the experimental capacitance data of ITO films (Figure 5.17(b)). In this situation, the intra-particle and inter-particle capacitance cannot be separated since all the small capacitance information is covered by the large capacitance information (Figure 5.16(b, c)). Thus, the final equivalent circuit model is simplified to (R1 + R2) in parallel with open circuit capacitor C_0.

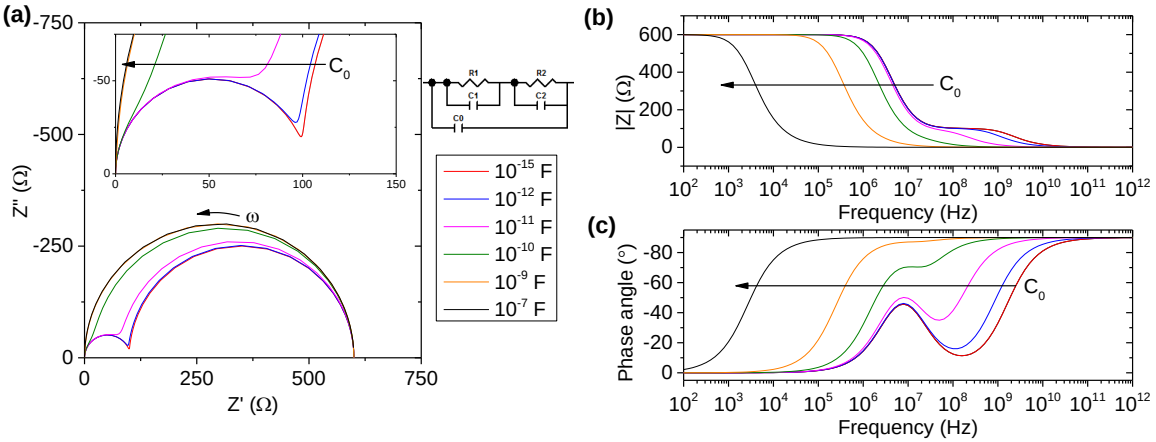

Figure 5.16. Impedance plots from simulated data to demonstrate the influence of open circuit capacitance. (a) Nyquist plots of impedance; Bode plots of (b) |Z| and (c) phase angle for equivalent circuit (inset) with different open circuit capacitance C_0. All other circuit elements are fixed: R1 = 100 Ω, R2 = 500 Ω, C1 = 10^{-12} F, C2 = 10^{-10} F. The frequency range is from 10^{12} Hz to 100 Hz. (R_0 was neglected in simulation since it only change the horizontal displacement of spectra without affecting the shape)

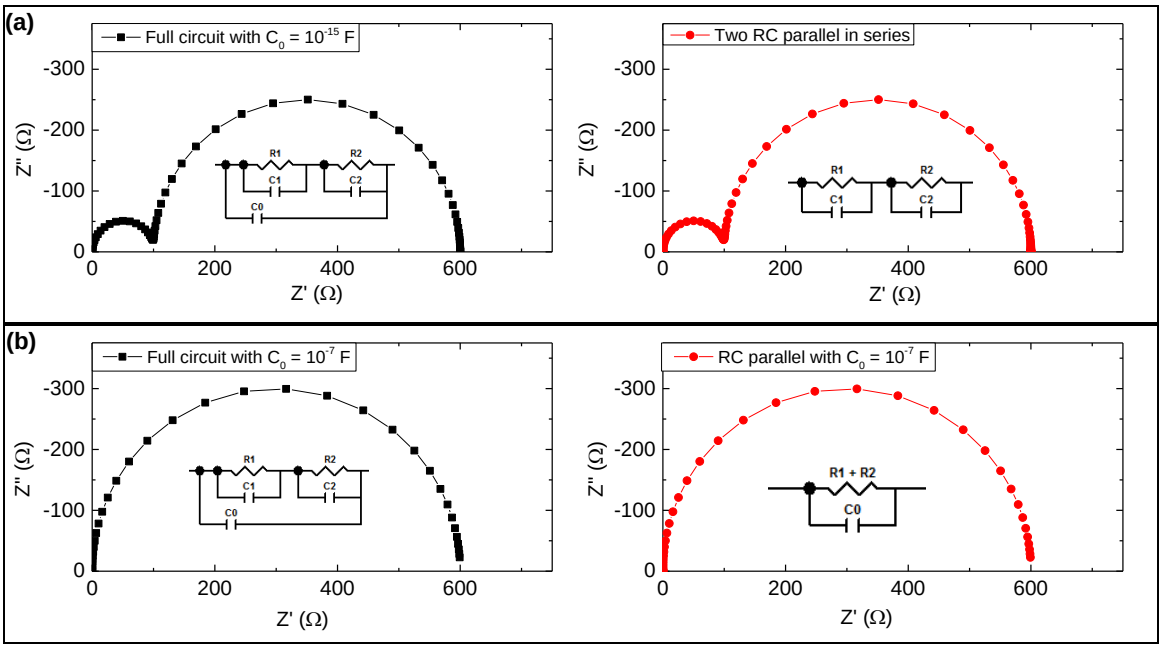

Figure 5.17. Comparison of Nyquist plots for two equivalent circuits (inset) with (a) $C_0 = 10^{-15}$ F; (b) $C_0 = 10^{-7}$ F. All other circuit elements are fixed: R1 = 100 Ω, R2 = 500 Ω, C1 = 10^{-12} F, C2 = 10^{-10} F. The frequency range is from 10^{12} Hz to 100 Hz.

Another situation is that the open circuit capacitance may be similar to the capacitance in ITO films (some cases are shown in Figure 5.16a). It is possible to separate two RC parallel behaviours with a defined open circuit capacitance. However, the open circuit capacitance is not easily defined because most impedance instruments show large noise for high impedance measurement. Only a rough estimation for open circuit capacitance can be obtained. Also, the capacitor in ITO films may interact with open circuit capacitor and show only one imperfect capacitor behaviour in the impedance plot (C_0=10^{-9} F curve in Figure 5.16a). This combined capacitor can be represented by a constant phase element (CPE).

CPE is non-ideal capacitor to compensate for inhomogeneity in the system such as surface defects, charge inhomogeneities, phase separation, variation in compositions and

stoichiometry [177]. The impedance of a CPE element can be expressed by Equation 5.17 [178]:

$$Z = \frac{1}{Y_0(i\omega)^n} \tag{5.17}$$

Where, Y_0 is a constant and n is the CPE power index ($0 \leq n \leq 1$). When n = 1, the CPE converts to a perfect capacitor. Thus, if CPE has to be used to represent the capacitor behaviour in ITO films, capacitance in ITO films may be similar to open circuit capacitance.

In the simulation, it is possible to separate the open circuit capacitance from the main circuit capacitance if the C_0 is about same order of magnitude with C1 or C2 as well as having a wide range of measured frequency. When C_0 is bigger than this, the separation for C1 and C2 will not be accurate.

5.3.2 Equivalent circuit fitting

A simple equivalent circuit model of parallel RC circuits in series with R_0 was used to fit the experimental impedance data for 1L ITO film and shows a good fitting in the impedance Nyquist and Bode plots in Figure 5.18. This model also fits well with other dielectric functions which can be found in Appendix B. CPE function is not required since the ideal capacitor fit well. The fitting data of capacitor C is about 1.602×10^{-11} F which is similar to the open circuit capacitance number. It is possible that the open circuit capacitance is larger than the capacitance in ITO films and dominate the IS data, which was discussed in the previous simulation.

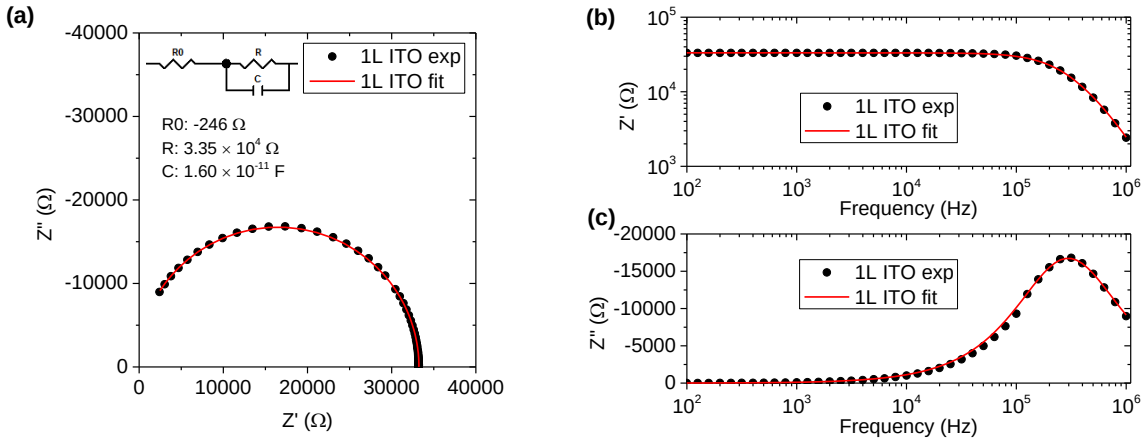

Figure 5.18. (a) Nyquist plot of impedance; Bode plots of (b) Z' and (c) Z" with equivalent circuit fit results for 1L ITO film on quartz substrate. Black dots are experimental data, red lines are fitting curves. Inset picture was equivalent circuit model and the fitting data.

Actually, we can roughly estimate the value of ITO intra-particle capacitance with the geometric capacitance using Equation 5.18 [179]:

$$C_{Intra} = \frac{\varepsilon_r \varepsilon_0 A}{d} = \varepsilon_r C_g \tag{5.18}$$

Where ε_r is the relative permittivity of bulk ITO and C_g is geometric capacitance. The ε_r of ITO is 4.0 at high frequency [180] and 9.0 at low frequency [181]. Thus the intra-particle capacitance of 1L ITO films should be in the range of 1.82×10^{-19} F to 4.10×10^{-19} F. This is eight orders of magnitude smaller than the open circuit capacitance (1.6×10^{-11} F). The inter-particle capacitance should be bigger than the intra-particle capacitance in this 1L polycrystalline ITO films considering the air between the ITO nanoparticles. If the ITO particles contact to each other, Equation 5.19 can be used to derive inter-particle capacitance [182].

$$C_{inter} = C_{Intra} \times \frac{d_{Grain}}{d_{GB}} \tag{5.19}$$

Where d_{Grain} is the size of ITO nanoparticle and d_{GB} is the thickness of grain boundary between ITO particles. Considering only one layer atoms as a grain boundary, the smallest thickness of grain boundary is about 0.5 nm (van der Waals radius of indium is about 0.225 nm). The size of ITO nanoparticle is about 15 nm. Then the estimated inter-particle capacitance can be 30 times (~10^{-17} F) larger than the intra-particle capacitance. However, it is still considerably smaller than the open circuit capacitance.

The obtained resistance (R) should be a combination of inter-particle resistance (R_{inter}) and intra-particle resistance (R_{intra}) because the equivalent circuit in Figure 5.15 simplified to RC parallel. It is interesting to find that the R_0 is a negative number. Actually, negative resistance is a widely reported topic in the literature [183, 184]. The cable resistance cannot be negative. Thus the negative value should come from the instrument compensation or contact resistance. For the instrument compensation part, it was noticed that the negative value showed up in the real impedance of open circuit measurement at high frequency. For contact resistance, a partial Schottky barrier may form between the conducting tungsten carbide (WC) probe electrode and semiconducting ITO films beside the ohmic contact [185]. The negative resistance may be explained by an avalanche multiplication at the edge of the depletion region of a W-ITO contact [186]. However, from the FEA simulation in the next chapter, it is found that the contact resistance should be a large positive number and contributes to the obtained resistance R. Thus the instrument compensation should be the main reason for the negative R_0 numbers.

Figure 5.19 shows the Nyquist plot and Bode plots of impedance for 5L ITO films with fitting results. The fitting curves using CPE-modified equivalent circuit model match well with the experimental data for the 5L ITO film. The reason for using the CPE function

instead of pure capacitor should be mainly attributed to presence of the interfacial layer defects in the multi-layer ITO films. With increasing number of interfaces between ITO layers, the capacitor behaviour is slightly deviated from the ideal situation. The film's intrinsic capacitance may have a partial contribution to this.

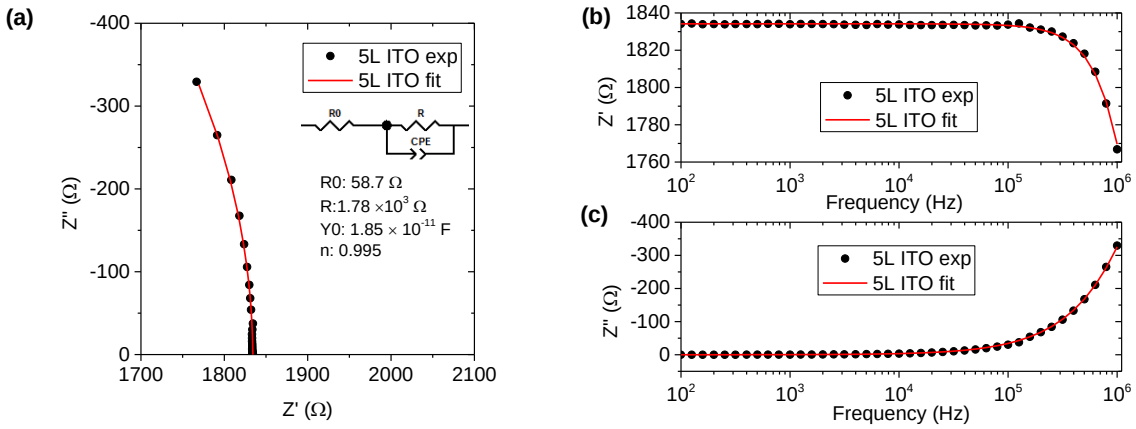

Figure 5.19. (a) Nyquist plot of impedance; Bode plots of (b) Z' and (c) Z" with equivalent circuit fit results for 5L ITO film on quartz substrate. Black dots are experimental data, red curves are fitting curves. Inset picture is modified circuit model.

All the fitting data of electrical elements in equivalent circuit for multi-layer ITO films are listed in Table 5.2. The standard deviation was obtained from fitting function of Z-view software. The R_0 gradually increases and becomes positive because 5L ITO films are more conducting than 1L ITO films. With increasing number of deposited layers, the combination of intra-particle and inter-particle resistance (R) was decreased from 3.35 × 10^4 Ω to 1.78 × 10^3 Ω. The capacitance value in CPE is similar to the open circuit capacitance. However, it is slightly increased from 1L to 5L ITO films which means that the capacitance of interfacial defects in ITO films has an influence on the total capacitance.

Table 5.2. Fitting data of electrical elements in equivalent circuit model for multi-layer ITO films on quartz substrates from Chapter 4.

ITO layers	R_0 (Ω)	R (Ω)	Y_0 (10^{-11} F)	n
1L	-246 ± 29.6	3.35×10^4 ± 32.9	1.60 ± 0.004	1
2L	-182 ± 17.2	7.56×10^3 ± 16.7	1.64 ± 0.007	0.999
3L	-126 ± 23.3	4.18×10^3 ± 23.0	1.65 ± 0.019	0.997
5L	58.7 ± 4.26	1.78×10^3 ± 42.5	1.85 ± 0.089	0.995

To fully separate the inter-particle capacitance and intra-particle capacitance from the open circuit capacitance, the only possible way is to increase the geometric capacitance. Considering Equation 5.11, we can increase the electrode length or decrease the electrode spacing when the film thickness is fixed. The maximum length for the electrodes can be the ITO film sample size (2.54×10^{-2} m), which is about 300 times larger than the probe diameter. To make the inter-particle capacitance similar to the open circuit capacitance, the spacing between two electrodes should be minimized to about 500 nm (1/3000 of the original spacing). Also, the electrodes should be as thin as possible to reduce the effect on the electrical properties of ITO films. Thus, a pair of long and thin electrodes with narrow spacing are required to separate intrinsic film capacitance for in-plane impedance measurements.

Other types of measurement configurations should be considered such as parallel-plate configuration. The electrode size can be enlarged and the spacing between electrodes can be minimized in the parallel-plate configuration. Thus the geometry capacitance can be increased as well as the intrinsic film capacitance. However, the ITO films are on the insulating quartz substrate, the parallel-plate measurement will be dominated by the large resistance and capacitance from the insulating substrates. Thus the ITO films must be

deposited onto conducting substrates such as metals. The possibility of these measurement configurations and different electrodes is discussed in the next simulation chapter.

5.4 Comparison of sheet resistance result from AC and DC methods

The low frequency impedance magnitude is always being used as the sheet resistance for thin films in the impedance spectroscopy. By measuring the same ITO films using AC method (2-probe AC IS) and DC method (4-probe DC resistance measurement) using the same four-probe station, we found that the sheet resistances value from AC method are always slightly bigger. Table 5.3 shows the sheet resistance comparison between the two methods using multi-layer spin-coated ITO films from Chapter 4 as an example. Each sample was measured at least 3 times and the average number was used. Similar current value was used in the two methods. The DC sheet resistance is higher than the data in Chapter 4 because these samples were measured several weeks after Ar annealing process and had reached a steady state.

From Table 5.3, the sheet resistance ratio between AC method and DC method is about 1.40 to 1.58. Several reasons may cause this difference. First, the AC method only uses 2-probe configuration and the measured impedance includes cable resistance, probe resistance and contact resistance. Second, the AC method takes a longer time to measure the same sample which may cause resistive heating [187]. The increasing temperature may increase the sheet resistance of ITO films. Last, the skin effect may happen inside ITO film during IS measurement. AC currents tend to go through the surface instead of passing inside of the conductor [188]. This will reduce the effective current cross-sectional area and thus increase the measured impedance.

Table 5.3. Comparison of sheet resistances from AC method and DC method for multi-layer spin-coated ITO films on quartz substrates (Obtained from the average).

ITO layers	AC method (Ω/sq)	DC method (Ω/sq)	AC/DC ratio
1L	$3.35\times10^4 \pm 32.9$	$2.39\times10^4 \pm 0.49$	1.40
2L	$7.56\times10^3 \pm 16.7$	$5.14\times10^3 \pm 0.026$	1.47
3L	$4.18\times10^3 \pm 23.0$	$2.63\times10^3 \pm 0.030$	1.58
5L	$1.78\times10^3 \pm 42.5$	$1.14\times10^3 \pm 0.064$	1.57

Thus, in order to get accurate sheet resistance value for ITO films, the 4-probe DC resistance measurement method should be used. However, the AC IS method is better to understand the electrical microstructure inside ITO films.

5.5 Conclusion

Impedance spectroscopy was used to characterize the multi-layer ITO films reported in Chapter 4. The measurement conditions were optimized to obtain repeatable and reliable impedance results. The conducting mechanism in ITO films should consist of intra-particle and inter-particle conduction. During IS simulation, it was found that the open circuit capacitance can dominate the film impedance. The fitting results of the experimental measurements proved that the obtained film capacitance had a value similar to open circuit capacitance. The estimated film intrinsic capacitance using geometry capacitance further provided evidence that intrinsic film capacitance is much smaller than the open circuit capacitance. Some possible solutions were discussed which might increase the geometric capacitance and help separate ITO intra-particle and inter-particle capacitance. Last, a comparison was made between DC resistance and AC impedance. It was shown that DC electrical measurements give more accurate sheet resistance values for ITO films, whereas AC measurements are more affected by several artifacts.

CHAPTER 6. IMPEDANCE AND CAPACITANCE SIMULATION OF ITO FILMS BY FINITE ELEMENT ANALYSIS

6.1 Introduction

Finite element analysis (FEA) is a computerized method for simulating and analyzing problems in engineering and mathematical physics. In FEA, a large domain of the problem is subdivided into small and simple finite elements which can be represented by element equations to model most closely the actual behavior. By systematically solving and recombining all these element equations into a large system of equations, the numerical answer is obtained for the original problem [189]. As a computer-based method, the FEA has several advantages that make it very popular. For general situations, small computers and short programs are able to solve the problems quickly with low development cost. With increasing computer calculation ability, irregular material shapes and complicated systems can be simulated by separating into small element problems in FEA. Most importantly, any additions and changes can be made into existing models quickly and inexpensively [190].

With the above stated advantages, FEA has been widely used to analyze structural problems for bulk materials including stress analysis, vibration analysis and impact problems, as well as nonstructural problems such as heat transfer, fluid flow and distribution of electrical or magnetic potential [190]. Recently, FEA has been extended to study materials with nanoscale dimensions like thin films [191, 192]. The electrical properties of thin films can be predicted from the simulation to assist the experimental measurements. For example, Kumar and Gerhardt [193] reported on the influence of

geometric parameters on the impedance behavior for insulating SiO_2 thin films on conducting Si substrates by FEA. Different electrode sizes and film thicknesses can cause orders of magnitude change in the measured film impedance and capacitance, whereas using thicker or thinner substrate thickness does not affect the impedance measurements significantly. It was also found that small electrode size and large film thickness can cause large measurement error in the simulation cases [192].

Most studies of electrical properties for ITO films have been based on the experimental data and very few electrical simulation have been reported [194]. ITO films are usually deposited on insulating substrates. Thus the electrical behavior is completely different from the situations of insulating films on conducting substrates. In this chapter, ITO films with different measurement configuration, geometric dimensions and electrode sizes were studied by FEA using 2D and 3D models.

6.2 Modeling steps

COMSOL Multiphysics 5.3 was applied as the FEA tool in this chapter. The impedance measurement usually uses AC voltage and is frequency-dependent. Thus the simulations here used a Bi-conjugate gradient stabilized iterative solver [195] in the ac/dc module in a frequency domain study, which implements a finite element method to solve partial differential equations. The goal is to solve the Maxwell's Equation 6.1 in terms of electric potential (V) [191].

$$-\nabla \cdot \left((\sigma + \varepsilon_r \varepsilon_0 \frac{\partial}{\partial t})\nabla \mathrm{V}\right) = 0 \tag{6.1}$$

Where σ is the electrical conductivity of the material, ε_r is the relative permittivity of the material, ε_0 is the vacuum permittivity (constant value: 8.854×10^{-12} F/m). The problem then is reduced to solving the electric potential in each finite element domain. An AC voltage signal (0.5V, 0.1 Hz-10 MHz, 10 points per decade) was added to the terminal electrode and the ground electrode had zero potential as a 2-probe method. The current flowing from terminal to ground electrode was extracted. The admittance (Y) can be derived between the terminal electrode and ground electrode using the functions in COMSOL software. Other dielectric properties such as impedance (Z) and capacitance (C) can also be calculated using Equations 6.2 and 6.3:

$$Z^* = \frac{1}{Y^*} = Z' + jZ'' \tag{6.2}$$

$$C^* = C' + jC'' = \frac{Y''}{\omega} + j\frac{Y'}{\omega} \tag{6.3}$$

Some standard values of the relative permittivity and electric conductivity used in this chapter are listed in Table 6.1. These numbers are kept as constants throughout the whole chapter unless otherwise given. One important assumption is that ITO film is treated as a homogeneous layer without any porosity.

The procedure for the modeling setup in FEA is:

a. Choosing the 2D or 3D model and ac/dc electric currents interface in the COMSOL model wizard;
b. Drawing ITO films model with or without environment;
c. Building the appropriate mesh for the model;

d. Defining the conductivity and relative permittivity for each domain and boundary conditions;

e. Computing the model by the solver in the frequency domain study;

f. Converting the calculated data into admittance and other electrical properties.

Table 6.1. Relative permittivity and electrical conductivity for different materials used in the simulation

Materials	Relative permittivity	Electrical conductivity (S/m)	Reference
Air	1.00059	3×10^{-15}	[196]
Quartz glass	4.2	1×10^{-12}	[197]
ITO	4[a]	1180[c]	[180]
Tungsten Carbide	1[b]	5.0×10^{6}	[198]

[a,b] For conductors, the relative permittivity is not constant at different frequency. To simplify the calculation, the relative permittivity for ITO and WC are fixed at 4 and 1.

[c] An average experimental value of solution-processed 1L ITO films after Ar annealing treatment.

6.3 Results and discussion

6.3.1 Effects of different measurement configurations for ITO film

The impedance spectroscopy of samples can be obtained from different measurement configurations. A FEA simulation of different measurement configurations can predict the impedance results and guide the experiments. Parallel-plate measurement and in-plane measurement are two common configurations for impedance measurement. They are both possible for ITO film impedance measurement. In a parallel-plate measurement simulation, ITO film is deposited onto WC substrates. Another WC plate is put on top of ITO film to form a sandwich structure as shown in Figure 6.1.

Two square WC plates have the same size of 12.7 mm × 12.7 mm and thickness of 1 mm (which is common value for substrate thickness). The ITO film is also 12.7 mm × 12.7 mm but the thickness is 10 μm. The electrical parameters were listed in Table 6.1. The top WC plate serves as terminal electrode and the bottom WC plate is the ground electrode. The electrical response of the system can be simulated.

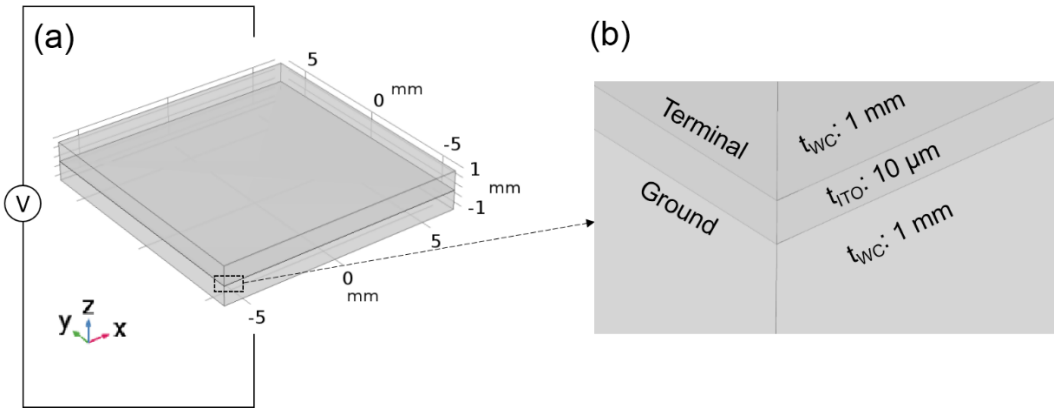

Figure 6.1. (a) 3D model geometry for parallel-plate measurement configuration; (b) magnified figure to show sandwich structure. (12.7 mm × 12.7 mm × 1 mm WC plates, 12.7 mm × 12.7 mm × 10 μm ITO film)

Figure 6.2 shows the electric potential map for the parallel-plate measurement configuration at 1 Hz from the FEA simulation results. The top WC plate has a constant electric potential of 0.5 V where the potential of the bottom WC plate is 0 V. The electric potential drop is found mainly on the ITO film as shown in Figure 6.2(c) because the ITO film has much larger resistance than the WC plates. The electric field lines vertically pass through the ITO films and are presented by the dots shown in Figure 6.2(b).

In-plane measurement is another configuration for ITO film impedance measurement. A probe station is required to work as electrodes on top (Figure 6.3). In the actual simulation, the thickness of the electrode was ignored to reduce the number of mesh elements. No contact resistances were added between electrodes and ITO film to simplify the simulation.

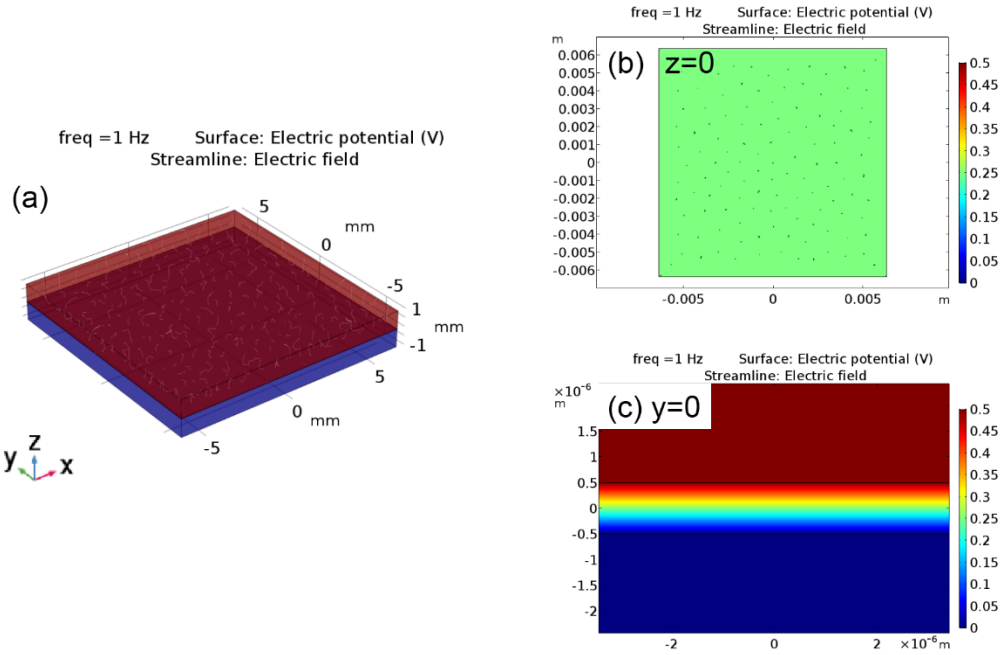

Figure 6.2. Simulated electric potential map and field lines for parallel-plate measurement configuration at 1 Hz: (a) 3D electric potential map; (b) 2D surface map at z=0; (c) 2D surface map at y=0.

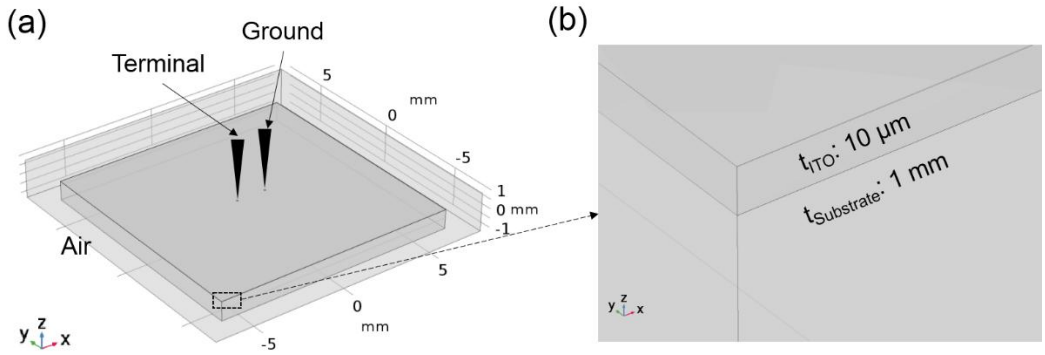

Figure 6.3. (a) 3D model geometry for in-plane measurement configuration; (b) magnified figure to show ITO film on substrate. (15 mm × 15 mm × 2 mm air, 12.7 mm × 12.7 mm × 10 µm ITO film, 12.7 mm × 12.7 mm × 1 mm substrate, D = 80 µm circular electrodes with a center spacing of 1.5875 mm)

In the simulation model, a 12.7 mm × 12.7 mm × 10 µm ITO film is on the 12.7 mm × 12.7 mm × 1 mm substrate and surrounded by 15 mm × 15 mm × 2 mm air which best simulates the real environment. ITO films can be deposited on conducting substrates or insulating substrates. The conducting substrate is WC plates, and insulating substrate is quartz glass.

Figure 6.4 shows the comparison of electric potential map for ITO films on the conducting substrate and the insulating substrate.

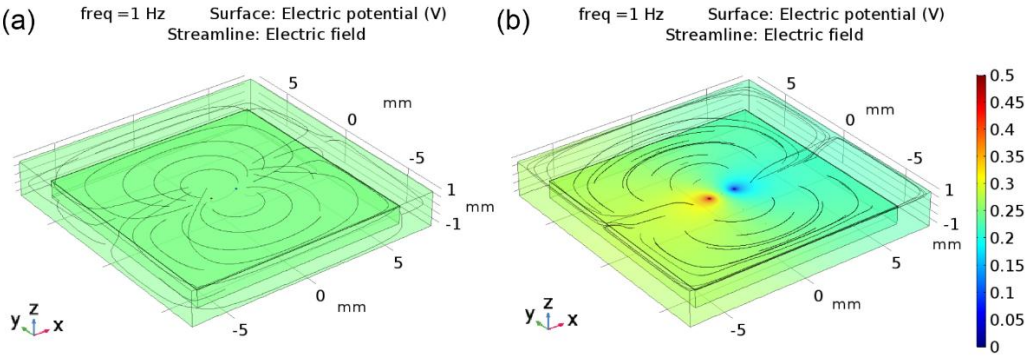

Figure 6.4. Simulated 3D electric potential map and electric field lines at 1 Hz for (a) ITO film on conducting substrate; (b) ITO film on insulating substrate. (15 mm × 15 mm × 2 mm air, 12.7 mm × 12.7 mm × 10 µm ITO film, 12.7 mm × 12.7 mm × 1 mm substrate, D = 80 µm circular electrodes with a center spacing of 1.5875 mm)

On the conducting substrate, the electric potential on the ITO film surface remains a constant at low values except for the electrodes area. Conversely, the electric potential has much bigger variance on the surface for an ITO film deposited on an insulating substrate. The conducting mechanism is different for these two in-plane measurement configurations. This can be easily noticed in the 2D current density map as shown in Figure 6.5. When measuring an ITO film on a conducting substrate, only the ITO region under electrodes has a high current density. The current passes through the ITO film and the WC substrate has a major contribution to the current path (Figure 6.5(a, c)). As a comparison, the main current path for an ITO film on an insulating substrate remains in the ITO film between two electrodes (Figure 6.5(b, d)). The current density spreads out from the electrodes and flows in the plane parallel to the substrate. Thus the current density is very low in the glass substrate.

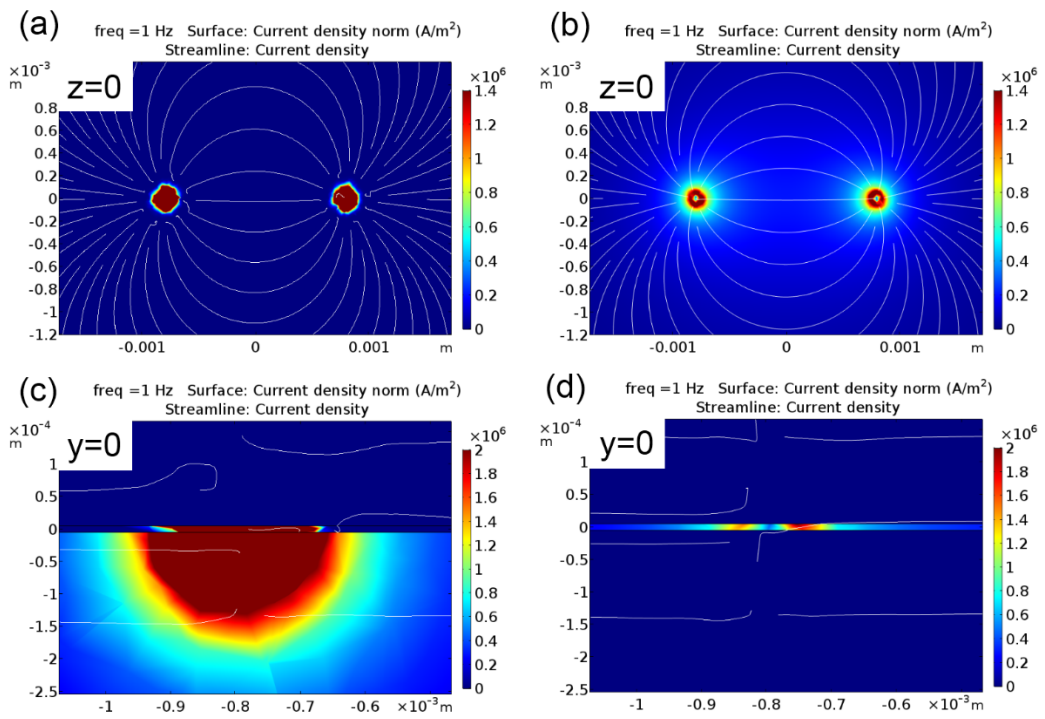

Figure 6.5. 2D simulated surface current density map at z=0 for ITO film (a) on conducting substrate and (b) on insulating substrate; 2D simulated surface current density map at y=0 near one electrode for ITO film (c) on conducting substrate and (d) on insulating substrate. (15 mm × 15 mm × 2 mm air, 12.7 mm × 12.7 mm × 10 µm ITO film, 12.7 mm × 12.7 mm × 1 mm substrate, D = 80 µm circular electrodes with a center spacing of 1.5875 mm)

The simulated impedance and capacitance values from 0.1 Hz to 10 MHz for the same 10 µm ITO film also proved that the measurement configurations can cause very big differences in the measurement results (Figure 6.6). As an example, the impedance magnitude at 1 Hz for ITO film (12.7 mm × 12.7 mm × 10 µm) can change from 5.247 × 10^{-5} Ω for parallel-plate configuration to 100.8 Ω for in-plane measurement on an insulating substrate. The real capacitance at 1 Hz can vary from 5.712 × 10^{-10} F (parallel-plate) to about 10^{-15} F (in-plane). This can also be used to verify the accuracy of our FEA model.

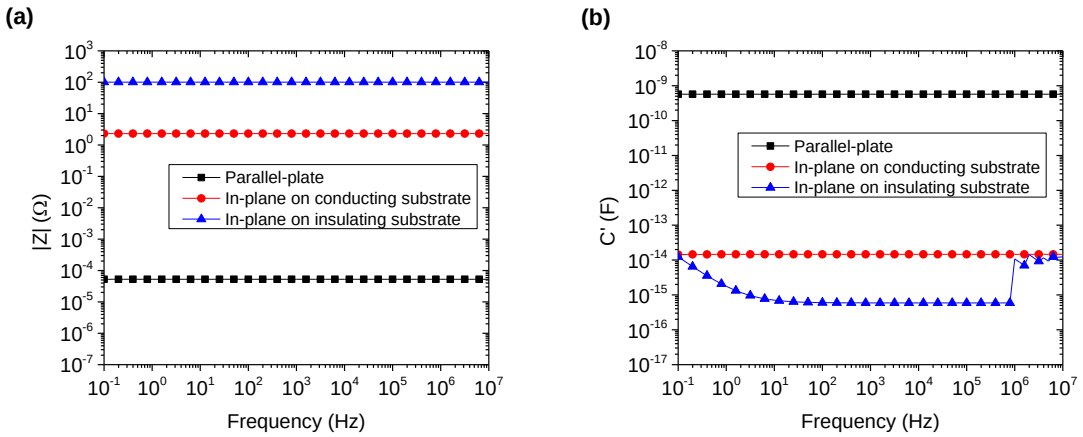

Figure 6.6. (a) Bode plots of impedance magnitude (|Z|) for same ITO film with three measurement configuration; (b) Bode plots of real capacitance (C') for same ITO film with three measurement configuration.

According to the resistance and parallel-plate capacitance Equations 6.4 and 6.5:

$$\mathrm{R} = \frac{\rho L}{A} = \frac{t}{\sigma a^2} = \frac{10\times10^{-6}}{1180\times(12.7\times10^{-3})^2} = 5.254\ \times 10^{-5}\ \Omega \tag{6.4}$$

$$\mathrm{C} = \frac{\varepsilon_r \varepsilon_0 A}{d} = \frac{\varepsilon_r \varepsilon_0 a^2}{t} = \frac{4\times8.854\times10^{-12}\times(12.7\times10^{-3})^2}{10\times10^{-6}} = 5.712\ \times 10^{-10} F \tag{6.5}$$

Where t is the thickness, σ is the conductivity and a is lateral length of a square ITO film. The theoretical values for resistance and capacitance are almost equal to the simulation results in the parallel-plate configuration case. This proves that our simulation setup, mesh process and solution are correct and that the simulation models are reasonable.

From the simulation results, it is noticed that the parallel-plate configuration and in-plane configuration on a conducting substrate give a relatively low impedance measurement. Considering the existence of cable resistance and contact resistance, it is very difficult to accurately extract the real ITO film electrical response from experimental measurement. Also, with very low impedance, the imaginary part of the circuit will be dominated by cable inductance which cannot show the capacitance behavior. Thus, the in-plane measurement

on insulating substrate, which has a relatively large impedance number and benefits capacitance measurement, is further analyzed in this chapter.

6.3.2 Comparison of different simulation models

Several different simulation models were used to study the electrical response of ITO films under in-plane measurement. For pure ITO films without substrate and air environment, both 2D and 3D models can provide reasonable simulations. The 2D top view model is a simple and effective way to obtain the impedance and capacitance of pure ITO films. Figure 6.7 shows that under the same geometry of ITO film, the 2D model and the 3D model generate similar electric potential map and electric field lines. Also, the wide frequency impedance and capacitance values are the same for these two models. However, the 2D model saves a lot of time in the simulation process. By inputting thickness with out-of-plane thickness, the number of degrees of freedom can be reduced from 10^7 to 10^5 for the 3D to 2D model. The only problem is that the substrate and environmental effect cannot be simulated in the 2D model.

To understand the substrate and environmental effects during the in-plane measurement, 3D models have to be used. In the real situation, ITO films can be as large as 25.4 mm × 25.4 mm, but films only have a thickness of 100 nm. The high aspect ratio of 2.54×10^5 make the normal meshing and simulation process very difficult and beyond our current calculation ability. In this work, one approach to overcome the problem is to apply an electric shielding boundary condition to replace the ITO layer. The thickness of the ITO layer is usually much thinner than the quartz glass substrate and air environment (1 mm). Also, the ITO layer is much more conductive than quartz glass and air. Using a 10 μm ITO

film as an example, the simulation results comparison in Figure 6.8 proves that a simplified 3D model generates similar electric potential and electric field map to the full 3D model.

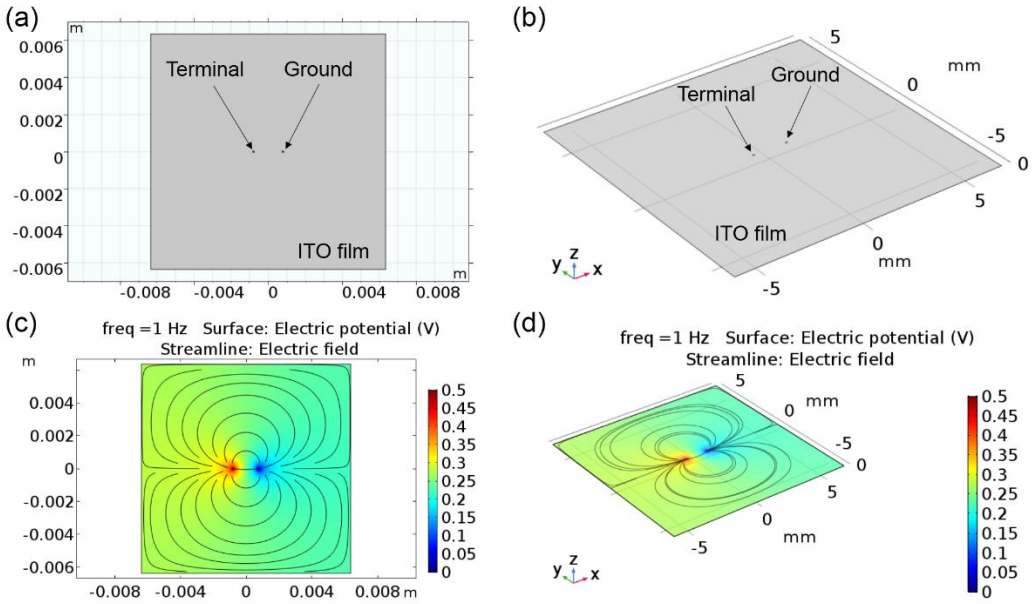

Figure 6.7. Model geometry for pure ITO film in-plane measurement: (a) 2D model and (b) 3D model. Simulated electric potential map and electric field lines at 1 Hz for (c) 2D model and (d) 3D model. (12.7 mm × 12.7 mm × 10 µm ITO film, D = 80 µm circular electrodes with a center spacing of 1.5875 mm)

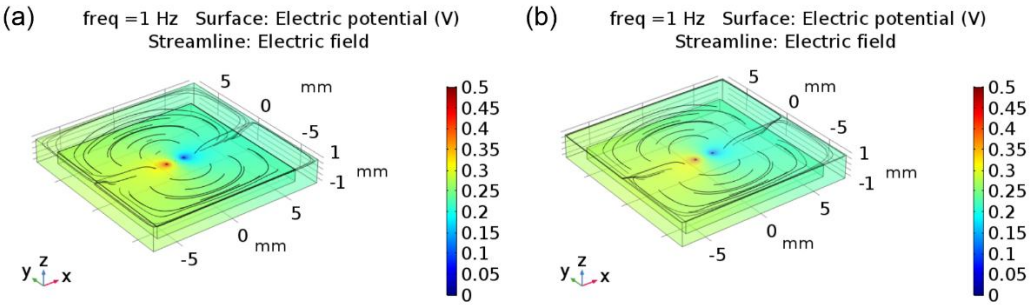

Figure 6.8. Simulated 3D electric potential map and electric field lines at 1 Hz for (a) 3D full-fidelity model with 12.7 mm × 12.7 mm × 10 µm ITO film; (b) 3D simplified model using ITO film as electric shielding boundary conditions. (15 mm × 15 mm × 2 mm air, 12.7 mm × 12.7 mm × 1 mm substrate, D = 80 µm circular electrodes with a center spacing of 1.5875 mm)

The impedance and capacitance within a wide frequency range can be obtained by post-processing as shown in Figure 6.9. The simplified 3D ITO model gives impedance values

(100.00 Ω) close to full 3D ITO models (100.78 Ω) with an error less than 1% from 0.1 Hz to 10 MHz frequency. The Bode plots of real capacitance for two models have similar shapes, but the values have some difference at mid-frequency region. The low frequency real capacitance (0.1 Hz) for the two models are both around 1.25×10^{-14} F. The later simulation results prove that this large capacitance is mainly coming from the substrate and air environment.

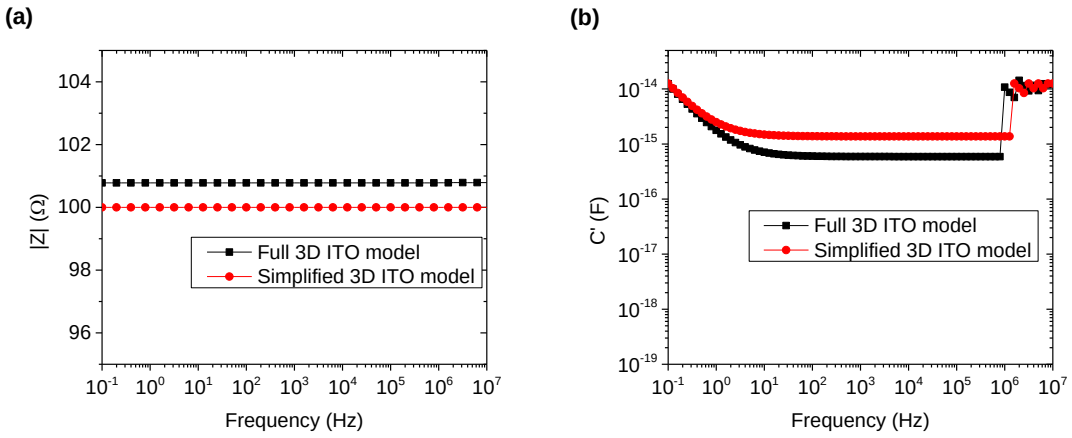

Figure 6.9. (a) Bode plots of |Z| for 10 µm ITO film with two different 3D models; (b) Bode plots of C' for same 10 µm ITO film with two different 3D models. (15 mm × 15 mm × 2 mm air, 12.7 mm × 12.7 mm × 10 µm ITO film, 12.7 mm × 12.7 mm × 1 mm substrate, D = 80 µm circular electrodes with a center spacing of 1.5875 mm)

6.3.3 Effect of substrate and air environment

As insulating materials, the quartz glass substrate and air environment should have higher impedance than the ITO films. Here a 2D model similar to Figure 6.7(a) was used to simulate electrical response from pure ITO film (12.7 mm × 12.7 mm with thickness of 100 nm), pure quartz glass substrate (12.7 mm × 12.7 mm with thickness of 1 mm) and air block (15 mm × 15 mm × 2 mm). Simplified 3D models using 100 nm ITO film as electric shielding boundary were applied to simulate the impedance and capacitance for the combination of ITO film with quartz substrate, combination of ITO film with air,

combination of ITO with both substrate and air. In this way, electric property for each material can be separated when it is impossible to do in the real experiments.

Figure 6.10 shows the simulated impedance and capacitance results for ITO film, quartz glass substrates, air environment and their combinations. The quartz and air are very insulating and their impedances decrease with increasing frequency. This matches the experimental data in the open circuit measurement in the Figure 5.3. The 100 nm pure ITO film and its three combinations with environments have almost the same impedance of 10^4 Ω. The imaginary impedances are always insignificantly small (approaching zero) compared to the real impedance. Thus the impedance magnitude are mostly contributed by the real impedance values. No apparent changes can be observed from 0.1 Hz to 10 MHz, which show pure resistor behaviour. The substrate and air environment have a very small effect on the impedance of ITO film as the curves overlap in Figure 6.10(a).

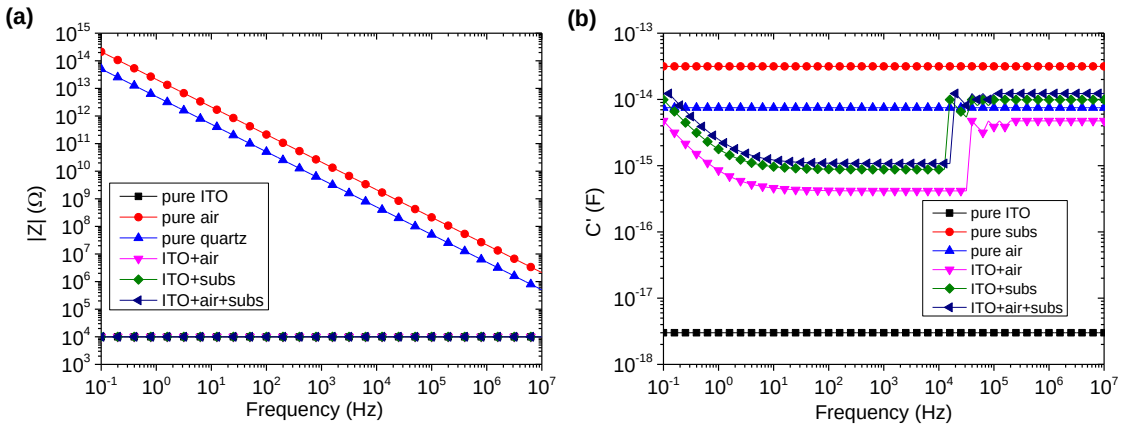

Figure 6.10. (a) Bode plots of |Z| (b) Bode plots of C' for pure ITO film, pure air block, pure quartz substrates, combination of ITO film with quartz substrate, combination of ITO film with air, combination of ITO with both substrate and air. (15 mm × 15 mm × 2 mm air, 12.7 mm × 12.7 mm × 100 nm ITO film, 12.7 mm × 12.7 mm × 1 mm substrate, D = 80 μm circular electrodes with a center spacing of 1.5875 mm)

However, the capacitance values have different trends. In the simulation, the pure substrate (3.15×10^{-14} F) and pure air (7.51×10^{-15} F) have much higher capacitance than the pure

ITO film (3.00×10^{-18} F, within the estimation of 10^{-19} F to 10^{-17} F in Chapter 5). As a result, the capacitances of combined systems are close to the substrate capacitance and air capacitance, more than 2 orders of magnitude higher than the ITO film capacitance in Figure 6.10(b) even with a transition during the middle frequency (10 to 10^4 Hz). Different air dimensions were simulated, but no apparent differences were observed. Anyway, the large capacitance of the system proves that in the in-plane capacitance measurement of conducting films on insulating substrates are dominated by the open circuit capacitance (substrate and air) as discussed in Chapter 5.

With the above impedance and capacitance values, the time constant τ can be estimated using Equation 5.6 and then the relaxation frequency f can be obtained using Equation 5.8. The time constant is about 10^{-10} s, and the relaxation frequency is about 1.29×10^9 Hz, which falls out of our frequency range. Thus during 0.1 Hz to 10 MHz frequency, all the ITO films show pure resistive behaviour in the Bode plots.

The simulated capacitance for 100 nm thick ITO film on quartz in air is still 3 orders of magnitude lower than the experimental values ($\sim 1.60 \times 10^{-11}$ F). The main reason should be attributed to the high capacitance from the probe station and the measuring instrument. With these high capacitances, the real capacitance information of ITO film were hidden and difficult to be measured in the experiments as described in Chapter 5.

6.3.4 Effect of ITO film properties

To study the effect of ITO film properties on the measured impedance and capacitance, simulations were performed using 2D models for pure ITO films and simplified 3D models for ITO films with substrate and air. Different film thickness, size and conductivity were

compared in this section when circular electrodes have a fixed diameter of 80 μm with 1.5875 mm spacing on top of measured film.

6.3.4.1 Film thickness

Figure 6.11 shows the impedance of ITO films in a wide frequency range simulated by 2D models and simplified 3D models. The impedance values of ITO films decrease with increasing film thickness as an inverse proportional relationship. This matches Equation 2.4. In addition, the impedance is independent of frequency and shows pure resistive behaviour because the relaxation frequency is much higher than what is regularly measured. Comparing the results of 2D models and 3D models, the quartz substrate and air environment has an insignificant effect on the impedance magnitude of ITO films with thickness of 100 nm to 10 μm.

The Bode plots of real capacitance for ITO films using 2D models and simplified 3D models are shown in Figure 6.12. For pure ITO films, the real capacitance is independent of frequency from 0.1 Hz to 10 MHz. The capacitance values increase in proportion to the film thickness which matches the geometric capacitance Equation 5.11 in the in-plane configuration. This proves that when calculating the capacitance for in-plane measurement, the thickness number should be in the numerator.

However, when ITO films are simulated with substrate and air environment, the capacitance curves for different film thickness have similar shapes. The high frequency platform and low frequency values for capacitance are always at 1.24×10^{-14} F. The mid-frequency platform has a capacitance about 10^{-15} F. With increasing film thickness, the sudden drop of capacitance happens at higher frequency. The reason for this transition is

still under investigation. It may be due to the large capacitance difference between the conducting film and the environment. When the ITO film is thick enough (100 μm) and has similar capacitance with the environment, the transition disappears (not shown). In the actual measurement, because the open circuit capacitance is so large (10^{-11} F), this phenomenon cannot be observed.

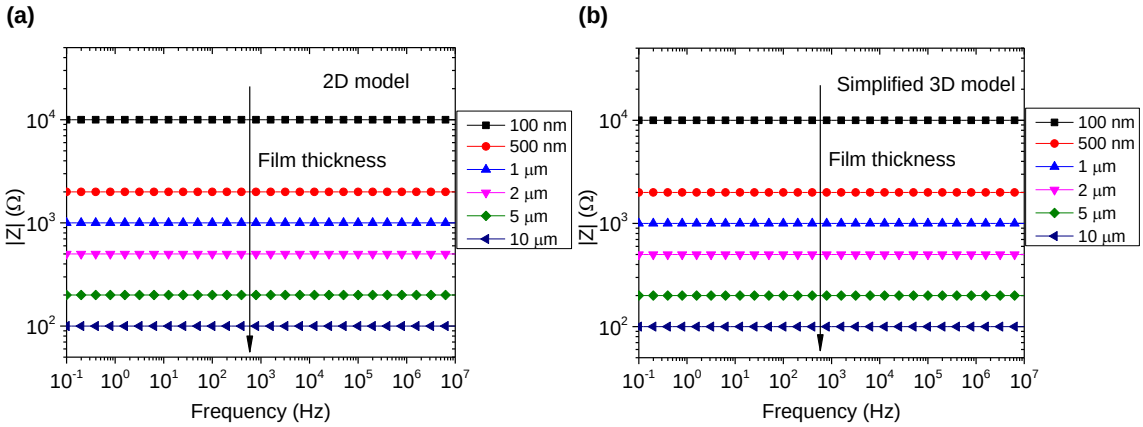

Figure 6.11. (a) Bode plots of |Z| for pure ITO films (12.7 mm × 12.7mm) simulated in 2D models; (b) Bode plots of |Z| for ITO films on quartz substrate in air environment simulated in simplified 3D models. (15 mm × 15 mm × 2 mm air, 12.7 mm × 12.7 mm × 1 mm substrate)

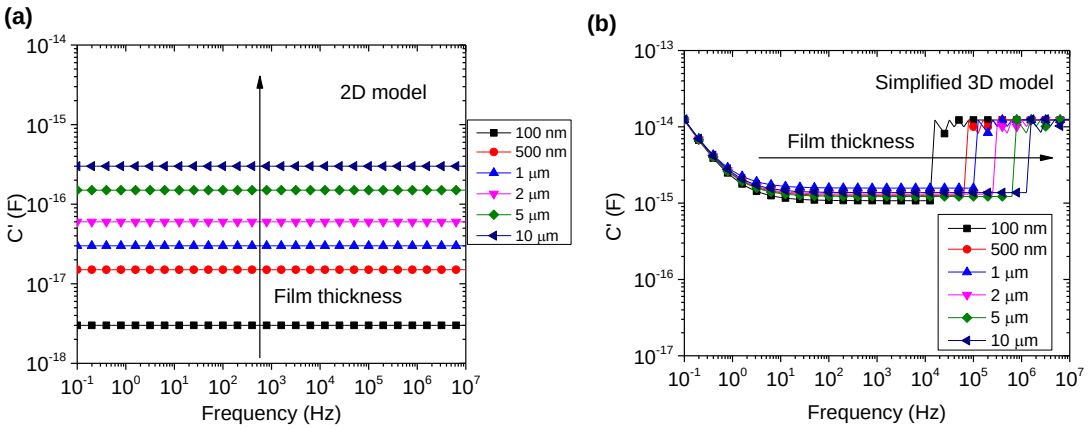

Figure 6.12. (a) Bode plots of C' for pure ITO films (12.7 mm × 12.7 mm) simulated in 2D models; (b) Bode plots of C' for ITO films on quartz substrate in air environment simulated in simplified 3D models. (15 mm × 15 mm × 2 mm air, 12.7 mm × 12.7 mm × 1 mm substrate)

6.3.4.2 Film size

Another important film property is film size (lateral length of the square film). The film thickness in this case was fixed at 100 nm. Since the ITO film impedance has almost no change over a wide frequency, a single value at low frequency is used to represent the data. The capacitance value at the same frequency is also recorded to compare the 2D models for the pure ITO film and the simplified 3D models for the ITO film with substrate in air.

Figure 6.13(a) shows the simulated impedance and capacitance for pure ITO films in 2D model. When the film size increases, the impedance of ITO film decreases from 1.31×10^4 Ω to about 10^4 Ω and then become as a constant after 12.7 mm × 12.7 mm. The reason is that when the film size is similar to the probe spacing (1.5875 mm), the non-conducting (reflecting) boundary can affect the film property as an edge effect [199]. It was reported that the outer probes to the film boundary should be at least four times the probe spacing to lower the error factor to be less than 1% [105]. The simulated capacitances are also affected by the non-conducting boundary when the film size is small. When the film size is large enough, the capacitances do not change with film size.

In the simplified 3D models for ITO films with substrate and air, the impedance shows the same trend as the pure ITO films in Figure 6.13(b). However, the simulated capacitance at 0.1 Hz is about 4 orders of magnitude higher than the capacitance of pure ITO films. This should mainly come from the capacitance of the quartz substrate and air environment.

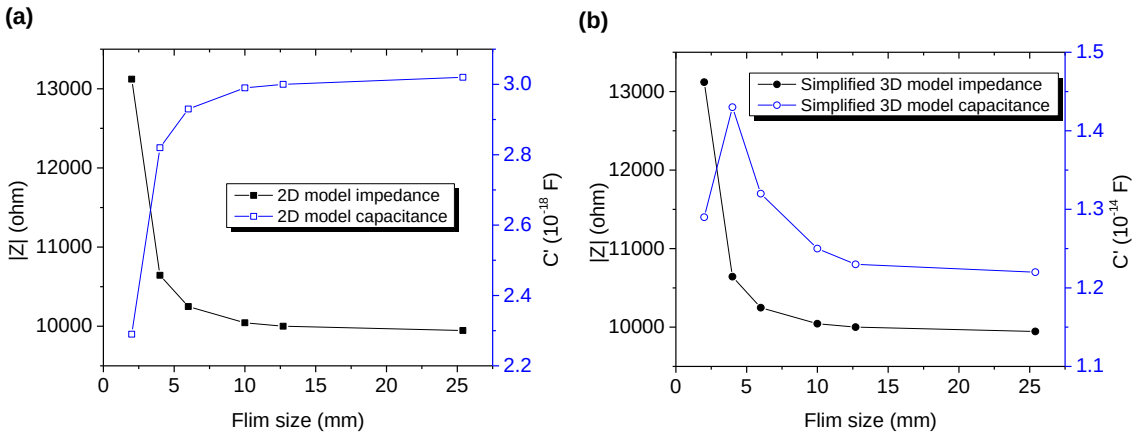

Figure 6.13. Simulated |Z| and C' at 0.1 Hz as a function of film size for two different models (a) 2D model for pure 100 nm ITO film; (b) simplified 3D models for 100 nm ITO film with substrate in air. (30 mm × 30 mm × 2 mm air) (For substrate, thickness is 1 mm but the lateral size is always the same as ITO film)

The experimental data listed in Table 6.2 matched the trend of simulation results. One layer ITO films were deposited on 12.7 mm × 12.7 mm and 25.4 mm × 25.4 mm quartz substrates with 0.5 M and 1 M ITO ink using the method described in Chapter 4. All the samples were measured by 2-probe ac impedance spectroscopy as described in Chapter 2 under 10% RH in glove box.

Table 6.2. Experimental values of |Z| and C' measured at 100 Hz for ITO films with 12.7 mm × 12.7 mm and 25.4 mm × 25.4 mm made by 0.5 M and 1 M ITO ink.

Samples (Concentration)	|Z| at 100 Hz (Ω)	C' at 100 Hz (F)
12.7 mm (0.5 M)	3.35×10^4	1.60×10^{-11}
25.4 mm (0.5 M)	3.32×10^4	1.62×10^{-11}
12.7 mm (1 M)	2.45×10^4	1.60×10^{-11}
25.4 mm (1 M)	2.40×10^4	1.65×10^{-11}

As the simulation predicted, the difference of impedance magnitudes is only about 1-2% for ITO films with two kinds of big film sizes (12.7 mm × 12.7 mm and 25.4 mm × 25.4

mm) in each ITO ink concentration. (The experimental values are different from simulation since the film conductivity is different). In addition, the measured real capacitance for all the samples has a similar value around 1.60×10^{-11} F, which is coming from the open circuit capacitance and much larger than the intrinsic ITO capacitance.

6.3.4.3 Film conductivity

In the experiments, one way to control electrical conductivity of ITO without altering thickness is to change the annealing temperature. Four high temperatures (450°C, 550°C, 650°C and 750°C) were used to anneal 100 nm ITO films on 12.7 mm × 12.7 mm quartz substrates. The electrical properties of these films were measured by the 4-probe DC sheet resistance method and 2-probe AC impedance spectroscopy. The electrical resistivities were calculated from the 4-probe DC sheet resistance method using Equation 2.4 and converted to conductivity as listed in Table 6.3. The conductivity values were put into the 2D ITO models for ITO films (D = 80 μm circular electrodes with a center spacing of 1.5875 mm). Thus the AC impedance and capacitance can be simulated.

The DC sheet resistance is also possible to be simulated from FEA. The 4-probe DC measurement has different resistance calculation formulas for bulk and thin film samples. The simulation of bulk samples has been done by Kelekanjeri and Gerhardt [200]. The simulation of thin film samples also has been done in the literature [194], which used point contact electrodes for thin films. A more realistic model with finite electrode size was performed in this work to relate the simulation to the experiments. Four circular electrodes with diameters of 80 μm and center spacing of 1.587 mm were put on the 12.7 mm × 12.7 mm ITO film as in-line 4-probe geometry in 2D model. The out-of-plane thickness is 100

nm. The voltage drop (V) between the two inner electrodes is measured when a current signal (I) is input through the two outer electrodes. A stationary study model (not shown) was used to simulate this DC electrical response. The DC resistance is calculated by Equation 2.3. Using this model, the geometric correction factor (F) can also be calculated by changing the film size.

Table 6.3. Electrical conductivity for ITO films annealed from 450°C to 750°C with AC/DC resistance ratio from experimental data and simulation results. (The AC impedance data were taken at 1 Hz frequency)

Temperature (°C)	Electrical conductivity (S/m)	Experimental AC/DC ratio	Simulated AC/DC ratio
450	5.44×10^2	1.53	1.18
550	1.40×10^3	1.55	1.18
650	3.80×10^3	1.57	1.18
750	8.30×10^3	1.67	1.18

Figure 6.14(a) shows the experimental DC resistance and AC impedance results together with the simulated results from FEA. The 2D model for the 4-probe DC method generates almost identical data with the experimental results as the data points coincide. This is reasonable since 4-probe DC method intrinsically cancels the contact resistance and probe, cable resistance with the in-line 4-probe geometry and measure the sample resistance only. Thus, the experimental results should be the same with the simulated data.

In contrast, the experimental AC impedance results are much larger than the simulated AC impedance results, as shown in Figure 6.14. Table 6.3 lists the experimental and simulated AC/DC resistance ratio. The difference in the ratio may come from cable and probe resistance. Considering the small number of these resistances (<10 Ω), they cannot explain

the large difference between the experimental and simulated AC impedance values. The contact resistance should be the main contribution to this. As reported in a recent article [201], the contact resistance for a two-electrode ac measurement can be as large as 2×10^4 Ω per contact for an In_2O_3 film (R ~ 2×10^4 Ω at 100 Hz) on Yttrium stabilized ZrO_2 substrate. When the ITO films have higher conductivity and low resistance, the contact resistance will be a bigger portion in the measurement results, which matches the increasing experimental AC/DC resistance ratio observed.

Figure 6.14(b) shows the comparison of experimental and simulated AC capacitance for ITO films with different conductivities. The experimental AC capacitance numbers are 6 orders of magnitude higher because of all the open circuit capacitance. Importantly, the simulated and experimental AC capacitances for ITO films do not change with different film electrical conductivity.

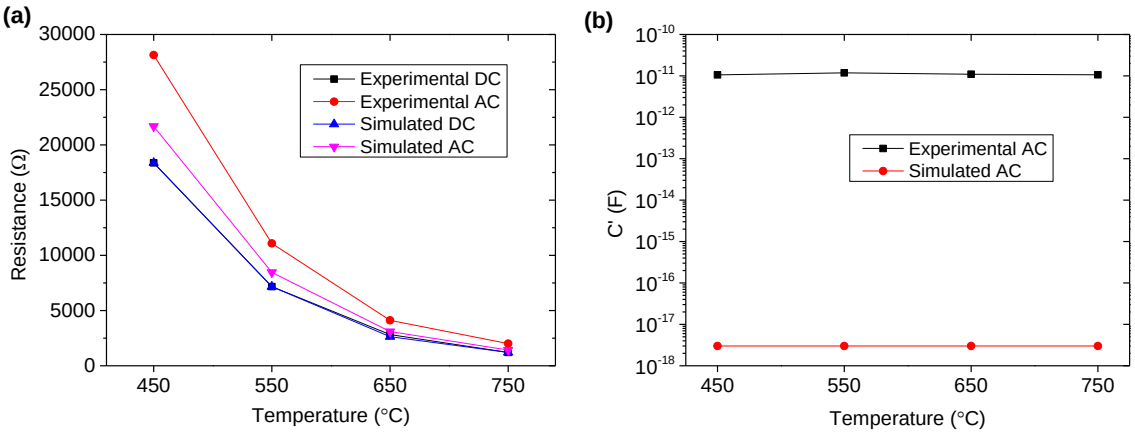

Figure 6.14. (a) Comparison of experimental DC resistance and AC impedance with simulated AC and DC results using 2D models. (b) Comparison of experimental AC capacitance with simulated AC capacitance using 2D models.

Another important fact from Table 6.3 is that the simulated AC/DC resistance ratio is not 1 even when there is no cable, probe and contact resistance in the models. Thus it is not

correct to directly use low frequency AC impedance to represent the DC resistance of ITO films for the in-plane measurement configuration. It is found that this ratio is largely dependent on the geometry of the electrodes which is discussed in the next section.

6.3.5 Effect of electrodes geometry

6.3.5.1 Comparison of circular electrodes and linear electrodes

One of the methods proposed in Chapter 5 was to deposit long linear electrodes on the top surface of the ITO films to measure capacitance. This can be simulated by FEA in a 2D model, as shown in Figure 6.15(a). The simulated electric potential map for the linear electrodes measurement is very different to the one with the circular electrodes described in Figure 6.7(c). The electric field is perpendicular to the linear electrodes (Figure 6.15(b)) instead of forming waves in the circular electrodes situation.

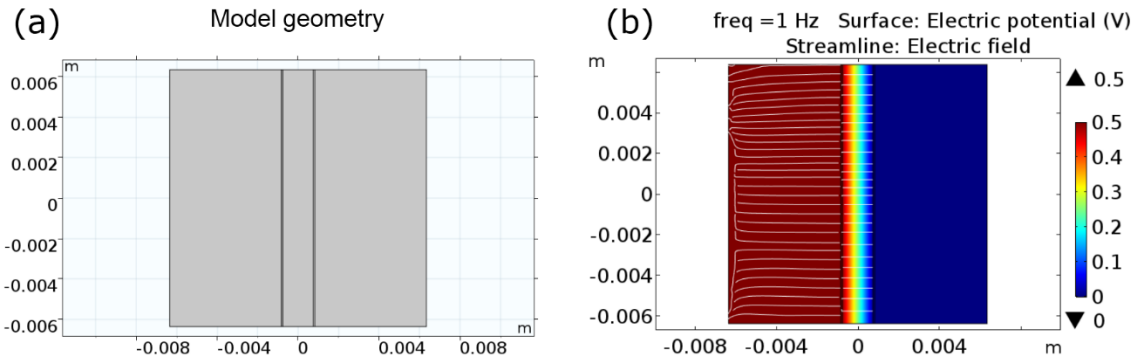

Figure 6.15. (a) Model geometry for two linear electrodes on pure ITO film in 2D model; (b) Simulated electric potential map and field lines for this model. (12.7 mm × 12.7 mm × 100 nm ITO film, 80 µm × 12.7 mm linear electrodes with spacing of 1.5875 mm in center)

Figure 6.16 shows that using the linear electrodes method can lower the measured impedance to 1.01×10^{3} Ω and increase the capacitance values to 2.98×10^{-17} F compared

to the circular electrodes method. These values prove that the linear electrodes configuration is closer to a parallel-plate measurement. According to Equation 6.4 and 6.5:

$$\mathrm{R} = \frac{\rho L}{A} = \frac{s}{\sigma t a} = \frac{1.5875\times10^{-3} - 80\times10^{-6}}{1180\times100\times10^{-9}\times12.7\times10^{-3}} = 1.01\ \times 10^{3}\ \Omega \tag{6.6}$$

$$\mathrm{C} = \frac{\varepsilon_r \varepsilon_0 A}{d} = \frac{\varepsilon_r \varepsilon_0 t a}{s} = \frac{4\times8.854\times10^{-12}\times100\times10^{-9}\times12.7\times10^{-3}}{1.5875\times10^{-3} - 80\times10^{-6}} = 2.98\ \times 10^{-17} F \tag{6.7}$$

Where s is the spacing between two linear electrodes, t is the film thickness, a is lateral length of a square ITO film.

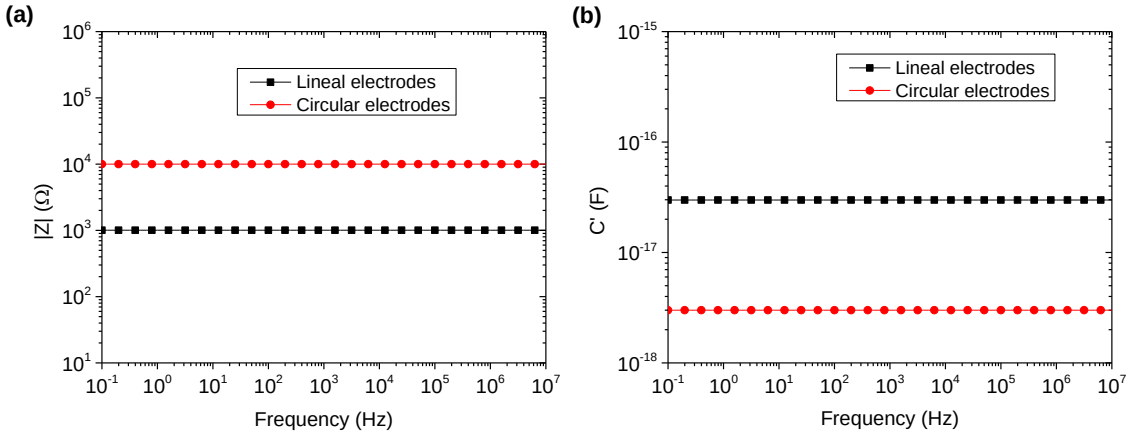

Figure 6.16. (a) Bode plots of |Z| and (b) Bode plots of C' for 12.7 mm × 12.7 mm × 100 nm ITO film with two different kinds of electrodes from 2D FEA simulation. Circular electrodes: D = 80 µm with a center spacing of 1.5875 mm. (geometry in Figure 6.7). Linear electrodes: 80 µm × 12.7 mm with center spacing of 1.5875 mm.

The theoretical impedance and capacitance of parallel-plate configuration matched simulation results from linear electrode configuration. This means that one can treat the ITO areas under electrodes as shorted [202]. The inner boundary of the electrodes to the bottom of ITO film are the real electrode plates. The ITO film in between give the measured impedance and capacitance as demonstrated in the simulation. In other words, the measured capacitance can be controlled by changing the electrodes spacing. However,

since the resistance also depends on the electrodes spacing, if one makes the capacitance as large as 10^{-11} F by making small spacing electrodes, the resistance also decreases to 10^{-3} Ω. Considering the normal cable resistance and their inductance, the real experimental measurement cannot give this accurate data. The capacitance will be also difficult to show since the inductance will dominate the impedance spectroscopy.

6.3.5.2 Effect of electrode size

As mentioned previously, it was found that the electrode size has a strong effect on the AC/DC resistance ratio from the simulation. In this section, the 2D model was used to simulate ITO film with different electrode size using the model geometry similar to Figure 6.7(a). The ITO film has a fixed size of 12.7 mm × 12.7 mm × 100 nm and electrodes center spacing is fixed at 1.5875 mm. The radius of the circular electrodes is changed from 0.1 μm to 100 μm. When the AC model has two electrodes, the DC model has four electrodes as in-line geometry. All the simulated AC and DC results are summarized in Table 6.4.

Table 6.4. Simulated AC impedance and capacitance results (at 1 Hz) compared with simulated DC resistance result from 2D model for 12.7 mm × 12.7 mm × 100 nm pure ITO film and circular electrodes center spacing is fixed at 1.5875 mm.

Electrode radius (μm)	Simulated ac impedance (Ω)	Simulated ac capacitance (F)	Simulated dc resistance (Ω)	Simulated ac/dc ratio
0.1	2.61×10^{4}	1.15×10^{-18}	8.47×10^{3}	3.09
1	2.00×10^{4}	1.50×10^{-18}	8.47×10^{3}	2.36
10	1.37×10^{4}	2.18×10^{-18}	8.47×10^{3}	1.62
40	1.00×10^{4}	3.00×10^{-18}	8.48×10^{3}	1.18
100	7.52×10^{3}	3.99×10^{-18}	8.48×10^{3}	0.89

From Table 6.4, it is proven that the simulated DC resistance stays constant when the electrode radius changes. The main reason is that electrode radius simulated are still

considerably smaller than the electrode spacing and no additional geometrical correction factor is required [105]. However, the simulated AC impedance decreases with increasing electrode radius, which causes the change of simulated AC/DC resistance ratio. In addition, when the electrode radius increases 1000 times from 0.1 μm to 100 μm, the simulated capacitance changes about 3.47 times. The ratio is much smaller than the parallel-plate configuration (1000 times). The in-plane measurement using circular electrodes cannot be simply treated as a parallel-plate configuration. Thus for in-plane configuration AC impedance spectroscopy, the electrode size can both affect the impedance and capacitance results.

6.3.6 Simulation of multi-layer ITO films

3D full models were used to simulate the electrical response for multi-layer ITO films in Chapter 4. To simplify the simulation and obtain the pure ITO film properties, the substrate and air environment were not included. The film dimensions are 25.4 mm × 25.4 mm. From the experimental DC resistance measurement, the measured electrical conductivities for one-layer (1L) ITO film and two-layer (2L) ITO film are 1118.14 S/m and 2092.63 S/m, respectively. The 2L ITO film has two separated layers of 67.4 nm (top layer) and 68.2 nm (bottom layer) with different NSLD measured by NR (from Figure 4.8). These two separated ITO layers should have different electrical conductivity and give an average conductivity of 2092.63 S/m as was measured. Assuming the top layer ITO has the same electrical conductivity as the 1L ITO film and two layers are connected in parallel as in Equation 5.11, the average conductivity ($\bar{\sigma}$) can then be calculated from Equation 6.8:

$$\bar{\sigma} = \frac{t_1\sigma_1 + t_2\sigma_2}{t_1 + t_2} \tag{6.8}$$

Where t_1 and σ_1 are thickness and conductivity for top layer, t_2 and σ_2 are thickness and conductivity for the bottom layer. The conductivity for the bottom layer ITO can be calculated as 3056.11 S/m. Then, one homogeneous ITO layer (135.6 nm) with average conductivity is compared with two separated ITO layers (top: 67.4 nm and 1118.14S/m; bottom: 68.2 nm and 3056.11 S/m) in the FEA 3D models.

Figure 6.17 (a, b) shows that one homogeneous ITO layer (135.6 nm) with average conductivity has similar electric potential map and electric field lines to the two separated ITO layers. One difference is that the electric field lines on the top surface of the two separated ITO layers are not fully connected, which means there is a weaker electric field. The 2D surface current density map at y=0 near one electrode end (cross section through center of electrodes) further proves this. With one homogenous ITO layer, the current density is highest near the end of the electrodes and current mainly flows between two electrodes in the ITO film (Figure 6.17(c)). In comparison, the two separated ITO layers show higher current density in the bottom layer (σ_2: 3056.11 S/m) than in the top layer (σ_1: 1118.14 S/m) where the potential drop in the thickness direction is negligible [202].

Figure 6.18 compares the simulated impedance and capacitance for one homogeneous ITO layer and two separated ITO layers in a wide frequency range. When the impedance values for the two models have a small difference (3.16%), the capacitance value of the two separated ITO layers is almost two times the value for one homogeneous ITO layer. The capacitance is closer to the sum of the top and bottom ITO layer capacitances which proves that Equation 5.16 is correct and films are connected in parallel. However, even when the capacitances for multi-layer ITO films are added up for each single layer, the values are

still much smaller than the open circuit capacitance. It is still a challenge to measure the intrinsic capacitance for ITO films in the real experiments.

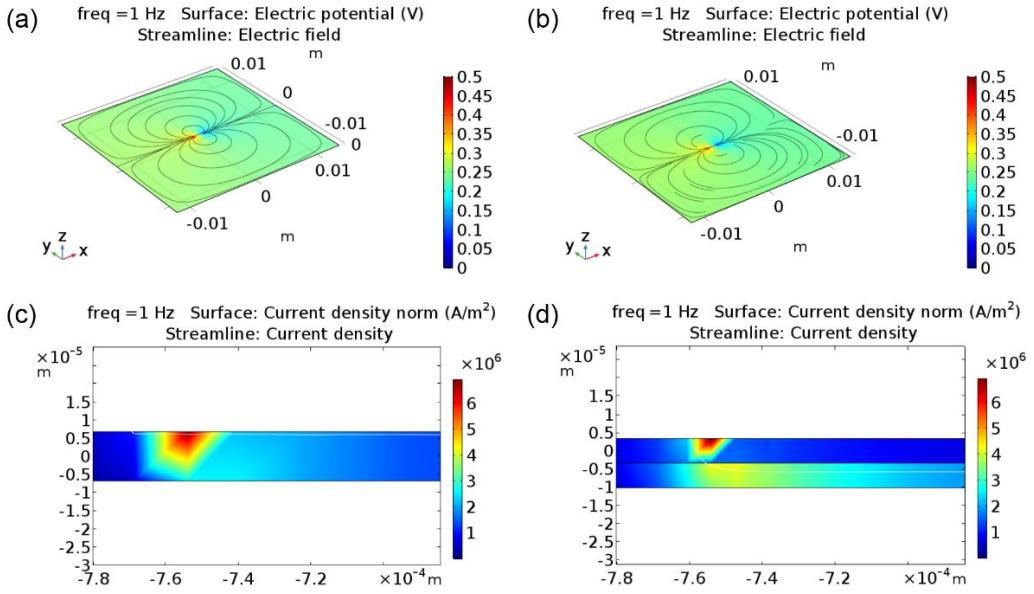

Figure 6.17. Simulated 3D electric potential map and electric field lines at 1 Hz for (a) one homogeneous ITO layer (135.6 nm) with average conductivity of 2092.63 S/m; (b) two separated ITO layers (top: 67.4 nm and 1118.14 S/m; bottom: 68.2 nm and 3056.11 S/m). 2D simulated surface current density map at y=0 near one electrode for (c) one homogeneous ITO layer; (d) two separated ITO layers. The film size is 25.4 mm × 25.4 mm (*The thicknesses are enlarged 100 × during simulation). Circular electrodes: D = 80 μm with a center spacing of 1.5875 mm.

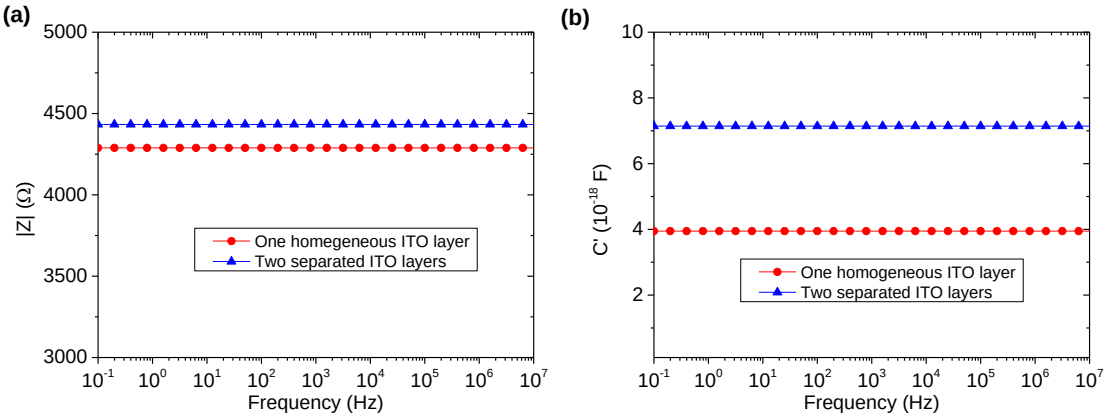

Figure 6.18. (a) Bode plots of |Z| and (b) Bode plots of C' for one homogeneous ITO layer (135.6 nm) with average conductivity of 2092.63 S/m and two separated ITO layers (top: 67.4 nm and 1118.14 S/m; bottom: 68.2 nm and 3056.11 S/m). The film size is 25.4 mm × 25.4 mm. Circular electrodes: D = 80 μm with a center spacing of 1.5875 mm.

6.4 Conclusion

FEA was used to simulate the electrical response of ITO films with 2D and 3D models and relate to the experimental results. Three different AC impedance spectroscopy measurement configurations were compared in the simulation to show that in-plane measurement on an insulating substrate is the most suitable method to study ITO films. The insulating substrate and air environment has an apparent effect on the measured capacitance but almost no influence on the measured impedance for the ITO films. When the normal experimental in-plane AC capacitance for ITO films are dominated by the open circuit capacitance, the FEA simulation makes it possible to estimate the intrinsic ITO capacitance values.

The effects of ITO film geometry and conductivity were discussed and compared to the experimental results. The simulated DC measurements results matched well with the experimental data. However, the simulated AC results are much smaller than the experimental AC data. It was concluded that a large contact resistance existed in the AC 2-probe measurements between the electrodes and the ITO film. Also, it was found that the AC measurement is affected by the electrode geometry (shape and size).

Last, an example of multi-layer ITO film was simulated with one homogenous layer and two separated ITO layers using the experimental data described in Chapter 4, which provided evidence that different ITO layers are connected in a parallel way.

CHAPTER 7. APPLICATIONS OF SOLUTION-PROCESSED ITO FILMS

The characterization in previous chapters proved that solution-processed ITO films have a good combination of smooth surface morphology, high optical transmittance and low sheet resistance. To demonstrate the applicability of these ITO films, several different electronic devices were fabricated using multi-layer ITO films such as a LCD pixel device, a humidity sensor and ITO transparent electrodes.

7.1 ITO used in a LCD

According to a recent research report [203], the display market was valued at $106.41 billion in 2015 and is expected to grow to $169.1 billion at a 7.5% annual growth rate from 2016 to 2022. As one of the main component of displays, the need for TCO thin films also increases. As mentioned in Chapter 1, ITO is the dominant TCO material in these display technologies that include liquid crystal displays (LCDs) [204], organic light emission diodes (OLEDs) [205] and transparent displays [206]. LCD is the most commonly used display in the current market. Most cell phones, tablets and monitors currently use LCD techniques. OLED and other multi-functional transparent displays are newly emerging applications that require flexibility and see-through functions.

The LCD is a display technique that uses liquid crystals to control the light direction. In each pixel, the ITO thin films in the LCD are used as electrodes to sandwich the liquid crystals in between. By changing the applied voltages on the ITO, the electrical field between two ITO layers can modulate the arrangements of the liquid crystal molecules and

thus switch the display on or off. The traditional methods of ITO deposition in LCDs require vacuum-based methods and etching steps to fabricate designed ITO patterns, which require more steps and waste a lot of ITO in the process.

Here we report an all solution-processed method to fabricate LCD pixel devices with ink-jet printing method. The ink-jet printing method not only simplifies the fabrication of the ITO films but also directly print ITO patterns without waste. This may greatly lower the cost of LCD devices.

7.1.1 Fabrication of all solution-processed LCD device

The structure of an all-printed LCD pixel device is shown in Figure 7.1. All the ITO films and ITO patterns were made by the ink-jet printing method discussed in Chapter 3. For assembly of the LCD pixel devices, 5 wt% polyvinyl alcohol (PVA) water solution was prepared with heating and mixing. PVA layers were deposited onto ITO-coated glass with a spin coater and heated up to 100^{o}C to remove any water residue. The surface of the PVA layers was rubbed with cotton cloth in one direction [207]. ITO films were exposed by wiping one edge of the PVA layers with a damp tissue. Then two pieces of PVA coated ITO films were assembled together by binder clips after putting one drop of twisted nematic liquid crystal 4'-pentyl-4-biphenylcarbonitrile on the PVA layer. The PVA layers here worked as alignment layers to control the orientation of liquid crystal molecules under no voltage conditions. Next, polarizer films were added to the outside of the glass substrates making sure that one side was aligned perpendicular to the orientation of the first. Finally, the properties of the LCD pixel device was tested by UV-visible spectroscopy when connecting to a Keithley voltage source.

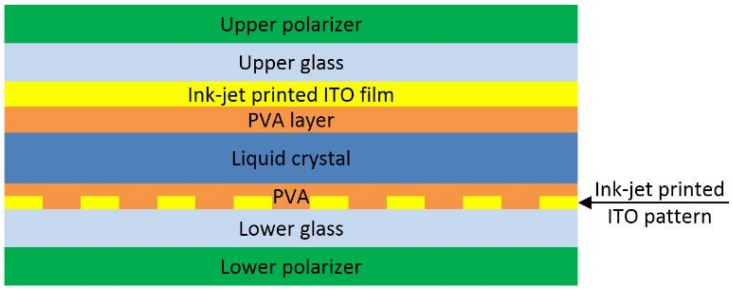

Figure 7.1. The structure of our all-printed LCD pixel.

7.1.2 Results and discussion

To test the ink-jet printed ITO films, simple LCD devices were assembled as shown in Figure 7.2. A small "GT" pattern was ink-jet printed on the glass substrate with ITO ink. The printing and annealing steps were exactly the same as with the previously described ink-jet printed samples on glass substrates. One 5L ink-jet printed ITO film and one 5L "GT" ITO pattern were put together for the LCD device. As we know, photolithography and etching processes are required for commercial ITO patterning, while they are not needed for all-printed LCD devices. Even with two polarized films in orthogonal optical directions, the small LCD devices were translucent (Figure 7.2(a)) with no applied voltage. The reason is that twisted nematic liquid crystal layers can rotate the field by 90^{o} between the two ITO films. In this way, polarized light can still go through the whole device. After applying a DC voltage to the ITO films, a clear "GT" pattern appeared on the device as shown in Figure 7.2(b). The DC voltage affects the orientation of the liquid crystals, making them parallel to the electric field. Thus, the liquid crystal cannot rotate the field and the light cannot pass through the ITO regions.

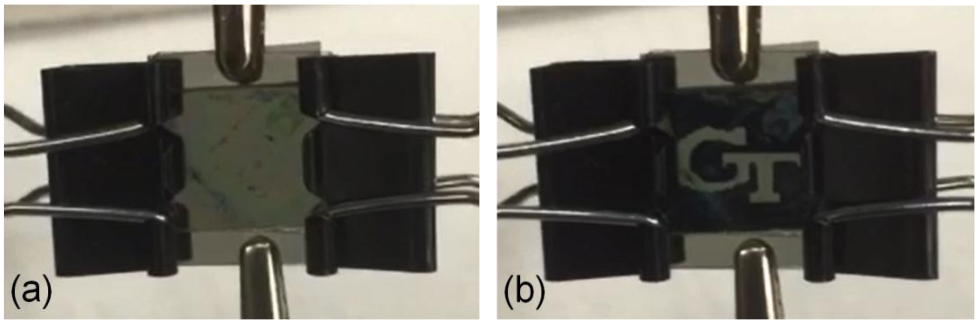

Figure 7.2. Visual images of an all-printed LCD device before (a) and after (b) connecting to a voltage source.

The voltage response properties of the all-printed LCD device was measured in a UV-vis spectrophotometer at room temperature when the device was connected to a controllable DC voltage source. Two commercial sputtered ITO glass slides were used to fabricate an LCD device with similar steps. These devices had no patterns. %Transmittance - Voltage (%T-V) curves of these two devices were recorded at $\lambda = 550$ nm, as shown in Figure 7.3.

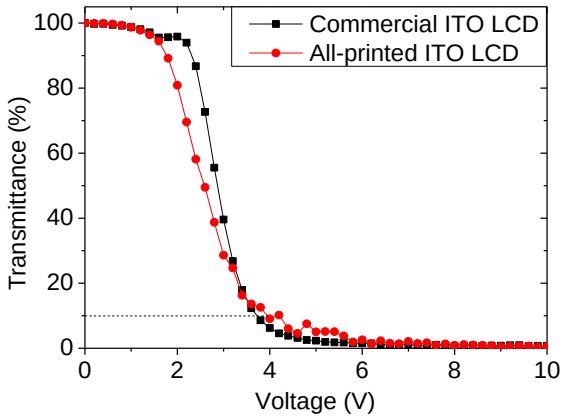

Figure 7.3. %Transmittance vs voltage curves of commercial ITO LCD and ink-jet printed ITO LCD at 550 nm wavelength.

It was found that the all-printed LCD device had a very similar driving voltage (voltage when transmittance is at 10%) compared to LCD devices made by the commercial ITO glass. It is noteworthy that the all-printed LCD devices had an earlier response to the DC

voltage in the low voltage region. However, the transmittance of the all-printed LCD device had some fluctuation between 4 and 6 V. The reason might come from the light interference between multiple layers of the ITO films.

7.2 ITO as an electrical sensor

Sensors are electronic devices which can detect and respond to the changes in the environment and send out different signals. Sensors are very common applications in everyday life, such as light sensors, humidity sensors and temperature sensors [208-210]. As an example, humidity sensors can measure the presence of water vapor in the air. The electrical property (impedance or capacitance) of humidity sensors changes when the sensing component absorbs different amounts of water. One of the methods to quantify humidity is to use relative humidity (RH), which can be expressed as shown in Equation 7.1 [211]:

$$\mathrm{RH} = \frac{P_w}{P_{ws}} \times 100\% \tag{7.1}$$

Where P_w is the actual vapour pressure of water, P_{ws} is the saturated vapour pressure of water at one temperature and pressure. Thus the relative humidity depends on the temperature and pressure. The mass of saturated water vapour in air is not trivial. At 25^{o}C and 101.325 kPa, it can be about 23.1 g in 1 m^3 air [212].

ITO is a material which has great potential in sensor electronics. Actually, the capacitive touch screen discussed before is a kind of position sensor, since the ITO-made capacitors show different capacitance with different finger-touch positions. ITO can also be used to detect a lot of gases such as CO_2, CCl_4, NO, NO_2 and other reducing gases [213-216]. Patel

et al. [215] reported E-beam evaporated ITO films with copper stimulator layer had high sensitivity to detect methanol at room temperature. Jiao et al. [216] reported that sol-gel prepared ITO thin films can detect various reducing gases with good long-term stability. These examples prove that the surface of oxide semiconductors is chemically active and able to react with gases.

In the next section, we provide evidence that solution-processed ITO films can work as humidity sensors and compare the detection sensitivity with sputtered ITO films.

7.2.1 Experiments

The 1L solution-processed ITO films were made by spin-coating method as described in Chapter 4. The comparison sample, 1L sputtered ITO film was purchased from Sigma Aldrich with a sheet resistance around 100 Ω/sq. A commercial glove box with desiccant/pump drying system was used. The actual RH inside the glove box was read by a commercial humidity sensor. To increase the RH, water was sprayed inside the chamber. To reduce the RH inside, the pump drew air out from the chamber and circulated it back to the chamber through the desiccator. Thus the pressure inside the glove box can remain the same. A 4-probe station was put inside the glove box to measure the AC impedance magnitude (|Z|) of all the ITO films at 0.1 Hz. At each RH, samples were measured three times and the average numbers were obtained. All of the tests were conducted under the same temperature of 23^{o}C.

7.2.2 Results and discussion

Figure 7.4 shows the variation of |Z| for 1L spin-coated ITO film and 1L sputtered ITO film as a function of RH conditions. One measurement was done for each RH condition. When the RH increases, the |Z| of the 1L spin-coated ITO film and 1L sputtered ITO film both decrease. Although the |Z| of sputtered ITO films was enlarged 100 times, it is apparent that the spin-coated ITO films have more significant drop in the values. The slope of the linear fit for the 1L spin-coated film is -218 Ω/sq·%, whereas the slope of the linear fit for the 1L sputtered film is -2.20 Ω/sq·%.

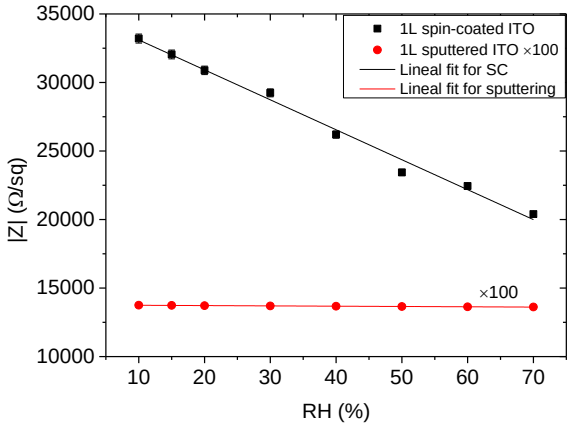

Figure 7.4. Variation of |Z| for 1L spin-coated ITO film on quartz substrate and 1L sputtered ITO film as a function of RH conditions. The dots are experimental data, lines are the linear fitting. The |Z| number for sputtered ITO film was enlarged at 100 times for better comparison.

To further compare the humidity sensor function of the spin-coated ITO film and sputtered ITO film, the sensitivity of these ITO films was determined using Equation 7.2 [215]:

$$|S| = \frac{R_0 - R_1}{R_1} \times 100\% \qquad (7.2)$$

Where R_0 is the impedance magnitude of ITO film at the measured humidity level, R_1 is the impedance magnitude of ITO film at the lowest humidity level.

The variation of sensitivity for the 1L spin-coated ITO film and the 1L sputtered ITO film as a function of RH conditions is shown in Figure 7.5. With increasing RH numbers, the sensitivity of two ITO films both increased. The solution-processed ITO film shows much higher sensitivity to the different RH than the sputtered ITO film. The sensitivity change of the 1L spin-coated ITO films is approximately linear with the increasing RH.

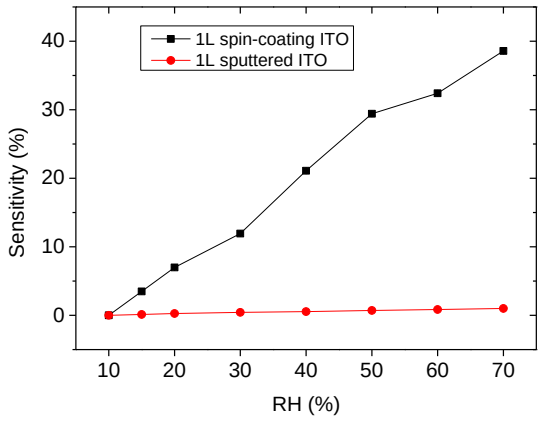

Figure 7.5. Variation of sensitivity for 1L spin-coated ITO film on quartz substrate and 1L sputtered ITO film as a function of RH conditions.

The reason is that the microstructures of solution-processed ITO films and sputtered ITO films are very different. The sputtered ITO films usually have a density approaching the theoretical ITO density and very little porosity (<10%) [217], whereas the 1L spin-coated ITO films had much lower ITO density and a large porosity of 57.3%. The surface as well as the inner microstructure of spin-coated ITO films are more porous than the sputtered ITO films. The water molecules can be physically absorbed on the ITO surface or chemically absorbed by hydrogen bonding [218]. The porous surface and microstructure

can increase the absorption of moisture in the air. Actually, pure water is a much better conductor than the air. Considering the large pores and space inside solution-processed ITO films, the water might fill in the pores and form a thin layer at the film surface, thus greatly decreasing the final |Z| at high humidity conditions.

The sensitivity change of 1L spin-coated ITO films is in approximately linear relationship with the RH, which makes it possible to work as a humidity sensor.

7.3 Transparent electrodes

The 5L ink-jet printed ITO films were tested with a blue LED light bulb. By putting the ITO films inside a LED electrical circuit to work as an electrical path, both the transparency and conductivity can be seen visually in Figure 7.6. By adding a 3V DC voltage, the LED lights up without changing any transparency of the ITO films. This proves that solution-processed ITO films can work as transparent electrodes. It is possible to use them in electronic applications requiring transparent conducting films.

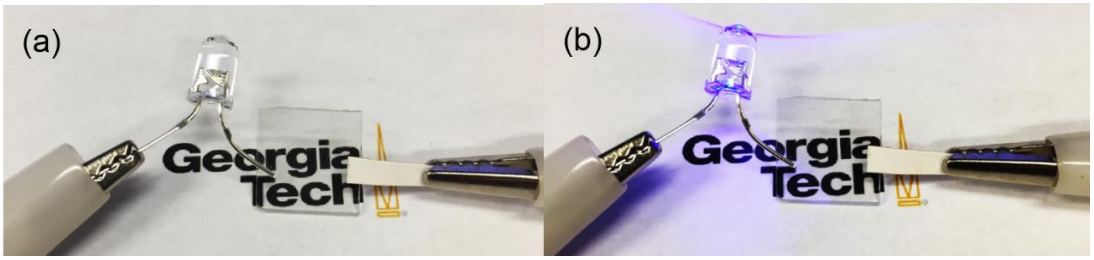

Figure 7.6. Visual images of transparent ink-jet printed ITO films on glass substrates working as transparent electrode for a blue LED light (a) without any voltage; (b) with 3V DC voltage.

7.4 Conclusion

To demonstrate the good properties of ink-jet printed ITO films, all-printed LCD devices were first fabricated and tested. The all-printed LCD device, which displayed a “GT” pattern, showed a sharp image shift when subjected to a DC voltage source. When compared to traditional LCD devices, made with sputtered ITO films, it was found that our all-printed LCD device had an earlier response to the application of a low voltage with a similar driving voltage.

Second, a prototype of a humidity sensor using one layer spin-coated ITO film was tested and discussed. The |Z| and sensitivity of 1L spin-coated ITO films were measured under RH from 10% to 70% inside a controlled glove box and compared with 1L commercial sputtered ITO films. The results showed that spin-coated ITO films have much better sensitivity to detect RH than the sputtered ITO films. The possible mechanisms for the changes under different RH were discussed.

Last, a simple demonstration of transparent electrodes using solution-processed ITO films were made with an LED light, which proves their applicability as transparent electrodes for electronic devices.

CHAPTER 8. CONCLUSIONS AND SUGGESTED FUTURE WORKS

8.1 Conclusions

This dissertation research covered the processing, characterization, modeling and applications of solution-processed ITO films, focusing on buried microstructural analysis and detailed studies of electrical properties for multi-layer ITO films.

Two solution-based processing methods were used to fabricate multi-layer ITO films with a good combination of high optical transmittance, low sheet resistance and smooth surface roughness under optimized processing conditions. The number of deposited layers can affect the film thickness, crystallinity, optical and electrical properties of ITO films. The ITO films from ink-jet printed method are more homogeneous than the spin-coated films considering the smoother cross section interphase and surface roughness number (~1 nm).

The buried microstructure of solution-processed multi-layer ITO films were characterized by neutron reflectometry in this dissertation for the first time. Detailed information about film thickness and surface roughness were obtained from fitting of the NR data and matched well with other experimental results. The microstructural porosity of the multi-layer ITO films was quantified from neutron scattering length density and found to be decreased with increasing number of deposited ITO layers. This is confirming that the ITO films became denser and less porous with the multi-layer deposition procedure. The existence of porosity also partially addresses the question that solution-processed ITO films has higher sheet resistivity than the dense vacuum-processed ITO films. The NR is believed

to be applicable to inspect microstructure of any type of multi-layer films non-destructively and not only ITO films.

The electrical properties of multi-layer solution-processed ITO films were experimentally characterized by impedance spectroscopy in a 2-probe in-plane configuration. The intra-particle and inter-particle conducting mechanisms in ITO films were discussed. It was proved that open circuit capacitance from measurement setup could have a significant impact on the IS measurements, which was further supported by the experimental results. This work demonstrates that correct measurement of impedance spectroscopy requires a well-controlled instrument setup and well-defined sample-electrode geometry to interpret the intrinsic impedance and capacitance of thin film samples. DC resistance and AC impedance of same ITO films were compared and the reasons for their differences were explained.

To further study the electrical properties, finite element analysis was used to simulate the impedance spectroscopy of solution-processed ITO films in 2D and 3D models. The FEA analysis gave an estimation of the intrinsic ITO capacitance values when it was difficult for real experiments. Insulating substrate and air environment could strongly affect the measured capacitance but had minimal effect on the measured impedance. This agreed well with the behavior of experimental open circuit capacitance. The effects of sample geometry, film conductivity and electrodes geometry were simulated. The simulation results showed a reasonable match to experimental results. A tentative multi-layer ITO film model was built and showed that different ITO layers were connected in parallel, which proved the correctness of the proposed models in this work.

Several electronic applications were fabricated using solution-processed multi-layer ITO films. All-solution processed liquid crystal devices can be assembled with ink-jet printed ITO films, showing comparable properties to the LCD device made by sputtered ITO films. A prototype of humidity sensor was built with spin-coated ITO film and had higher sensitivity to the different RH conditions than a sputtered ITO film. A simple demonstration of transparent electrodes using solution-processed ITO films was fabricated with LED light.

The best ITO films made in this work had a combination of very low surface roughness (<2 nm), high optical transmittance (> 95%) in visible light range and controllable low sheet resistivity (10^{-2} to 10^{-3} Ω·cm). These low-cost solution-processed ITO films, with sub-micrometer thickness, have great potential for most optoelectronic applications.

8.2 Suggested future work

The fabrication of solution-processed ITO films in this research were all done in the atmospheric conditions. The different relative humidity conditions were proved to affect the electrical measurements of ITO films. Also, different RH can affect the film properties during the processing. It was found that ITO ink could not wet the substrate well and formed individual droplets under high RH conditions. The possible reason is that moisture can absorb to the substrate surface and affect the wetting of the ITO ink. A comparison of film fabrication under different RH in controlled glove box may give a better fabrication conditions for solution-processed ITO films.

The most frequently used annealing process in this research was 450°C annealing on a hot plate, which is a relatively simple and convenient annealing process. However, with this

temperature, most flexible polymer substrates can melt. Other annealing process should be considered to achieve quick annealing without damage to the substrate, such as laser sintering and infrared heating. Flexible ITO films have more broad electronic applications.

Other forms of ITO particles can be considered, such as ITO nanowires and ITO/conductive polymer composites. Although these can increase the difficulty of processing, these directions may produce ITO films with better flexibility than the ones from normal round-shape ITO particles. Also, it may be possible to lower the annealing temperature when other forms of ITO particles are used that have large surface areas.

Other impedance spectroscopy instruments should be considered to measure the ac impedance of multi-layer ITO films. Different impedance instruments may give different response for the same sample because the different compensation inside the instruments. An expanded frequency range, especially high frequency range (GHz to THz) may show more information about the ITO films. Other measurement configuration can be tried for bulk ITO pellets to understand the relation between in-plane and parallel-plate measurement. Very low impedance may be obtained and it will be a challenge to remove the large inductance from cables and extract the ITO capacitance.

Computers with better calculation ability could be used to simulate multi-layer ITO films with full-fidelity 3D dimensions, which was difficult for current research. The contact resistance can be added into the model between electrodes and ITO film. The result will be closer to the experimental data. Another improvement can be done by simulating ITO nanoparticles with air pores instead of assuming homogeneous ITO layer. This may reveal the detailed conduction mechanism inside porous ITO films.

APPENDIX A. COMPARISON OF DIFFERENT ITO INKS

In this chapter, we compared three different ITO inks for making solution-processed ITO films. ITO films were all fabricated by spin coating and annealed by hot plate as described in Chapter 3 using glass substrates. The electrical resistivity, optical transmittance and surface morphology of these ITO films were characterized and compared using several different characterization tools, including confocal microscopy, SEM and AFM. The goal was to find out which ITO ink had the best combination of different properties. Many of the figures in this section appear in a previous publication [126].

A.1 Three different ITO inks

All of the ITO inks used in this chapter are shown in Figure A.1(a). The first ITO ink is nanopowder-water suspension made from commercial ITO. For this suspension, the ink cannot be directly used right after the mixing steps, since the large agglomerates in the suspension will lower the film quality. Therefore, the ink was put into a centrifuge for 30s to allow partial precipitation, as shown in Figure A.1(b). The top, middle and bottom dispersion were extracted to make separate ITO films.

The second ITO ink is made by dissolving sol-gel ITO precursors in acetylacetone to form a colloid as described in Chapter 2. For this ITO ink, the quality of each deposition for multiple layers is good, so one to five layer ITO films were made by sol-gel ITO ink.

The third ITO ink is obtained by dispersing ITO colloidal nanoparticles in hexane. For this hexane solution, it is difficult to deposit more than three layers, because the ITO films will

become very rough and cloudy on the surface after three layers. Therefore, only one, two, three layer ITO films were fabricated.

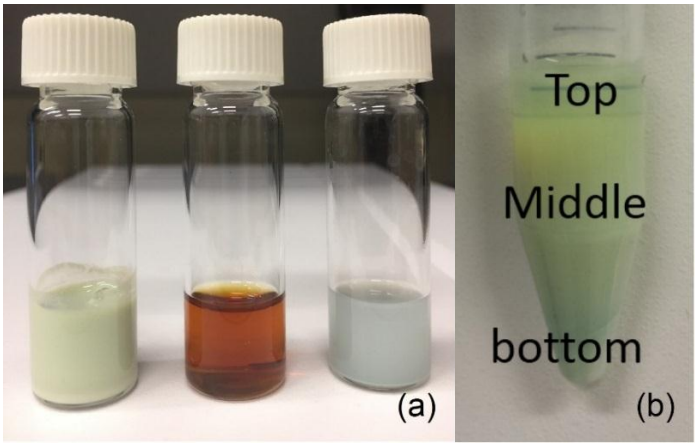

Figure A.1. (a) Image of three different ITO inks in glass vials. From left to right: commercial ITO nanopowder-water dispersion, sol-gel ITO ink, ITO colloidal nanoparticle hexane dispersion. (b) The partial precipitation of a commercial ITO nanopowder-water dispersion.

A.2 Characterization results and discussion

A.2.1 Optical and electrical properties

All of the ITO films were highly transparent after annealing except for the bottom dispersion ITO films (made from commercial ITO nanopowder ink), which showed a light yellow color. The high transparency was proved by the transmittance characterization using a UV-vis spectrophotometer shown in Figure A.2. Since the commercial ITO nanoparticles don't have surface modification, the ink will gradually form stratification layers. Different parts of the dispersion can produce ITO films with very different properties. In Figure A.2(a), the top dispersion ITO films had a transmittance as high as 99.36%, whereas the bottom dispersion ones had only 67.56% at 550 nm wavelength. This is the reason that bottom dispersion ITO films are yellow in color. For the synthesized ITO

colloidal nanoparticle dispersion, all the ITO films had a transparency higher than 90% (Figure A.2(b)). The sol-gel ITO ink can also produce highly transparent ITO films with multiple layers. The transmittance for five layer ITO films was 92.66% at 550 nm. The only difference from other UV-vis spectroscopy results is that the sol-gel ITO films had wave-like features, while others did not. The possible reason might be the light interference between the upper and lower surfaces in each layer of thin films and the porous structure inside films.

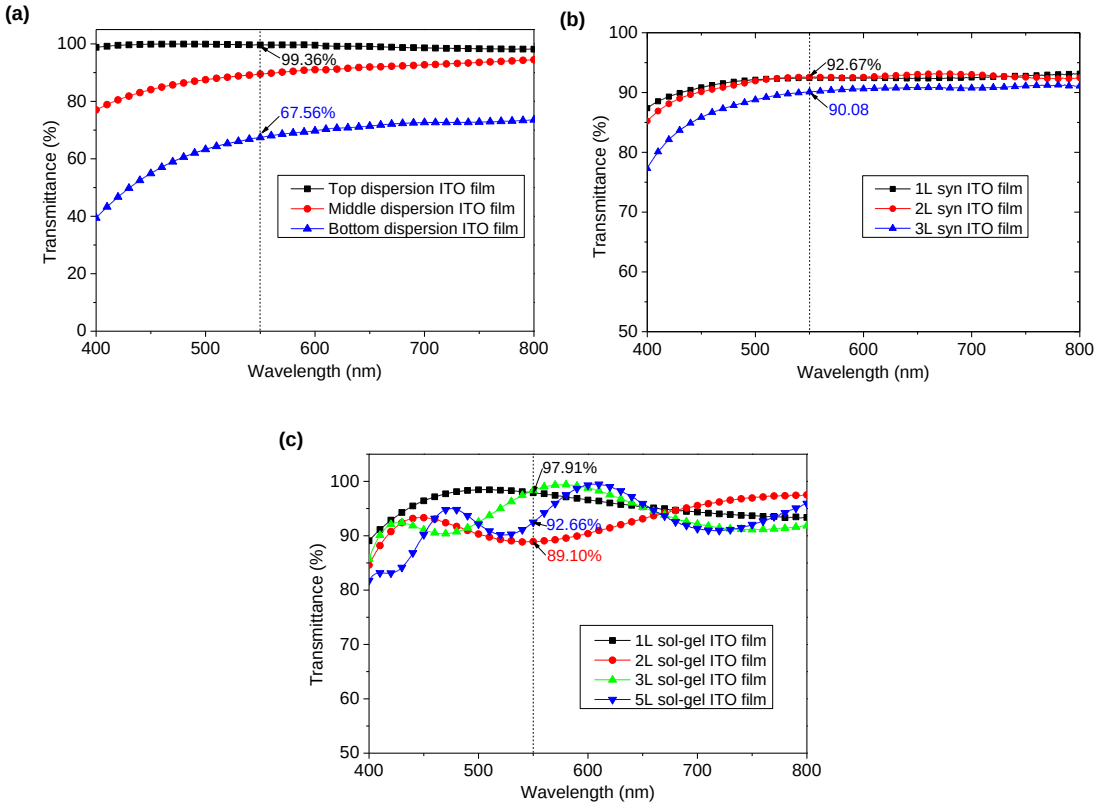

Figure A.2. UV-vis spectroscopy for all ITO films on glass substrates after annealing using the three ITO inks: (a) commercial ITO nanopowder-water dispersion; (b) synthesized ITO colloidal nanoparticle hexane dispersion; (c) sol-gel ITO ink (Figure A.2(a) and (c) are from [126]).

All of the ITO films were characterized by 2-probe AC impedance spectroscopy after annealing at 450°C using a hot plate. Figure A.3 shows representative impedance magnitude vs. logarithm of frequency curves for all three sets of samples.

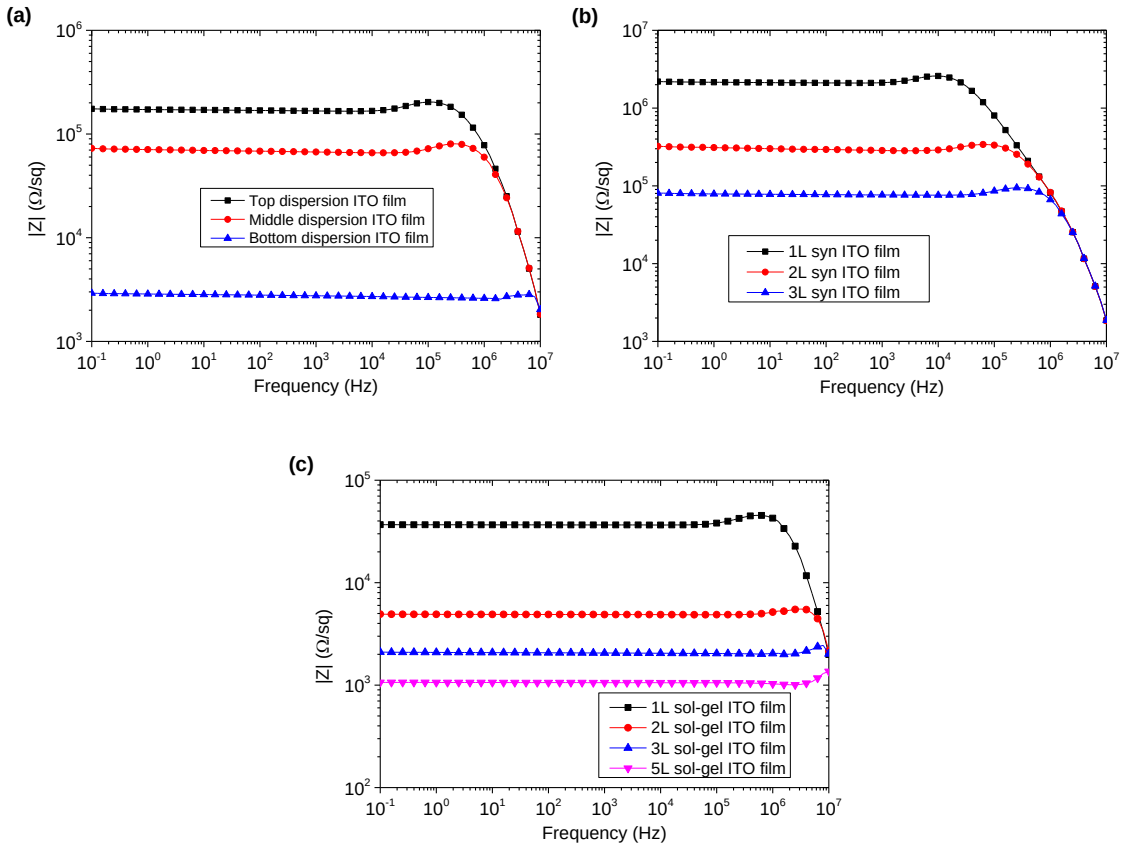

Figure A.3. Bode plots of |Z| for ITO films on glass substrates made from three inks. (a) Commercial ITO nanopowder-water dispersion; (b) synthesized ITO colloidal nanoparticle hexane dispersion; (c) sol-gel ITO ink.

For different types of ITO inks, building up thickness is always an effective method to lower the impedance magnitude. The films from ITO colloidal nanoparticles have impedances ranging from 10^4 Ω to 10^7 Ω. The lowest impedance magnitude of the three layer films was 8.31×10^4 Ω with a thickness of 1.4 μm. For commercial ITO nanopowder ink, there is a huge gap in the impedance magnitude between the middle dispersion ITO

films and the bottom dispersion ITO films. The reason might be the big difference in the film thickness. The middle dispersion ITO film is 7.52×10^4 Ω with 200 nm thickness when the bottom dispersion ITO film is 2.88×10^3 Ω with 3 μm thickness. As a comparison, the five layer sol-gel ITO films have the lowest impedance magnitude at 1.07×10^3 Ω only with 460 nm thickness.

A.2.2 Surface morphology

Figure A.4 shows the surface morphology of ITO films made from the three different ITO inks after 450°C annealing. The top set of images represent thinner samples and those on the bottom are thicker samples in the same series. These images were scanned by AFM in non-contact mode. The topography images contain a lot of surface information about the ITO films. For the commercial ITO nanopowder ink, the surface morphology of the ITO films looks smooth and the root mean square roughness (R_{ms}) increases with the film thickness. A small R_{ms} number means a smooth surface morphology. The R_{ms} of the top dispersion, middle dispersion and bottom dispersion ITO films were 12.2 nm, 13.5 nm and 33.1 nm, respectively (Figure A.4(a) and A.4(d) show top and bottom ones). One reason for a large R_{ms} number for the bottom dispersion ITO films may be the big ITO nanoparticles and nanoparticle aggregates at the bottom of the ITO ink. For synthesized ITO nanoparticle ink, the one layer film looks similar to the top dispersion ITO film and has an R_{ms} of 7.4 nm (shown in Figure A.4(b)). The three layer films are much rougher with an R_{ms} of 19.0 nm (Figure A.4(e)). For sol-gel ITO films (Figure A.4(c) and A.4(f)), the surface morphology of these films is very different from the other two methods. Volcano-shaped voids can be found on the film surface. This effect may be due to wetting phenomena of the sol-gel precursor [118] and/or fast solvent evaporation which increases

the viscosity of the sol-gel solution [129]. Since sol-gel ITO solids had the lightest residue left after TGA testing, these voids might also be formed by fast evaporation of acetylacetone and quick decomposition of [NO^{3-}] and [Cl^{-}] into gas during the annealing steps. Even with these voids, the sol-gel ITO films still had better R_{ms} values than the films made from the other inks. The number increased from only 3.7 nm to 8.0 nm for the one layer and five layer films, respectively. This means that the sol-gel ITO films have the smoothest surface morphology in all three types of ITO films when considering the R_{ms}.

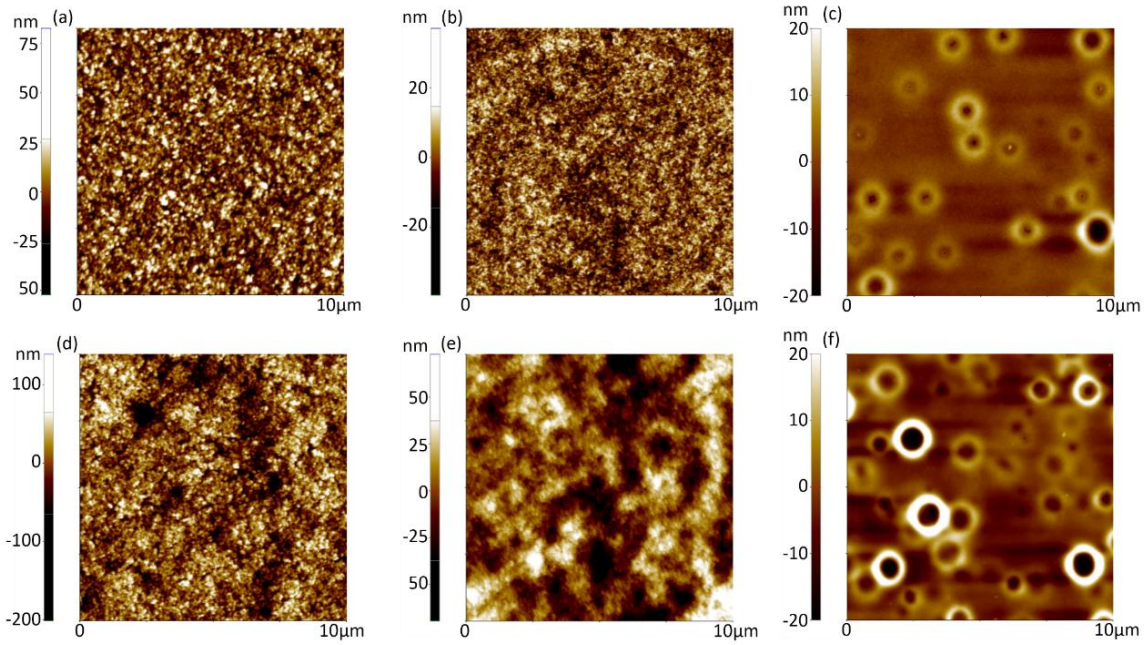

Figure A.4. 10 × 10 µm² NC-AFM images of ITO films on glass substrates made from three different inks. (a, d) Top and bottom commercial ITO nanopowder-water dispersion films; (b, e) 1-layer and 3-layer synthesized ITO colloidal nanoparticle hexane dispersion films; (c, f) 1-layer and 5-layer sol-gel ITO ink films (Figure A.4(a, c, d, f) are from reference [126]).

Non-contact AFM imaging can also provide particle size information on ITO films by looking at 1 × 1 µm² images as shown in Figure A.5. While the commercial ITO nanopowder had a particle size of 50 nm (Figure A.5(a)), the size of the nanoparticles for

the synthesized ITO particle films was about 20-30 nm in diameter (Figure A.5b). The sol-gel ITO ink had the smallest particle size on the film surface, which was about 10 nm (Figure A.5(c)). The particle size can strongly affect the surface morphology of thin films. In this image size (1 × 1 μm^2), the bottom dispersion ITO films had an R_{ms} of 24.7 nm, whereas the three layer synthesized ITO nanoparticle films had an R_{ms} of 15.5 nm. The sol-gel 5L ITO film has an R_{ms} of 1.14 nm, which is comparable to sputtered ITO films (1.1nm) [219]. Also, the changes of surface roughness numbers show that different image sizes can have different R_{ms} as was shown in Chapter 3.

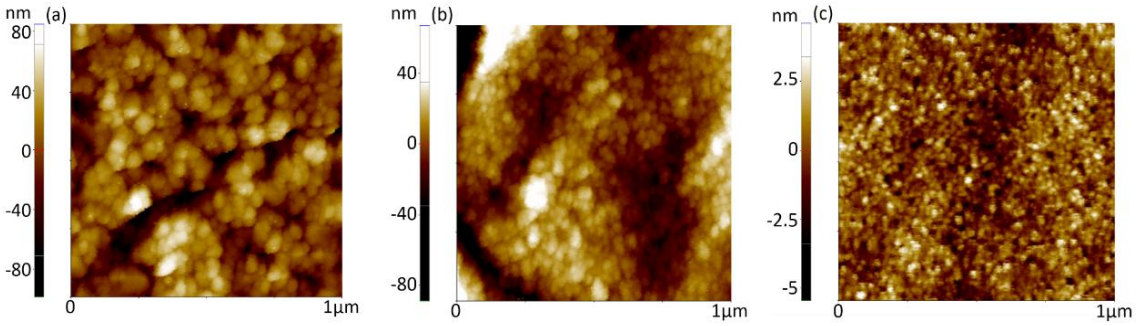

Figure A.5. 1 × 1 μm^2 NC-AFM images of ITO films on glass substrates made from three different inks: (a) commercial ITO nanopowder-water dispersion; (b) synthesized ITO colloidal nanoparticle hexane dispersion; (c) sol-gel ITO ink (Figure A.5(a, c) are from reference [126]).

A.2.3 Cross sectional images

SEM was used to take cross sectional images of the bottom dispersion ITO film and the sol-gel 5L ITO film (shown in Figure A.6). The average thickness for the bottom dispersion ITO film is around 3.1 μm. From the high magnification inset images, the porous structure and cracking in the middle of the cross section demonstrated that ITO nanoparticles were loosely connected to each other. This is mainly owing to the large ITO nanoparticles and

aggregates. Sol-gel 5L ITO films had a closed packing as well as five clearly distinguished deposited layers. The bottom layer is thicker than the other layers, whereas the top layer is thinner than the other layers. The total thickness is around 460 nm, which matched the contact AFM results.

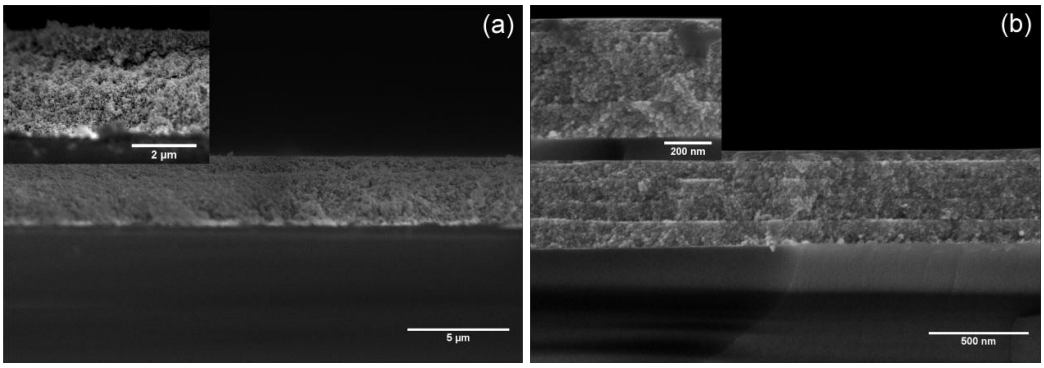

Figure A.6. SEM cross section images of (a) bottom dispersion ITO films and (b) sol-gel 5L ITO films on glass substrates (inset: higher magnification SEM images to show details) [126].

A.3 Conclusion

In this appendix, ITO films were fabricated by spin coating using three different custom-made ITO inks. Several characterization techniques were used to investigate these ITO films. The results show that the optical and electrical properties of ITO films are highly affected by the choice of the ITO ink and film thickness.

Among the three ITO inks, sol-gel ITO ink had the best combination of high optical transmittance and low sheet resistance although the surface morphology still can be improved. The sheet resistance of sol-gel 5L ITO films can be as low as 174 Ω/sq with a transmittance higher than 90%. In small areas, the surface roughness number can be comparable to that in sputtered ITO films.

APPENDIX B. ADDITIONAL IMPEDANCE SPECTROSCOPY FIGURES

B.1 Other dielectric functions for 1L ITO film

All the other dielectric functions from experimental data and equivalent circuit fitting results are presented to demonstrate that the equivalent circuit model fits all of the dielectric functions for 1L ITO film in Chapter 4. Black dots are experimental data, red lines are fitting curves. The equivalent circuit model is in Figure 5.18 inset.

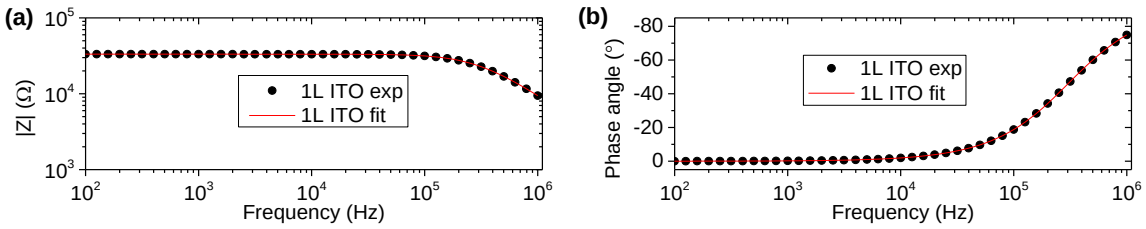

Figure B.1. Bode plots of (a) impedance magnitude |Z| and (b) phase angle with equivalent fitting results for 1L ITO film on quartz substrate.

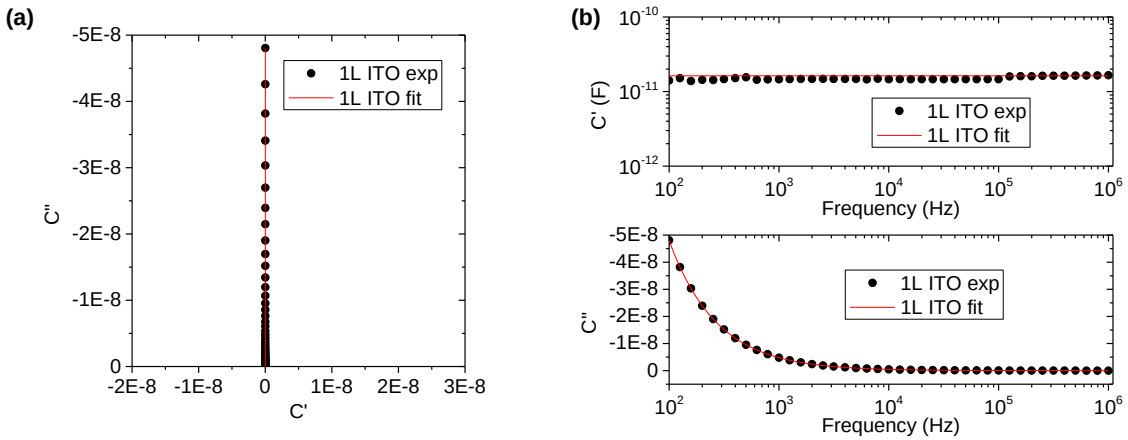

Figure B.2. (a) Nyquist plots and (b) Bode plots of capacitance (C*) with equivalent circuit fitting results for 1L ITO film on quartz substrate.

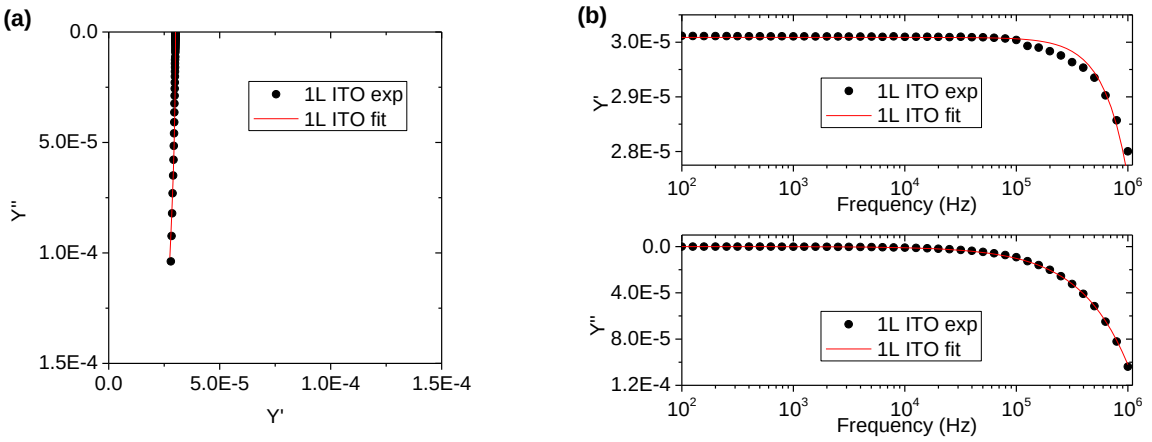

Figure B.3. (a) Nyquist plots and (b) Bode plots of admittance (Y*) with equivalent circuit fitting results for 1L ITO film on quartz substrate.

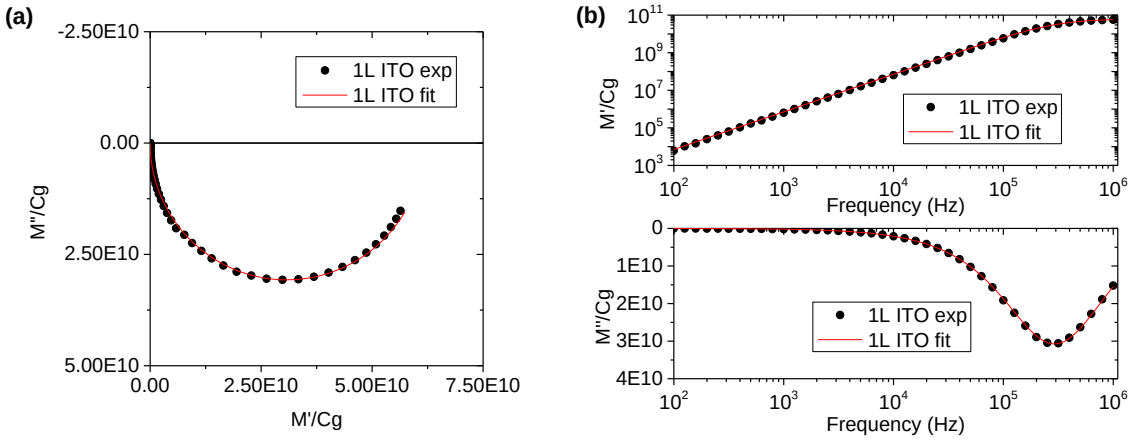

Figure B.4. (a) Nyquist plots and (b) Bode plots of modulus (M*) with equivalent circuit fitting results for 1L ITO film on quartz substrate.

B.2 Other dielectric functions for 5L ITO film

The equivalent circuit model in Figure 5.19 inset also gives good fitting for other dielectric functions of 5L ITO film in Chapter 4. Black dots are experimental data, red lines are fitting curves.

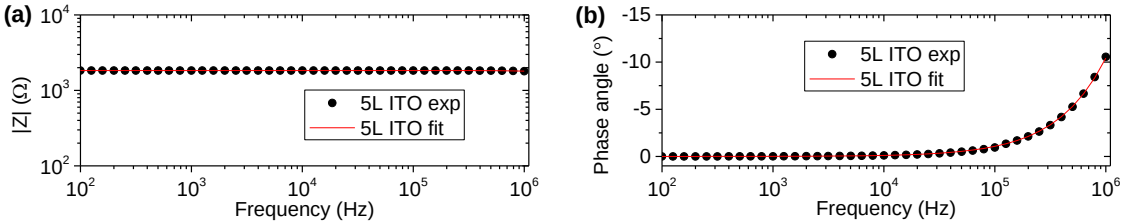

Figure B.5. Bode plots of (a) impedance magnitude |Z| and (b) phase angle with equivalent fitting results for 5L ITO film on quartz substrate.

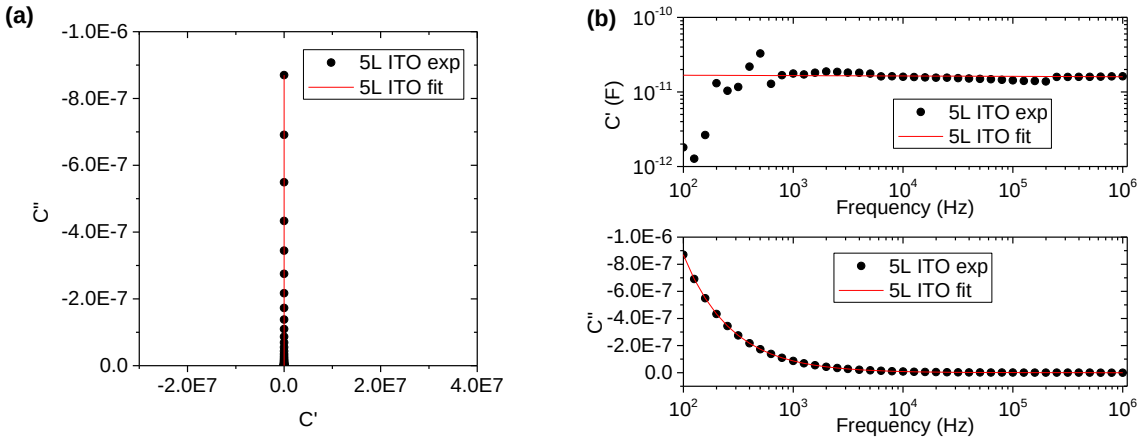

Figure B.6. (a) Nyquist plots and (b) Bode plots of capacitance (C*) with equivalent circuit fitting results for 5L ITO film on quartz substrate.

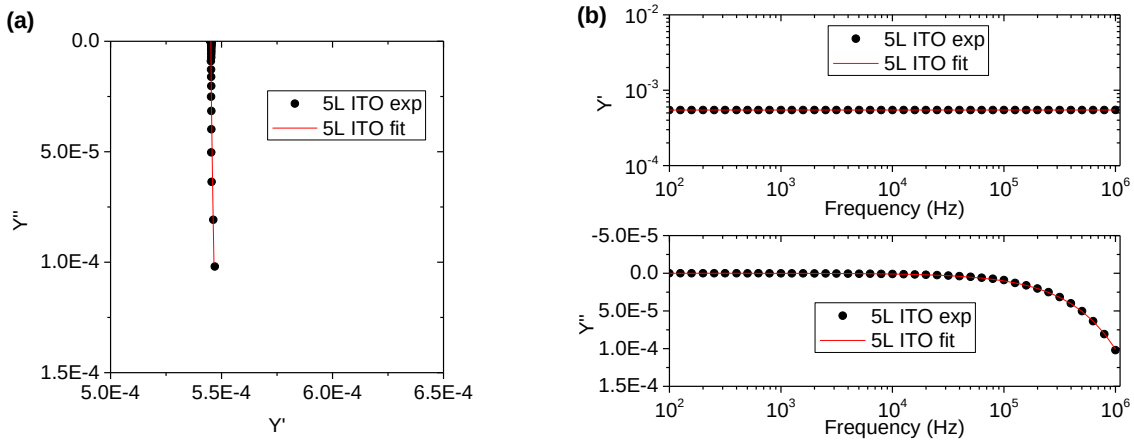

Figure B.7. (a) Nyquist plots and (b) Bode plots of capacitance (Y*) with equivalent circuit fitting results for 1L ITO film on quartz substrate.

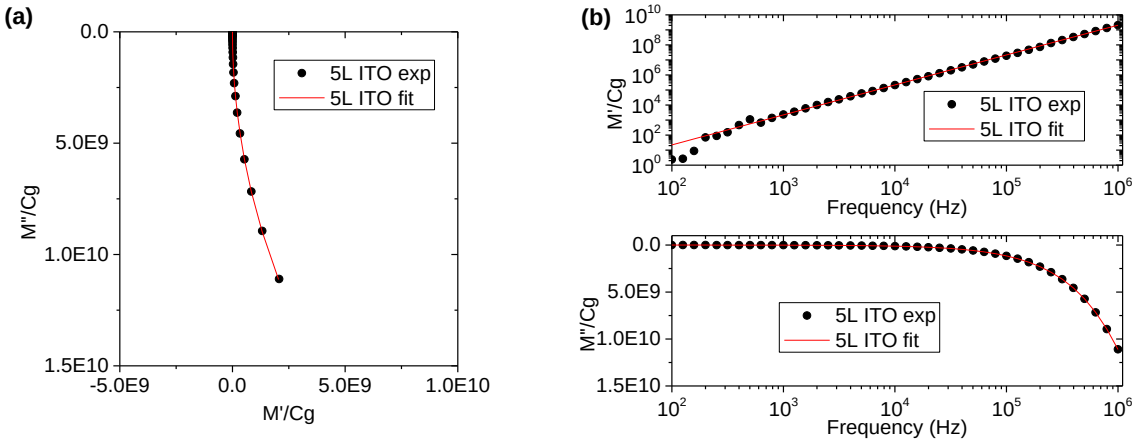

Figure B.8. (a) Nyquist plots and (b) Bode plots of modulus (M*) with equivalent circuit fitting results for 1L ITO film on quartz substrate.

B.3 Effect of annealing temperature on IS

The 1L ITO films were spin-coated on quartz glass substrates with the same method described in Chapter 3. The as-coated ITO films were quickly annealed at 120°C on hot plate for 10 minutes to remove moisture and residual solvent. Then the ITO films sample were annealed at different temperature from 300°C to 400°C on a hot plate for 10 minutes to find the critical temperature. Higher annealing temperature of 450°C, 550°C, 650°C and 750°C for 10 minutes (dwell time) were tested to anneal ITO films in a tube furnace under compressed air flow. Since the substrate was changed to quartz glass, much higher annealing temperature can be used. The samples were measured by Gamry 5000 for conducting ones and Gamry 3000 for insulating ones using 2-probe in-plane configuration. The ac voltage is fixed at 500 mV without dc bias. The frequency range is from 0.1 Hz to 1 MHz.

Figure B.9 shows that the impedance magnitude of 1L ITO films decreased with increasing annealing temperature from 300°C to 400°C. The difference of impedance magnitude is

more than 2 orders of magnitude between 360°C to 370°C when other 10°C range only have change less than 1 order. After 370°C, the change of impedance magnitude is small. It is possible that the a temperature between 360°C to 370°C is the point where the annealed 1L ITO film transitioned from insulating film to more conducting films. This phenomenon is similar to a percolation threshold effect in composite, which means a better conducting network forming inside ITO film.

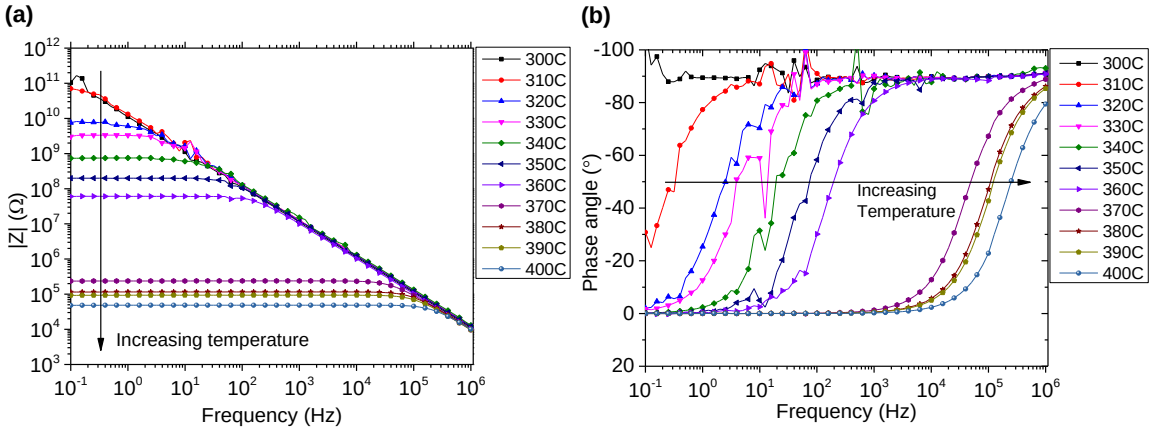

Figure B.9. Representative Bode plots of (a) impedance magnitude |Z| and (b) phase angle for 1L ITO films on quartz substrates annealed from 300°C to 400°C with 10°C interval on hot plate measured by Gamry setup.

Higher annealing temperature is one approach to reduce the resistance of solution-processed ITO films. Most hot plate cannot heat up to more than 500°C, thus a tube furnace is required to anneal the samples. The ramping rate is 50°C/min and the holding time is 10 minutes. Figure B.10 shows that the 1L 750°C annealed ITO films can have |Z| one order of magnitude smaller than the 1L 450°C annealed ITO films. The high temperature may further remove the impurities inside ITO films and improve the conducting network. Also, the tube furnace annealing may increase the grain size (polycrystalline ITO film) since the annealing time takes longer, considering ramping and cooling.

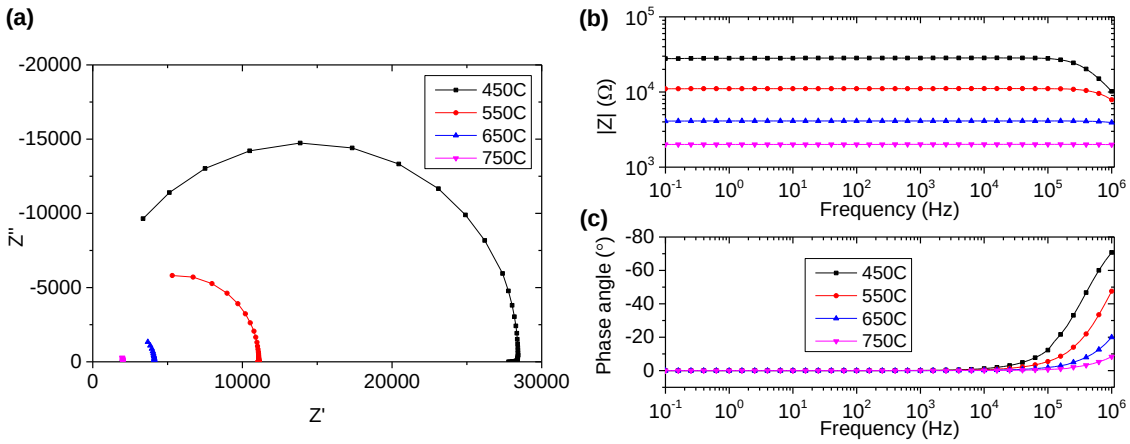

Figure B.10. (a) Representative Nyquist plots of impedance; Bode plots of (b) |Z| and (c) phase angle for 1L ITO films on quartz substrates annealed from 450°C to 750°C with 100°C interval in tube furnace measured by Gamry setup.

B.4 Impedance spectroscopy measured by different instruments

For the same ITO films, different instruments can give different results. Figure B.11 shows the Bode plots of impedance magnitude and phase angle for 300°C-400°C annealed 1L ITO films measured by Solartron instrument setup with the in-plane configuration. The Solartron instruments setup is designed for insulating samples whereas Gamry setup is ideal for conducting samples. At frequency of 0.1 Hz, the impedance magnitude of 300°C annealed 1L ITO film is about 10^{12} Ω measured from Solartron, about one order of magnitude higher than the result (10^{11} Ω) from Gamry in Figure B.9. Other ITO film samples have similar |Z| at low frequency from two instruments. When the overall shapes of Bode plots of |Z| are similar, it is noticed that there are small humps near the relaxation frequency in the Figure B.11(a). In addition, the Bode plots of phase angle from Solartron (Figure B.11(b)) show positive numbers, which indicates the existence of inductance or negative capacitance. In contrast, all the phase angle numbers measured from Gamry are from -90° to 0° without inductive behaviours in Figure B.9(b). The Solartron results are

similar to a previous group member's results of ITO films which were made from synthesized ITO nanoparticle colloid [176]. The explanation for the inductive behaviour was that negative resistance and negative capacitance both existed in the ITO films, which needs further experiments to confirm.

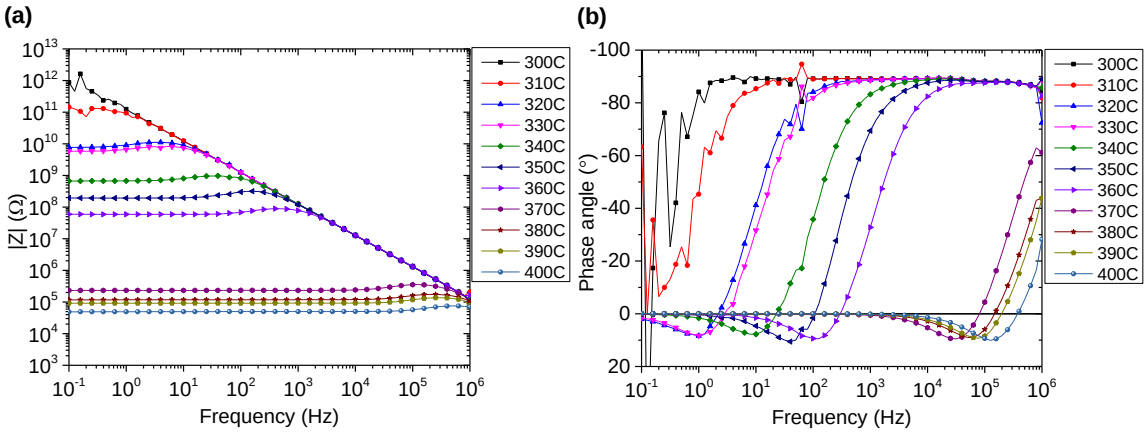

Figure B.11. Representative Bode plots of (a) |Z| and (b) phase angle for 1L ITO films on quartz substrates annealed from 300°C to 400°C with 10°C interval on hot plate measured by Solartron setup.

B.5 Impedance spectroscopy for other multi-layer ITO films

In Chapter 3, multi-layer ITO films made from spin-coating and ink-jet printing on glass substrates were only measured by 4-probe DC resistance method. The electrical properties of these ITO films were also measured by 2-probe AC impedance spectroscopy with Gamry instrument as shown in Figure B.12. The shape of Nyquist plots of these ITO films are similar to the ones shown in Chapter 5 and the same equivalent circuit model can be used. The fitting results from equivalent circuit model (inset of the images) match well with the experimental data, which further proves that our impedance models are correct.

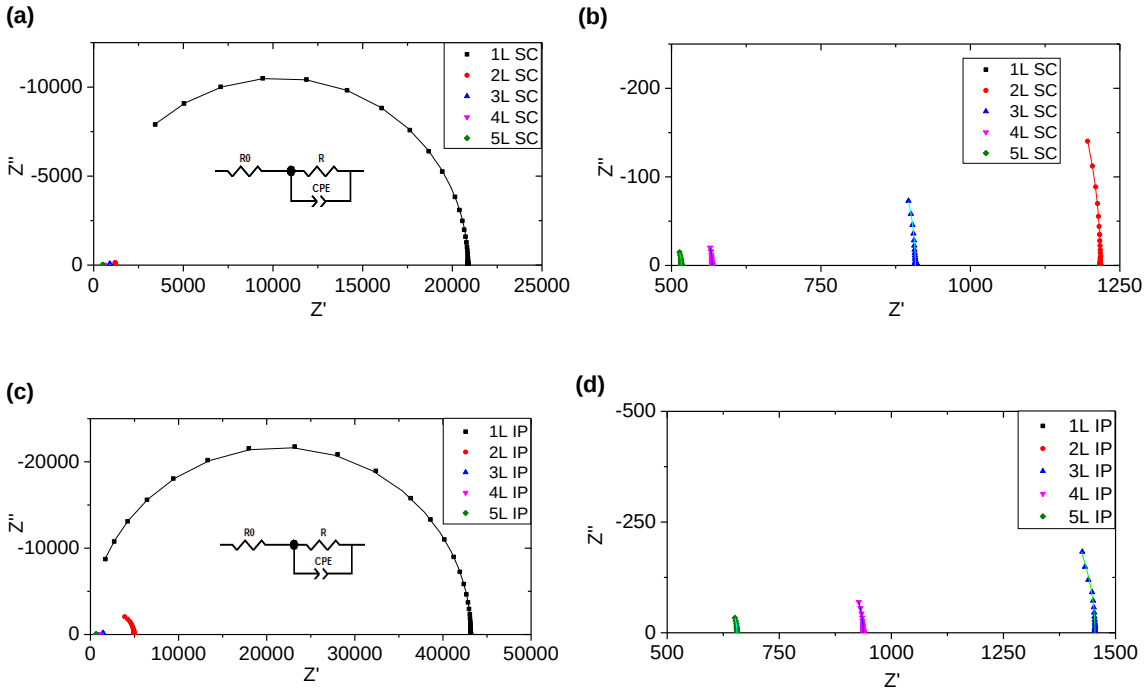

Figure B.12. Representative Nyquist plots of impedance for (a, b) multi-layer spin-coated (SC) ITO films and (c, d) multi-layer ink-jet printed (IP) ITO films on glass substrate. Different scales were used to better show all the curves. Symbols are the experimental data, curves are the fitting results from equivalent circuit model in the inset image.

REFERENCES

[1] Heller, A., D. E. Aspnes, J. D. Porter, T. T. Sheng, and R. G. Vadimsky. "Transparent metals preparation and characterization of light-transmitting platinum films." *The Journal of Physical Chemistry* 89, no. 21 (1985): 4444-4452.

[2] Jarrett, D. N., and L. Ward. "Optical properties of discontinuous gold films." *Journal of Physics D: Applied Physics* 9, no. 10 (1976): 1515.

[3] Sam, F. L. M., C. A. Mills, L. J. Rozanski, and S. R. P. Silva. "Thin film hexagonal gold grids as transparent conducting electrodes in organic light emitting diodes." *Laser & Photonics Reviews* 8, no. 1 (2014): 172-179.

[4] Peng, H., W. Dang, J. Cao, Y. Chen, D. Wu, W. Zheng, H. Li, Z. Shen, and Z. Liu. "Topological insulator nanostructures for near-infrared transparent flexible electrodes." *Nature Chemistry* 4, no. 4 (2012): 281-286.

[5] De, S., T. M. Higgins, P. E. Lyons, E. M. Doherty, P. N. Nirmalraj, W. J. Blau, J. J. Boland, and J. N. Coleman. "Silver nanowire networks as flexible, transparent, conducting films: extremely high DC to optical conductivity ratios." *ACS Nano* 3, no. 7 (2009): 1767-1774.

[6] Haacke, G. "Transparent conducting coatings." *Annual Review of Materials Science* 7, no. 1 (1977): 73-93.

[7] Valkonen, E., C. G. Ribbing, and J. E. Sundgren. "Optical constants of thin silver and titanium nitride films." In *Thin Film Technologies II* 652, pp. 235-243. International Society for Optics and Photonics, 1986.

[8] Ahn, B. Y., D. J. Lorang, and J. A. Lewis. "Transparent conductive grids via direct writing of silver nanoparticle inks." *Nanoscale* 3, no. 7 (2011): 2700-2702.

[9] Badeker, K. "Concerning the electricity conductibility and the thermoelectric energy of several heavy metal bonds." *Ann. Phys. (Leipzig)* 22, no. 4 (1907): 749-766.

[10] Lewis, B. G., and D. C. Paine. "Applications and processing of transparent conducting oxides." *Mrs Bulletin* 25, no. 8 (2000): 22-27.

[11] “Indium supply risk”, http://www.rsc.org/periodic-table/element/49/indium (Accessed Nov 14, 2017).

[12] Yu, S., H. Zheng, L. Li, and S. Chen. "Highly conducting and transparent antimony doped tin oxide thin films: the role of sputtering power density." *Ceramics International* 43, no. 7 (2017): 5654-5660.

[13] Cranton, W. M., N. Kalfagiannis, X. Hou, R. Ranson, and D. C. Koutsogeorgis. "Enhanced electrical and optical properties of room temperature deposited Aluminium doped Zinc Oxide (AZO) thin films by excimer laser annealing." *Optics and Lasers in Engineering* 80 (2016): 45-51.

[14] Banyamin, Z. Y., P. J. Kelly, G. West, and J. Boardman. "Electrical and optical properties of fluorine doped tin oxide thin films prepared by magnetron sputtering." *Coatings* 4, no. 4 (2014): 732-746.

[15] Heeger, A. J., A. G. MacDiarmid, and H. Shirakawa. "The Nobel Prize in chemistry, 2000: conductive polymers." *Stockholm, Sweden: Royal Swedish Academy of Sciences* (2000): 1-16.

[16] Nowaczyk, J., K. Kadac, and E. Olewnik-Kruszkowska. "Emulsion polymerization of thiophene–the new way of conducting polymers synthesis." *Advances in Science and Technology Research Journal* 9, no. 27 (2015): 118-122.

[17] Heeger, A. J., S. Kivelson, J. R. Schrieffer, and W-P. Su. "Solitons in conducting polymers." *Reviews of Modern Physics* 60, no. 3 (1988): 781.

[18] Tsang, E. M., Z. Zhang, Z. Shi, T. Soboleva, and S. Holdcroft. "Considerations of macromolecular structure in the design of proton conducting polymer membranes: graft versus diblock polyelectrolytes." *Journal of the American Chemical Society* 129, no. 49 (2007): 15106-15107.

[19] Ofer, D., R. M. Crooks, and M. S. Wrighton. "Potential dependence of the conductivity of highly oxidized polythiophenes, polypyrroles, and polyaniline: finite windows of high conductivity." *Journal of the American Chemical Society* 112, no. 22 (1990): 7869-7879.

[20] Cao, Y., G. M. Treacy, P. Smith, and A. J. Heeger. "Solution-cast films of polyaniline: Optical-quality transparent electrodes." *Applied Physics Letters* 60, no. 22 (1992): 2711-2713.

[21] Jang, J., and J. H. Oh. "Fabrication of a highly transparent conductive thin film from polypyrrole/poly (methyl methacrylate) core/shell nanospheres." *Advanced Functional Materials* 15, no. 3 (2005): 494-502.

[22] Vosgueritchian, M., D. J. Lipomi, and Z. Bao. "Highly conductive and transparent PEDOT: PSS films with a fluorosurfactant for stretchable and flexible transparent electrodes." *Advanced functional materials* 22, no. 2 (2012): 421-428.

[23] Le, T., Y. Kim, and H. Yoon. "Electrical and electrochemical properties of conducting polymers." *Polymers* 9, no. 4 (2017): 150.

[24] Krebs, F. C. "All solution roll-to-roll processed polymer solar cells free from indium-tin-oxide and vacuum coating steps." *Organic Electronics* 10, no. 5 (2009): 761-768.

[25] Wang, X., L. Zhi, and K. Müllen. "Transparent, conductive graphene electrodes for dye-sensitized solar cells." *Nano letters* 8, no. 1 (2008): 323-327.

[26] Wu, Z., Z. Chen, X. Du, J. M. Logan, J. Sippel, M. Nikolou, K. Kamaras, J. R. Reynolds, D. B. Tanner, A. F. Hebard, and A. G. Rinzler. "Transparent, conductive carbon nanotube films." *Science* 305, no. 5688 (2004): 1273-1276.

[27] Lopéz, I. P., L. Cattin, D. Nguyen, M. Morsli, and J. C. Bernède. "Dielectric/metal /dielectric structures using copper as metal and MoO_3 as dielectric for use as transparent electrode." *Thin Solid Films* 520, no. 20 (2012): 6419-6423.

[28] Kim, Y. S., J. H. Park, D. H. Choi, H. S. Jang, J. H. Lee, H. J. Park, J. I. Choi, D. H. Ju, J. Y. Lee, and Daeil Kim. "ITO/Au/ITO multilayer thin films for transparent conducting electrode applications." *Applied Surface Science* 254, no. 5 (2007): 1524-1527.

[29] Choi, K. H., J. Y. Kim, Y. S. Lee, and H. J. Kim. "ITO/Ag/ITO multilayer films for the application of a very low resistance transparent electrode." *Thin Solid Films* 341, no. 1 (1999): 152-155.

[30] Yu, S., L. Li, X. Lyu, and W. Zhang. "Preparation and investigation of nano-thick FTO/Ag/FTO multilayer transparent electrodes with high figure of merit." *Scientific Reports* 6 (2016): 20399.

[31] Sutthana, S., N. Hongsith, and S. Choopun. "AZO/Ag/AZO multilayer films prepared by DC magnetron sputtering for dye-sensitized solar cell application." *Current Applied Physics* 10, no. 3 (2010): 813-816.

[32] Jen, Y., A. Lakhtakia, M. Lin, W. Wang, H. Wu, and H. Liao. "Metal/dielectric/metal sandwich film for broadband reflection reduction." *Scientific Reports* 3 (2013): 1672.

[33] Brewer, S. H., and S. Franzen. "Calculation of the electronic and optical properties of indium tin oxide by density functional theory." *Chemical Physics* 300, no. 1 (2004): 285-293.

[34] Nadaud, N., N. Lequeux, M. Nanot, J. Jove, and T. Roisnel. "Structural studies of tin-doped indium oxide (ITO) and $In_4Sn_3O_{12}$." *Journal of Solid State Chemistry* 135, no. 1 (1998): 140-148.

[35] Buchholz, D. B., Q. Ma, D. Alducin, A. Ponce, M. Jose-Yacaman, R. Khanal, J. E. Medvedeva, and R. Chang. "The structure and properties of amorphous indium oxide." *Chemistry of Materials* 26, no. 18 (2014): 5401-5411.

[36] Frank, G., and H. Köstlin. "Electrical properties and defect model of tin-doped indium oxide layers." *Applied Physics A: Materials Science & Processing* 27, no. 4 (1982): 197-206.

[37] González, G. B., J. B. Cohen, J. Hwang, T. O. Mason, J. P. Hodges, and J. D. Jorgensen. "Neutron diffraction study on the defect structure of indium–tin–oxide." *Journal of Applied Physics* 89, no. 5 (2001): 2550-2555.

[38] Bel Hadj Tahar, R., T. Ban, Y. Ohya, and Y. Takahashi. "Tin doped indium oxide thin films: Electrical properties." *Journal of Applied Physics* 83, no. 5 (1998): 2631-2645.

[39] Fan, J. C., and J. B. Goodenough. "X-ray photoemission spectroscopy studies of Sn-doped indium-oxide films." *Journal of Applied Physics* 48, no. 8 (1977): 3524-3531.

[40] Warschkow, O., D. E. Ellis, G. B. González, and T. O. Mason. "Defect Structures of Tin-Doped Indium Oxide." *Journal of the American Ceramic Society* 86, no. 10 (2003): 1700-1706.

[41] Berggren, K-F., B. E. Sernelius, L. Engström, I. Hamberg, and C. G. Granqvist. "Bandgap Widening in Heavily Sn-Doped In_2O_3." In *Proceedings of the 17th International Conference on the Physics of Semiconductors*, pp. 1051-1054. Springer, New York, NY, 1985.

[42] Mryasov, O. N., and A. J. Freeman. "Electronic band structure of indium tin oxide and criteria for transparent conducting behavior." *Physical Review B* 64, no. 23 (2001): 233111.

[43] Pammi, S. V., A. Chanda, J. Ahn, J. Park, C. Cho, W. Lee, and S. Yoon. "Low resistivity ITO thin films deposited by NCD technique at low temperature: variation of tin concentration." *Journal of the Electrochemical Society* 157, no. 10 (2010): 937-941.

[44] Pasquarelli, R. M., D. S. Ginley, and R. O'Hayre. "Solution processing of transparent conductors: from flask to film." *Chemical Society Reviews* 40, no. 11 (2011): 5406-5441.

[45] Johnson, V., and K. Lark-Horovitz. "Erratum: Transition from Classical to Quantum Statistics in Germanium Semiconductors at Low Temperature." *Physical Review* 71, no .12 (1947): 909.

[46] Frank, G., L. Brock, and H. D. Bausen. "The solubilities of Sn in In_2O_3 and of In in SnO_2 crystals grown from Sn—In melts." *Journal of Crystal Growth* 36, no. 1 (1976): 179-180.

[47] Meng, L., and M. P. Dos Santos. "Properties of indium tin oxide films prepared by rf reactive magnetron sputtering at different substrate temperature." *Thin Solid Films* 322, no. 1 (1998): 56-62.

[48] Gupta, L., A. Mansingh, and P. K. Srivastava. "Band gap narrowing and the band structure of tin-doped indium oxide films." *Thin Solid Films* 176, no. 1 (1989): 33-44.

[49] Bierwagen, O., M. E. White, M. Tsai, and J. S. Speck. "Plasma-assisted molecular beam epitaxy of high quality In_2O_3 (001) thin films on Y-Stabilized ZrO_2 (001) using In as an auto surfactant." *Applied Physics Letters* 95, no. 26 (2009): 262105.

[50] Edwards, P. P., A. Porch, M. O. Jones, D. V. Morgan, and R. M. Perks. "Basic materials physics of transparent conducting oxides." *Dalton Transactions* 19 (2004): 2995-3002.

[51] Erhart, P., A. Klein, R. G. Egdell, and K. Albe. "Band structure of indium oxide: Indirect versus direct band gap." *Physical Review B* 75, no. 15 (2007): 153205.

[52] Mason, M. G., L. S. Hung, C. W. Tang, S. T. Lee, K. W. Wong, and M. Wang. "Characterization of treated indium–tin–oxide surfaces used in electroluminescent devices." *Journal of Applied Physics* 86, no. 3 (1999): 1688-1692.

[53] Bourlange, A., D. J. Payne, R. G. Egdell, J. S. Foord, P. P. Edwards, M. O. Jones, A. Schertel, P. J. Dobson, and J. L. Hutchison. "Growth of In_2O_3 (100) on Y-stabilized ZrO_2 (100) by O-plasma assisted molecular beam epitaxy." *Applied Physics Letters* 92, no. 9 (2008): 092117.

[54] King, P. D. C., Tim D. Veal, F. Fuchs, C. Y. Wang, D. J. Payne, A. Bourlange, H. Zhang, G. R. Bell, V. Cimalla, O. Ambacher and R. G. Egdell. "Band gap, electronic structure, and surface electron accumulation of cubic and rhombohedral In_2O_3." *Physical Review B* 79, no. 20 (2009): 205211.

[55] Bierwagen, O., J. S. Speck, T. Nagata, T. Chikyow, Y. Yamashita, H. Yoshikawa, and K. Kobayashi. "Depletion of the In_2O_3 (001) and (111) surface electron accumulation by an oxygen plasma surface treatment." *Applied Physics Letters* 98, no. 17 (2011): 172101.

[56] Morkoc, H., S. Strite, G. B. Gao, M. E. Lin, B. Sverdlov, and M. Burns. "Large-band-gap SiC, III-V nitride, and II-VI ZnSe-based semiconductor device technologies." *Journal of Applied Physics* 76, no. 3 (1994): 1363-1398.

[57] Yap, S. Shan, T. K. Yong, C. H. Nee, and T. Y. Tou. "Pulsed Laser Deposition of ITO: From Films to Nanostructures." In *Applications of Laser Ablation-Thin Film Deposition, Nanomaterial Synthesis and Surface Modification*. InTech, 2016.

[58] Bierwagen, O. "Indium oxide—a transparent, wide-band gap semiconductor for (opto) electronic applications." *Semiconductor Science and Technology* 30, no. 2 (2015): 024001.

[59] De Carvalho, C. N., A. Luis, O. Conde, E. Fortunato, G. Lavareda, and A. Amaral. "Effect of rf power on the properties of ITO thin films deposited by plasma enhanced reactive thermal evaporation on unheated polymer substrates." *Journal of Non-crystalline Solids* 299 (2002): 1208-1212.

[60] Ishida, T., H. Kobayashi, and Y. Nakato. "Structures and properties of electron-beam-evaporated indium tin oxide films as studied by X-ray photoelectron spectroscopy and work-function measurements." *Journal of Applied Physics* 73, no. 9 (1993): 4344-4350.

[61] Kim, H., J. S. Horwitz, G. P. Kushto, Z. H. Kafafi, and D. B. Chrisey. "Indium tin oxide thin films grown on flexible plastic substrates by pulsed-laser deposition for organic light-emitting diodes." *Applied Physics Letters* 79, no. 3 (2001): 284-286.

[62] Maruyama, T., and K. Fukui. "Indium-tin oxide thin films prepared by chemical vapor deposition." *Journal of Applied Physics* 70, no. 7 (1991): 3848-3851.

[63] Latz, R., K. Michael, and M. Scherer. "High conducting large area indium tin oxide electrodes for displays prepared by DC magnetron sputtering." *Japanese Journal of Applied Physics* 30, no. 2A (1991): L149.

[64] Jilani, A., M. S. Abdel-wahab, and A. H. Hammad. "Advance Deposition Techniques for Thin Film and Coating." *Modern Technologies for Creating the Thin-film Systems and Coatings*. InTech, 2017.

[65] Vaziri, M. R., and F. Hajiesmaeilbaigi. "Optical and structural properties of copper nanostructured thin films prepared by pulsed laser deposition." *Optik-International Journal for Light and Electron Optics* 126, no. 14 (2015): 1348-1351.

[66] "Chemical vapor deposition", https://www.memsnet.org/mems/processes/deposition.html (Accessed Nov 14, 2017).

[67] You, Y. Z., Y. S. Kim, D. H. Choi, H. S. Jang, J. H. Lee, and Daeil Kim. "Electrical and optical study of ITO films on glass and polymer substrates prepared by DC magnetron sputtering type negative metal ion beam deposition." *Materials Chemistry and Physics* 107, no. 2 (2008): 444-448.

[68] Ober, J. A. *Mineral commodity summaries* 2017. US Geological Survey, 2017.

[69] Chamberlin, R. R., and J. S. Skarman. "Chemical spray deposition process for inorganic films." *Journal of the Electrochemical Society* 113, no. 1 (1966): 86-89.

[70] Lee, J., M. A. Petruska, and S. Sun. "Surface Modification and assembly of transparent indium tin oxide nanocrystals for enhanced conductivity." *The Journal of Physical Chemistry C* 118, no. 22 (2014): 12017-12021.

[71] Mahajeri, M., A. Schneider, M. Baum, T. Rechtenwald, M. Voigt, M. Schmidt, and W. Peukert. "Production of dispersions with small particle size from commercial indium tin oxide powder for the deposition of highly conductive and transparent films." *Thin Solid Films* 520, no. 17 (2012): 5741-5745.

[72] Shaheen, S. E., R. Radspinner, N. Peyghambarian, and G. E. Jabbour. "Fabrication of bulk heterojunction plastic solar cells by screen printing." *Applied Physics Letters* 79, no. 18 (2001): 2996-2998.

[73] Hong, S., Y. Kim, and J. Han. "Development of ultrafine indium tin oxide (ITO) nanoparticle for ink-jet printing by low-temperature synthetic method." *IEEE Transactions on nanotechnology* 7, no. 2 (2008): 172-176.

[74] Kim, S., S. Choi, C. Park, and H. Jin. "Transparent conductive ITO thin films through the sol-gel process using metal salts." *Thin Solid Films* 347, no. 1 (1999): 155-160.

[75] Dippel, A., T. Schneller, P. Gerber, and R. Waser. "Morphology control of highly-transparent indium tin oxide thin films prepared by a chlorine-reduced metallo-organic decomposition technique." *Thin solid films* 515, no. 7 (2007): 3797-3801.

[76] Gilstrap, R. A., C. J. Capozzi, C. G. Carson, R. A. Gerhardt, and C. J. Summers. "Synthesis of a nonagglomerated indium tin oxide nanoparticle dispersion." *Advanced Materials* 20, no. 21 (2008): 4163-4166.

[77] Narayanaswamy, A., H. Xu, N. Pradhan, M. Kim, and X. Peng. "Formation of nearly monodisperse In_2O_3 nanodots and oriented-attached nanoflowers: hydrolysis and alcoholysis vs pyrolysis." *Journal of the American Chemical Society* 128, no. 31 (2006): 10310-10319.

[78] Lee, J., S. Lee, G. Li, M. A. Petruska, D. C. Paine, and S. Sun. "A facile solution-phase approach to transparent and conducting ITO nanocrystal assemblies." *Journal of the American Chemical Society* 134, no. 32 (2012): 13410-13414.

[79] Ito, T., H. Uchiyama, and H. Kozuka. "Evaporation-Driven Deposition of ITO Thin Films from Aqueous Solutions with Low-Speed Dip-Coating Technique." *Langmuir* 33 (2017): 5314−5320.

[80] Sunde, T. O. L., E. Garskaite, B. Otter, H. E. Fossheim, R. Sæterli, R. Holmestad, M. Einarsrud, and T. Grande. "Transparent and conducting ITO thin films by spin coating of an aqueous precursor solution." *Journal of Materials Chemistry* 22, no. 31 (2012): 15740-15749.

[81] Park, T., and D. Kim. "Excimer laser sintering of indium tin oxide nanoparticles for fabricating thin films of variable thickness on flexible substrates." *Thin Solid Films* 578 (2015): 76-82.

[82] Ito, Y., H. Shiki, H. Takikawa, T. Ootsuka, T. Okawa, S. Yamanaka, and E. Usuki. "Low-temperature sintering of indium tin oxide thin film using split gliding arc plasma." *Japanese Journal of Applied Physics* 47, no. 8S2 (2008): 6956.

[83] Zimmerman, J., and J. A. Martino. "Touch-screen image scrolling system and method." U.S. Patent 6,690,387, issued February 10, 2004.

[84] Yoshida, H., S. Izhar, E. Nishio, Y. Utsumi, N. Kakimori, and S. A. Feridoun. "Recovery of indium from TFT and CF glasses in LCD panel wastes using sub-critical water." *Solar Energy Materials and Solar Cells* 125 (2014): 14-19.

[85] Yoshino, T., N. Baba, and Y. Kouda. "Electrochromic Properties of V_2O_5 Thin Films Colloid-Chemically Deposited onto ITO Glasses." *Japanese Journal of Applied Physics* 26, no. 5 (1987): 782.

[86] H. K. Yu, W. J. Dong, G. H. Jung, and J. L. Lee, "Three-dimensional nanobranched indium–tin-oxide anode for organic solar cells," *ACS nano* 5, no. 10 (2011): 8026-8032.

[87] Bae, S., S. J. Kim, D. Shin, J. Ahn, and B. H. Hong. "Towards industrial applications of graphene electrodes." *Physica Scripta* 2012, no. 146 (2012): 014024.

[88] Kim, H., S. Lee, and K. Yun. "Capacitive tactile sensor array for touch screen application." *Sensors and Actuators A: Physical* 165, no. 1 (2011): 2-7.

[89] Ivanov, I. N., M. P. Garrett, and R. A. Gerhardt. "Carbon nanotube assemblies for transparent conducting electrodes." In *Nanoscale Applications for Information and Energy Systems*, pp. 117-148. Springer, New York, NY, 2013.

[90] Crawley, R. L., K. E. Nietering, and J. W. Proscia. "Multilayer coating for defrosting glass." U.S. Patent 5,756,192, issued May 26, 1998.

[91] Cannavale, A., P. Cossari, G. E. Eperon, S. Colella, F. Fiorito, G. Gigli, H. J. Snaith, and A. Listorti. "Forthcoming perspectives of photoelectrochromic devices: a critical review." *Energy & Environmental Science* 9, no. 9 (2016): 2682-2719.

[92] Baetens, R., B. P. Jelle, and A. Gustavsen. "Properties, requirements and possibilities of smart windows for dynamic daylight and solar energy control in buildings: A state-of-the-art review." *Solar Energy Materials and Solar Cells* 94, no. 2 (2010): 87-105.

[93] Im, K., K. Cho, J. Kim, and S. Kim. "Transparent heaters based on solution-processed indium tin oxide nanoparticles." *Thin Solid Films* 518, no. 14 (2010): 3960-3963.

[94] Palenzuela, J., A. Viñuales, I. Odriozola, G. Cabañero, H. J. Grande, and V. Ruiz. "Flexible viologen electrochromic devices with low operational voltages using reduced graphene oxide electrodes." *ACS Applied Materials & Interfaces* 6, no. 16 (2014): 14562-14567.

[95] Li, G., R. Zhu, and Y. Yang. "Polymer solar cells." *Nature Photonics* 6, no. 3 (2012): 153-161.

[96] Hagfeldt, A., G. Boschloo, L. Sun, L. Kloo, and H. Pettersson. "Dye-sensitized solar cells." *Chemical Reviews* 110, no. 11 (2010): 6595-6663.

[97] Zhou, Y., P. Chen, S. Liu, G. Wang, H. Jiang, and S. Zhan. "Thermal stress analysis of mesoporous perovskite solar cell by finite element method." In *Electronic Packaging Technology (ICEPT), 2015 16th International Conference on*, pp. 205-209. IEEE, 2015.

[98] Chen, Z., W. Li, R. Li, Y. Zhang, G. Xu, and H. Cheng. "Fabrication of highly transparent and conductive indium–tin oxide thin films with a high figure of merit via solution processing." *Langmuir* 29, no. 45 (2013): 13836-13842.

[99] Hall, D. B., P. Underhill, and J. M. Torkelson. "Spin coating of thin and ultrathin polymer films." *Polymer Engineering & Science* 38, no. 12 (1998): 2039-2045.

[100] Binnig, G., C. F. Quate, and C. Gerber. "Atomic force microscope." *Physical review letters* 56, no. 9 (1986): 930.

[101] Coats, A. W., and J. P. Redfern. "Thermogravimetric analysis. A review." *Analyst* 88, no. 1053 (1963): 906-924.

[102] Warren, B. E. *X-ray Diffraction*, pp. 51-74. Courier Corporation, North Chelmsford, MA, 1969.

[103] Reichelt, R. "Scanning electron microscopy." In *Science of microscopy*, pp. 133-272. Springer, New York, NY, 2007.

[104] Perkampus, H., and H. Grinter. *UV-VIS Spectroscopy and its Applications*, pp. 3-9. Springer, Berlin, Heidelberg, 1992.

[105] Miccoli, I., F. Edler, H. Pfnür, and C. Tegenkamp. "The 100th anniversary of the four-point probe technique: the role of probe geometries in isotropic and anisotropic systems." *Journal of Physics: Condensed Matter* 27, no. 22 (2015): 223201.

[106] Penfold, J., and R. K. Thomas. "The application of the specular reflection of neutrons to the study of surfaces and interfaces." *Journal of Physics: Condensed Matter* 2, no. 6 (1990): 1369.

[107] Lauter, V., H. Ambaye, R. Goyette, W. H. Lee, and A. Parizzi. "Highlights from the magnetism reflectometer at the SNS." *Physica B: Condensed Matter* 404, no. 17 (2009): 2543-2546.

[108] "Magnetism Reflectometer", https://neutrons.ornl.gov/mr (Accessed Nov 14, 2017).

[109] Schmitt, J., and H. Flemming. "FTIR-spectroscopy in microbial and material analysis." *International Biodeterioration & Biodegradation* 41, no. 1 (1998): 1-11.

[110] Howard, D. L., H. G. Kjaergaard, J. Huang, and M. Meuwly. "Infrared and near-infrared spectroscopy of acetylacetone and hexafluoroacetylacetone." *The Journal of Physical Chemistry A* 119, no. 29 (2015): 7980-7990.

[111] Tayyari, S. F., and F. Milani-Nejad. "Vibrational assignment of acetylacetone." *Spectrochimica Acta Part A: Molecular and Biomolecular Spectroscopy* 56, no. 14 (2000): 2679-2691.

[112] Mahfouz, R. M., S. Al-Ahmari, A. Al-Fawaz, Z. Al-Othman, I. K. Warad, and M. R. H. Siddiqui. "Kinetic analysis for non-isothermal decomposition of unirradiated and γ-irradiated indium acetyl acetonate." *Materials Research* 14, no. 1 (2011): 7-10.

[113] Luo, S., J. Feng, and K. M. Ng. "Effect of fatty acid on the formation of ITO nanocrystals via one-pot pyrolysis reaction." *CrystEngComm* 17, no. 5 (2015): 1168-1172.

[114] Jafan, M. M., M. Zamani-Meymian, R. Rahimi, and M. Rabbani. "The effect of solvents and the thickness on structural, optical and electrical properties of ITO thin films

prepared by a sol–gel spin-coating process." *Journal of Nanostructure in Chemistry* 4, no. 1 (2014): 89.

[115] Celik, E., U. Aybarc, M. F. Ebeoglugil, I. Birlik, and O. Culha. "ITO films on glass substrate by sol–gel technique: synthesis, characterization and optical properties." *Journal of Sol-gel Science and Technology* 50, no. 3 (2009): 337-347.

[116] Das, N., and P. K. Biswas. "Synthesis and characterization of smoke-like porous sol–gel indium tin oxide coatings on glass." *Journal of Materials Science* 47, no. 1 (2012): 289-298.

[117] Puri, P., and V. Yang. "Effect of particle size on melting of aluminum at nano scales." *The Journal of Physical Chemistry C* 111, no. 32 (2007): 11776-11783.

[118] Wachtman, J. B., and R. A. Haber. "Ceramic films and coatings." pp. 328. Noyes Publications, Park Ridge, NJ, 1993.

[119] Joshi, S. M., and R. A. Gerhardt. "Effect of annealing atmosphere (Ar vs. air) and temperature on the electrical and optical properties of spin-coated colloidal indium tin oxide films." *Journal of Materials Science* 48, no. 4 (2013): 1465-1473.

[120] Yonkoski, R. K., and D. S. Soane. "Model for spin coating in microelectronic applications." *Journal of applied physics* 72, no. 2 (1992): 725-740.

[121] Xia, N., and R. A. Gerhardt. "All-printed liquid crystal display devices made from sol-gel Indium tin oxide (ITO) ink." *Advanced Manufacturing, Electronics and Microsystems*, chapter 4, (2016):163-167.

[122] Birnie, D. P. "Rational solvent selection strategies to combat striation formation during spin coating of thin films." *Journal of Materials Research* 16, no. 4 (2001): 1145-1154.

[123] Taylor, D. J., and D. P. Birnie. "A Case Study in Striation Prevention by Targeted Formulation Adjustment: Aluminum Titanate Sol-Gel Coatings." *Chemistry of materials* 14, no. 4 (2002): 1488-1492.

[124] Uchiyama, H., W. Namba, and H. Kozuka. "Spontaneous formation of linear striations and cell-like patterns on dip-coating titania films prepared from alkoxide solutions." *Langmuir* 26, no. 13 (2010): 11479-11484.

[125] Stenzel-Rosenbaum, M. H., T. P. Davis, A. G. Fane, and V. Chen. "Porous Polymer Films and Honeycomb Structures Made by the Self-Organization of Well-Defined Macromolecular Structures Created by Living Radical Polymerization Techniques." *Angewandte Chemie* 113, no. 18 (2001): 3536-3540.

[126] Xia, N., and R. A. Gerhardt. "Fabrication and characterization of highly transparent and conductive indium tin oxide films made with different solution-based methods." *Materials Research Express* 3, no. 11 (2016): 116408.

[127] Zhang, J., A. C. E. Chia, and R. R. LaPierre. "Low resistance indium tin oxide contact to n-GaAs nanowires." *Semiconductor Science and Technology* 29, no. 5 (2014): 054002.

[128] Xia, N., V. Lauter and R. A. Gerhardt. “Three-dimensional nanoscale sensing of porosity in solution-processed ITO multilayer thin films.” 2017, submitted draft.

[129] Predoana, L., S. Preda, M. Nicolescu, M. Anastasescu, J. M. Calderon-Moreno, M. Duta, M. Gartner, and M. Zaharescu. "Influence of the substrate type on the microstructural, optical and electrical properties of sol–gel ITO films." *Journal of sol-gel science and technology* 71, no. 2 (2014): 303-312.

[130] Ederth, J., G. A. Niklasson, A. Hultåker, P. Heszler, C. G. Granqvist, A. R. van Doorn, M. J. Jongerius, and D. Burgard. "Characterization of porous indium tin oxide thin films using effective medium theory." *Journal of applied physics* 93, no. 2 (2003): 984-988.

[131] Bruggeman, D. A. G. "The calculation of various physical constants of heterogeneous substances. I. The dielectric constants and conductivities of mixtures composed of isotropic substances." *Annals of Physics* 416 (1935): 636-791.

[132] Daoudi, K., B. Canut, M. G. Blanchin, C. S. Sandu, V. S. Teodorescu, and J. A. Roger. "Tin-doped indium oxide thin films deposited by sol–gel dip-coating technique." *Materials Science and Engineering: C* 21, no. 1 (2002): 313-317.

[133] Stoica, T. F., M. Gartner, T. Stoica, M. Losurdo, V. S. Teodorescu, M. G. Blanchin, and M. Zaharescu. "Properties of high-porosity sol-gel derived indium-tin oxide films." *Journal of Optoelectronics and Advanced Materials* 7, no. 5 (2005): 2353-2358.

[134] Tolan, M. "X-ray scattering from soft-matter thin films-materials science and basic research-introduction." In *X-ray scattering from soft-matter thin films*, pp. 5-31. Springer, Berlin, Heidelberg, 1999.

[135] Wang, Y., Y. Yang, X. Wang, and Y. Li. "Readout for a large area neutron sensitive microchannel plate detector." *Nuclear Instruments and Methods in Physics Research Section A: Accelerators, Spectrometers, Detectors and Associated Equipment* 784 (2015): 226-231.

[136] Demkowicz, M. J., and J. Majewski. "Probing Interfaces in Metals Using Neutron Reflectometry." *Metals* 6, no. 1 (2016): 20.

[137] Sperling, L. H. *Introduction to physical polymer science*. John Wiley & Sons, 2005.

[138] Lauter-Pasyuk, V., H. J. Lauter, D. Ausserre, Y. Gallot, V. Cabuil, B. Hamdoun, and E. I. Kornilov. "Neutron reflectivity studies of composite nanoparticle–copolymer thin films." *Physica B: Condensed Matter* 248, no. 1 (1998): 243-245.

[139] Lauter-Pasyuk, V. "Neutron grazing incidence techniques for nano-science." *Collection SFN* 7 (2007): 221-240.

[140] Peng, C., Y. S. Thio, R. A. Gerhardt, H. Ambaye, and V. Lauter. "pH-promoted exponential layer-by-layer assembly of bicomponent polyelectrolyte/nanoparticle multilayers." *Chemistry of Materials* 23, no. 20 (2011): 4548-4556.

[141] Toperverg, B., V. Lauter, H. Lauter, O. Nikonov, D. Ausserre, and Y. Gallot. "Morphology of off-specular neutron scattering pattern from islands on a lamellar film." *Physica B: Condensed Matter* 283, no. 1 (2000): 60-64.

[142] Lauter, V., P. Müller-Buschbaum, H. Lauter, and W. Petry. "Morphology of thin nanocomposite films of asymmetric diblock copolymer and magnetite nanoparticles." *Journal of Physics: Condensed Matter* 23, no. 25 (2011): 254215.

[143] Lauter, V., H. J. C. Lauter, A. Glavic, and B. P. Toperverg, Reflectivity, Off-Specular Scattering, and GISANS Neutrons, in *Reference Module in Materials Science and Materials Engineering*. Elsevier. (2016), 1-27.

[144] Rusop, M. "Effect of film thickness on structural, electrical, and optical properties of sol-gel deposited layer-by-layer ZnO nanoparticles." *Transactions on Electrical and Electronic Materials* 13, no. 2 (2012): 102-105.

[145] Parratt, Lyman G. "Surface studies of solids by total reflection of X-rays." *Physical review* 95, no. 2 (1954): 359.

[146] Katmis, F., V. Lauter, F. S. Nogueira, B. A. Assaf, M. E. Jamer, P. Wei, B. Satpati and J. W. Freeland, I. Eremin, D. Heiman, P. A. Jarillo-Herrero. "A high-temperature ferromagnetic topological insulating phase by proximity coupling." *Nature* 533, no. 7604 (2016): 513-516.

[147] Korneev, D. A., V. V. Pasyuk, A. V. Petrenko, and H. Jankovski. "Absorbing sublayers and their influence on the polarizing efficiency of magnetic neutron mirrors." *Nuclear Instruments and Methods in Physics Research Section B: Beam Interactions with Materials and Atoms* 63, no. 3 (1992): 328-332.

[148] Ilavsky, J., and P. R. Jemian. "Irena: tool suite for modeling and analysis of small-angle scattering." *Journal of Applied Crystallography* 42, no. 2 (2009): 347-353.

[149] Hao, L., X. Diao, H. Xu, B. Gu, and T. Wang. "Thickness dependence of structural, electrical and optical properties of indium tin oxide (ITO) films deposited on PET substrates." *Applied Surface Science* 254, no. 11 (2008): 3504-3508.

[150] Riley, D. W., and R. A. Gerhardt. "Microstructure and optical properties of submicron porous silicon thin films grown at low current densities." *Journal of Applied Physics* 87, no. 5 (2000): 2169-2177.

[151] Gundersen, H. J. G., and E. B. Jensen. "The efficiency of systematic sampling in stereology and its prediction." *Journal of microscopy* 147, no. 3 (1987): 229-263.

[152] Zhou, X., and S. Chen. "Model-independent method for reconstruction of scattering-length-density profiles using neutron or x-ray reflectivity data." *Physical Review E* 47, no. 5 (1993): 3174.

[153] Doshi, D. A., A. M. Dattelbaum, E. B. Watkins, C. J. Brinker, B. I. Swanson, A. P. Shreve, A. N. Parikh, and J. Majewski. "Neutron reflectivity study of lipid membranes

assembled on ordered nanocomposite and nanoporous silica thin films." *Langmuir* 21, no. 7 (2005): 2865-2870.

[154] Gondorf, A., M. Geller, J. Weißbon, A. Lorke, M. Inhester, A. Prodi-Schwab, and D. Adam. "Mobility and carrier density in nanoporous indium tin oxide films." *Physical Review B* 83, no. 21 (2011): 212201.

[155] Fang, M., Andrey A., K. V. Rao, A. V. Kabashin, and L. Belova. "Particle-free inkjet printing of nanostructured porous indium tin oxide thin films." *RSC Advances* 3, no. 42 (2013): 19501-19507.

[156] Menzies, D. J., A. Nelson, H. Shen, K. M. McLean, J. S. Forsythe, T. Gengenbach, C. Fong, and B. W. Muir. "An X-ray and neutron reflectometry study of 'PEG-like'plasma polymer films." *Journal of the Royal Society Interface* 9, no. 70 (2012): 1008-1019.

[157] Gerhardt, R. A., and T. R. Grossman. "CHARACTERISATION OF POROSITY IN THERMAL BARRIER COATINGS." *Ceram. Trans.* 11 (1989): 189-199.

[158] Runyan, J., R. A. Gerhardt, and R. Ruh. "Electrical properties of boron nitride matrix composites: I, Analysis of McLachlan Equation and modeling of the conductivity of boron nitride–boron carbide and boron nitride–silicon carbide composites." *Journal of the American Ceramic Society* 84, no. 7 (2001): 1490-1496.

[159] Barsoukov, E., and J. R. Macdonald. *Impedance spectroscopy: theory, experiment, and applications*, pp. 1-8. John Wiley & Sons, Hoboken, NJ, 2005.

[160] Gerhardt, R. A. "Impedance spectroscopy and mobility spectra." *Encyclopedia of Condensed Matter Physics* (2005): 350-363.

[161] Irvine, J. T., D. C. Sinclair, and A. R. West. "Electroceramics: characterization by impedance spectroscopy." *Advanced Materials* 2, no. 3 (1990): 132-138.

[162] Gerhardt, R. A., "Equivalent circuit lecture." Class lecture, MSE 7140 from Georgia Institute of Technology, Atlanta, GA, September, 2014.

[163] Gerhardt, R. A., "Single relaxation process." Class lecture, MSE 7140 from Georgia Institute of Technology, Atlanta, GA, September, 2014.

[164] Gerhardt, R. "Impedance and dielectric spectroscopy revisited: distinguishing localized relaxation from long-range conductivity." *Journal of Physics and Chemistry of Solids* 55, no. 12 (1994): 1491-1506.

[165] "Z-view software", http://www.scribner.com/software/general-electrochemistry/ 68-general-electrochemistr/376-zview-for-windows (Accessed Nov 15, 2017).

[166] Erol, M., Y. Han, S. K. Stanley, C. M. Stafford, H. Du, and S. Sukhishvili. "SERS not to be taken for granted in the presence of oxygen." *Journal of the American Chemical Society* 131, no. 22 (2009): 7480-7481.

[167] Rocha, P. R., P. Schlett, U. Kintzel, V. Mailänder, L. K. Vandamme, G. Zeck, H. L. Gomes, F. Biscarini, and D. M. D. Leeuw. "Electrochemical noise and impedance of Au electrode/electrolyte interfaces enabling extracellular detection of glioma cell populations." *Scientific Reports* 6 (2016): 34843.

[168] RIBEIRO, D. V., C. A. C. Souza, and J. C. C. Abrantes. "Use of Electrochemical Impedance Spectroscopy (EIS) to monitoring the corrosion of reinforced concrete." *Revista IBRACON de Estruturas e Materiais* 8, no. 4 (2015): 529-546.

[169] Demolder, S., M. Vandendriessche, and A. Van Calster. "The measuring of 1/f noise of thick and thin film resistors." *Journal of Physics E: Scientific Instruments* 13, no. 12 (1980): 1323.

[170] Yeh, S., W. Hsu, J. Lee, Y. Lee, and J. Lin. "1/f noise in micrometer-sized ultrathin indium tin oxide films." *Applied Physics Letters* 103, no. 12 (2013): 123118.

[171] Ryu, J., D. Park, and R. Schmidt. "In-plane impedance spectroscopy in aerosol deposited $NiMn_2O_4$ negative temperature coefficient thermistor films." *Journal of Applied Physics* 109, no. 11 (2011): 113722.

[172] Cao, W., and R. A. Gerhardt. "Calculation of various relaxation times and conductivity for a single dielectric relaxation process." *Solid State Ionics* 42, no. 3-4 (1990): 213-221.

[173] Yuan, X., H. Wang, J. C. Sun, and J. Zhang. "AC impedance technique in PEM fuel cell diagnosis—A review." *International Journal of Hydrogen Energy* 32, no. 17 (2007): 4365-4380.

[174] Kokan, J. R., and R. A. Gerhardt. "Humidity Effects on Porous Silica Thin Films." *MRS Online Proceedings Library Archive* 411 (1995).

[175] Gerhardt, R. A., and W. Cao. "Distinguishing bulk water from adsorbed water via dielectric measurements [silica gels]." In *Electrical Insulation and Dielectric Phenomena, 1996, IEEE 1996 Annual Report of the Conference on*, vol. 1, pp. 102-105. IEEE, 1996.

[176] Joshi, S. M. "Effect of Heat and Plasma Treatments on the Electrical and Optical Properties of Colloidal Indium Tin Oxide Films"; PhD Thesis, Georgia Institute of Technology, Atlanta, GA, 2013.

[177] Cesiulis, H., N. Tsyntsaru, A. Ramanavicius, and G. Ragoisha. "The Study of Thin Films by Electrochemical Impedance Spectroscopy." In *Nanostructures and Thin Films for Multifunctional Applications*, pp. 3-42. Springer International Publishing, 2016.

[178] Jin, Y., N. Xia, and R. A. Gerhardt. "Enhanced dielectric properties of polymer matrix composites with BaTiO 3 and MWCNT hybrid fillers using simple phase separation." *Nano Energy* 30 (2016): 407-416.

[179] Gerhardt, R. A., "Measurement dependent factors that can affect the measured electrical response." Class lecture, MSE 7140 from Georgia Institute of Technology, Atlanta, GA, October, 2014.

[180] Hamberg, I., and C. G. Granqvist. "Evaporated Sn-doped In_2O_3 films: Basic optical properties and applications to energy-efficient windows." *Journal of Applied Physics* 60, no. 11 (1986): 123-160.

[181] Preissler, N., O. Bierwagen, A. T. Ramu, and J. S. Speck. "Electrical transport, electrothermal transport, and effective electron mass in single-crystalline In_2O_3 films." *Physical Review B* 88, no. 8 (2013): 085305.

[182] Gerhardt, R. A., and A. S. Nowick. "Grain-boundary effect in ceria doped with trivalent cations: I, electrical measurements." *Journal of the American ceramic society* 69, no. 9 (1986): 641-646.

[183] Ridley, B. K. "Specific negative resistance in solids." *Proceedings of the Physical Society* 82, no. 6 (1963): 954.

[184] Khatami, Y., J. Kang, and K. Banerjee. "Graphene nanoribbon based negative resistance device for ultra-low voltage digital logic applications." *Applied Physics Letters* 102, no. 4 (2013): 043114.

[185] Heinze, S., J. Tersoff, R. Martel, V. Derycke, J. Appenzeller, and P. Avouris. "Carbon nanotubes as Schottky barrier transistors." *Physical Review Letters* 89, no. 10 (2002): 106801.

[186] Yamamoto, T., and M. Morimoto. "Thin-MIS-Structure Si Negative-Resistance Diode." *Applied Physics Letters* 20, no. 8 (1972): 269-270.

[187] Kim, J., K. Na, C. J. Kang, and Y. Kim. "A disposable thermopneumatic-actuated micropump stacked with PDMS layers and ITO-coated glass." *Sensors and Actuators A: Physical* 120, no. 2 (2005): 365-369.

[188] Kim, S., and D. P. Neikirk. "Compact equivalent circuit model for the skin effect." *Microwave Symposium Digest, 1996, IEEE MTT-S International*. Vol. 3. IEEE, 1996.

[189] Logan, D. L. A first course in the finite element method. Cengage Learning, 2011.

[190] Zienkiewicz, O. C., R. L. Taylor, R. L. Taylor, and J. Z. Zhu. The *Finite Element Method: Its Basis and Fundamentals*. Elsevier, Incorporated, 2013.

[191] Kumar, S., and R. A. Gerhardt. "Role of geometric parameters in electrical measurements of insulating thin films deposited on a conductive substrate." *Measurement Science and Technology* 23, no. 3 (2012): 035602.

[192] Jin, Y., S. Kumar, and R. A. Gerhardt. "Simulation of the Impedance Response of Thin Films as a Function of Film Conductivity and Thickness." In *Proceedings of COMSOL Conference*, pp. 1-5. 2015.

[193] Kumar, S., and R. A. Gerhardt. "Numerical study of the electrical properties of insulating thin films deposited on a conductive substrate." *Proc. 2009 COMSOL Multiphysics (Boston, MA, USA) pp* (2009): 1-5.

[194] Chen, Y., and J. Juang. "Finite element analysis and equivalent parallel-resistance model for conductive multilayer thin films." *Measurement Science and Technology* 27, no. 7 (2016): 074006.

[195] Van der Vorst, H. A. "Bi-CGSTAB: A fast and smoothly converging variant of Bi-CG for the solution of nonsymmetric linear systems." *SIAM Journal on scientific and Statistical Computing* 13, no. 2 (1992): 631-644.

[196] Pawar, S. D., P. Murugavel, and D. M. Lal. "Effect of relative humidity and sea level pressure on electrical conductivity of air over Indian Ocean." *Journal of Geophysical Research: Atmospheres* 114, no. D2 (2009).

[197] “Relative permittivity and electrical conductivity from COMSOL Material Library”, https://www.comsol.com/material-library (Accessed Nov 15, 2017)

[198] Pierson, H. O. *Handbook of chemical vapor deposition: principles, technology and applications*. William Andrew, Norwich, NY, 1999.

[199] Valdes, L. B. "Resistivity measurements on germanium for transistors." *Proceedings of the IRE* 42, no. 2 (1954): 420-427.

[200] Kelekanjeri, V. S. K. G., and R. A. Gerhardt. "A closed-form solution for the computation of geometric correction factors for four-point resistivity measurements on cylindrical specimens." *Measurement Science and Technology* 19, no. 2 (2008): 025701.

[201] Veal, B. W., P. M. Baldo, A. P. Paulikas, and J. A. Eastman. "Understanding Artifacts in Impedance Spectroscopy." *Journal of the Electrochemical Society* 162, no. 1 (2015): 47-57.

[202] Martin, E. J. J., M. Yan, M. Lane, J. Ireland, C. R. Kannewurf, and R. P. H. Chang. "Properties of multilayer transparent conducting oxide films." *Thin solid films* 461, no. 2 (2004): 309-315.

[203] “ Display Market by Technology (LED-backlit LCD, OLED, QD-LED, E-Paper), Display Type (Flat, Flexible, Transparent), Application (Smartphone & Tablet, TV & Digital Signage, PC Monitor & Laptop), Vertical, and Geography - Global Forecast to 2022.” http://www.marketsandmarkets.com/Market-Reports/display-market-925.html. (Accessed Nov 15, 2017)

[204] Tai, Y., L. Chuang, and C. Chen. "Liquid crystal display having stripe-shaped common electrodes formed above plate-shaped pixel electrodes." U.S. Patent Application 09/444,141, filed November 20, 1999.

[205] Park, S., J. Choi, E. Kim, and S. Im. "Inverted top-emitting organic light-emitting diodes using transparent conductive NiO electrode." *Applied surface science* 244, no. 1 (2005): 439-443.

[206] Ito, M., M. Kon, C. Miyazaki, N. Ikeda, M. Ishizaki, Y. Ugajin, and N. Sekine. "" Front drive" display structure for color electronic paper using fully transparent amorphous oxide TFT array." *IEICE transactions on electronics* 90, no. 11 (2007): 2105-2111.

[207] Hale, P. S., J. G. Shapter, N. H. Voelcker, M.l J. Ford, and E. R. Waclawik. "Liquid-crystal displays: fabrication and measurement of a twisted nematic liquid-crystal cell." *J. Chem. Educ.* 81, no. 6 (2004): 854.

[208] He, Q., P. Cheng, Y. Yang, L. Wang, K. H. Gardner, and Y. Liu. "White collar-1, a DNA binding transcription factor and a light sensor." *Science* 297, no. 5582 (2002): 840-843.

[209] Rittersma, Z. M. "Recent achievements in miniaturised humidity sensors—a review of transduction techniques." *Sensors and Actuators A: Physical* 96, no. 2 (2002): 196-210.

[210] Byrne, C., and C. L. Lim. "The ingestible telemetric body core temperature sensor: a review of validity and exercise applications." *British journal of sports medicine* 41, no. 3 (2007): 126-133.

[211] Cohen, D. K., J. H. Hunt, and D. G. Crowe. "Characteristics of a chamber used for electrooptical device performance measurements in the presence of fog." *Applied optics* 21, no. 13 (1982): 2399-2404.

[212] Bell, S. "A beginner's guide to humidity measurement." *National Physical Laboratory* 2 (2012).

[213] Patel, N. G., K. K. Makhija, and C. J. Panchal. "Fabrication of carbon dioxide gas sensor and its alarm system using indium tin oxide (ITO) thin films." *Sensors and Actuators B: Chemical* 21, no. 3 (1994): 193-197.

[214] Patel, N. G., K. K. Makhija, C. J. Panchal, D. B. Dave, and V. S. Vaishnav. "Fabrication of carbon tetrachloride gas sensors using indium tin oxide thin films." *Sensors and Actuators B: Chemical* 23, no. 1 (1995): 49-53.

[215] Patel, N. G., P. D. Patel, and V. S. Vaishnav. "Indium tin oxide (ITO) thin film gas sensor for detection of methanol at room temperature." *Sensors and Actuators B: Chemical* 96, no. 1 (2003): 180-189.

[216] Jiao, Z., M. Wu, J. Gu, and X. Sun. "The gas sensing characteristics of ITO thin film prepared by sol–gel method." *Sensors and Actuators B: Chemical* 94, no. 2 (2003): 216-221.

[217] Choi, S. K., and J. I. Lee. "Effect of film density on electrical properties of indium tin oxide films deposited by dc magnetron reactive sputtering." *Journal of Vacuum Science & Technology A: Vacuum, Surfaces, and Films* 19, no. 5 (2001): 2043-2047.

[218] Kuang, Q., C. Lao, Z. L. Wang, Z. Xie, and L. Zheng. "High-sensitivity humidity sensor based on a single SnO_2 nanowire." *Journal of the American Chemical Society* 129, no. 19 (2007): 6070-6071.

[219] Betz, U., M. K. Olsson, J. Marthy, M. F. Escolá, and F. Atamny. "Thin films engineering of indium tin oxide: large area flat panel displays application." *Surface and Coatings Technology* 200, no. 20 (2006): 5751-5759.